This is to certify that the

thesis entitled

COMPOSITION OF SPUTTERED TITANIUM NICKEL AND TITANIUM NICKEL PALLIDUIM FILMS

presented by

THOMAS BRADLEY LAGRANGE

has been accepted towards fulfillment
of the requirements for

M.S. degree in Material Science & Mechanics

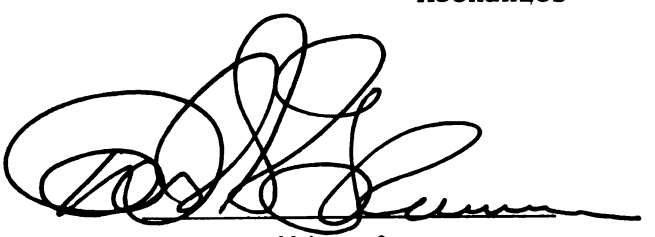

Major professor

Date 11/23/01

COMPOSITION OF SPUTTERED TITANIUM NICKEL AND TITANIUM NICKEL PALLIDUIM THIN FILMS

By

Thomas Bradley LaGrange

A THESIS

Submitted to
Michigan State University
in partial fulfillment of the requirements
for the degree of

MASTER OF SCIENCE

Department of Material Science and Mechanics

2001

ABSTRACT

COMPOSITION OF SPUTTERED TITANIUM NICKEL AND TITANIUM NICKEL PALLIDUIM THIN FILMS

By

Thomas Bradley LaGrange

The properties of shape memory alloys (SMA) are strong function composition, thus tight control of composition is necessary during material manufacturing processes. The goal of the present work is to observe the effect of sputter deposition process on composition of TiNi and TiNiPd SMA thin films. TiNi and TiNiPd films made by d.c. magnetron sputtering have shown composition shift with target erosion, which does not occur in d.c magnetron triode sputtered films. In addition, deposition parameters such as working gas pressure, throw distance, and substrate temperature have been shown to affect the composition. Due to the complexity of the sputter deposition process, it has been difficult to determine the particular phenomena that most affects the film composition, however preferential resputtering, thermalization, diffusion, sticking coefficients, and angular distributions of sputter particles are discussed as possible contributors. Further experiments will be presented that may lead to a solution for the composition control problem.

ACKNOWLEDGEMENTS

I would first like to thank Dr. Ron Averill and Dr. Thomas Pence for their support.

I would like to thank Reza Lolee for his assistance on the triode deposition experiments.

I would like to thank to the MSM department secretaries, Jo Ann Peterson, Lorna Couliter, Debbie Conway, and Iris Taylor.

I would to thank J.C. Brenton, whose design and machining skills help to make my experimental setups possible.

I would especially like to thank Dr. David Grummon who inspired me, and gave me this unique opportunity to study shape memory thin films. Without his guidance and wisdom, this thesis would not be possible.

I would like to thank my parents who have given their support and love that helped me to become successful student and adult.

Finally, I would like to give my unconditional love and gratitude to my wife stands by me through thick and thin and gives me the loving support that I need to achieve my goals.

TABLE OF CONTENTS

LIST OF TABLES

LIST OF FIGURES

CHAPTER 1 INTRODUCTION

Shape memory alloys (SMAs) have been used for many applications, such as eyeglass frames and arterial stents. With recent advancements in thin film technology and micromachining techniques, there has been a growing interest in shape memory thin films for use in micro-actuator systems. The shape memory effect (SME) is dependent on thermoelastic phase transformations at temperatures that are a strong function material composition. These transformation temperatures define the thermomechanical operational parameters of micro-actuators, thus tight control of composition is necessary to obtain the desired properties of the SMA and device operation.

Since titanium and nickel have very different vapor pressures, vacuum evaporation is impractical, and sputtering has been the preferred way to manufacture TiNi shape memory thin films. Sputtering is the most widely used manufacturing process in the thin film industry because it can produce films of any desired composition with high substrate adhesion [Bunshah, 1994]. The physical nature of the sputtering plasma is not well understood. In recent years, there has been a significant effort to understand the sputtering deposition process for complex alloys [Bunshah, 1994]. The goal of the present work has been to understand the effect of sputtering deposition parameters on composition of sputtered TiNi and TiNiPd alloys.

There have been many studies on the metallurgical and mechanical properties of TiNi thin films, but very few research studies have focused on the effect of sputtering parameters on the production TiNi SME thin films. The sputtering process is so complex, and little is known about the effects of deposition parameters on the composition

of sputtered alloys. Many experimental results are empirical and are concerned with alloys of particular use in the semiconductor and computer industry. Compositional shifts from preferential resputtering have been observed in sputtered superconductive YBaCuO and BiSrCaCuO thin films. In this case, small deviations in composition from stoichiometry can dramatically change the superconductivity characteristics [Grace, 1991; Selinder, 1991]. Likewise, small deviations from stoichiometry in TiNi alloys may shift the martensite start (M_s) temperature significantly and also change the mechanical strength and ductility of the alloy [Wang, 1965].

The above-mentioned studies on superconductive thin films used X-ray fluorescence to observe changes in composition with respect to the target as a function of sputter gas pressure and deposition temperature [Grace, 1991; Selinder, 1991]. In the same manner, much of present work has been focused on tracking composition changes as a function of deposition parameters such as target erosion, working gas pressure, substrate-target distance, and deposition temperature. This thesis will present results and theoretical models of sputtering yield found in the literature to help develop an understanding for these composition shifts. In addition, ideas for future experiments will be presented that will give a further understanding of the sputtering phenomena that affect composition.

The technical goal of this research work has been to develop a sputter deposition process that gives reproducible results and yields films of a predictable composition. Due to complexity of sputtering process, no definitive conclusions have been drawn regarding the actual mechanisms that determine composition in sputtered TiNi and TiNiPd alloy. Instead, a list of all the possible phenomena associated with the sputter deposition process

that effect film composition will be evaluated in light of the experimental results along with future experiments, which may lead to better understanding and a solution to this very important composition control problem.

CHAPTER 2 LITERATURE REVIEW

The purpose of this chapter is to introduce the Shape Memory Effect and the effects of composition on the thermomechanical properties of shape memory materials. In addition, background information on the sputtering process will be presented along with mechanisms that are thought to result in composition shifts during sputter deposition of alloy systems.

2.1 Shape Memory Properties of TiNi

2.1.1 Martensitic Transformations

To understand the Shape Memory Effect in TiNi, an explanation of the process of martensitic transformations is useful. The martensitic transformation in shape memory alloys is a displacive phase transformations that does not require atomic migration to form the new crystal structure. These phase changes are first-order transformations where heat is liberated when the martensite is formed upon cooling. There is a thermal hysteresis that defines the associated transformation temperature and a temperature range where both martensite and austenite coexist. This type of martensitic transformation is sometimes described as athermal since the driving force for the phase transformation is the free energy change of the transformation. Thus, the reaction is not rate dependent, since thermal activation is required.

The martensite transformation produces austenite/martensite (A/M) phase boundaries, which are highly glissile and are either partially or fully coherent. At first observation, the lattice appears to undergo a simple shear between the (A/M) phases, like

twins, however, this simple shear will not produce the martensite symmetry or lattice parameters. The actual deformation is a lattice invariant-plane strain that gives the undistorted habit for deformation and accommodates the new lattice symmetry martensite. The mechanisms of transformations are complex, and the phenomenological crystallographic theory, or Wechsler Lieberman Read (WLR) theory, offers crystallographic explanation of the behavior of martensitic phase transformation based on experimental observations. The following paragraphs discuss this theory in more detail.

2.1.1.1 Phenomenological Theory

Since martensitic transformation happens sometimes at the speed of sound, and since actual observation of the transformation is impossible, the WLR theory offers logical steps for the transformation that correlate with experimental conclusions. The first logical step in the martensitic transformation is a lattice deformation, which creates the new lattice symmetry. This deformation is often termed as a Bain strain or distortion, since Bain was the first to observe this phenomenon. If the accommodation deformation does not cause any structural change in the newly formed crystal, there must be an undistorted crystallographic habit plane to produce the coherent phase boundary between the austenitic and martensitic structure. A simple shear created from twinning will not produce an undistorted reference plane. Therefore, there must be an invariant plane deformation that produces an undistorted habit plane and the experimentally observed martensite phase symmetry and lattice parameters [Wayman, 1983]. The final step in the phenomenological theory is a rigid body rotation of the invariant plane to bring it into

lattice correspondence with parent and product phases, which can be imagined by superimposing the parent and product lattices.

2.1.1.2 Martensite Internal Twin Structures and Variant Interfaces

The lattice deformation in TiNi is shear-dominated, unlike steels that have both a shape and volume change [Duerig, 1990]. The shape change must be accommodated by the surrounding austenite lattice structure, which can be accomplished by either slip or twinning. The slip deformation is permanent and is common in steel martensitic transformations, while twinning is the preferred accommodation deformation in shape memory alloys and creates twin boundaries that are reversible [Duerig, 1990]. The twin structure is self-accommodating due to the creation of internally twinned martensite variants (called transformational twins) that result in no net macroscopic shear strain in the crystal, and there can be as much as 24 martensite variants formed from one austenite crystal [Duerig, 1990].

There have been many investigations into the crystallography of the internally twinned structures that are produced in the TiNi alloys. Matusumoto *et al.* have used the deformation twinning theory of Bilby-Crocker to calculate the twinning elements of TiNi single crystals observed by Transmission Electron Microscopy and X-ray Diffraction. Table 2-2 shows the values for the twinning modes in the martensitic transformation. Matsumoto *et al.* used a tensile stage to deform a TiNi single crystal, and the twin plane orientation of the stress-induced martensite was observed with a Laue camera and diffractometer. Their theoretical calculations in Table 2-2 confirmed that the two twinning systems possible during the experiment were the {111} Type I and <110> Type

II twins, however the experimental results concluded that Schimid factor was zero for both {111} Type I twinning. The habit plane calculated from this study was (0.8684 0.26878 0.4138), which deviated from the theoretically predicted plane by 3.3 degrees [Matusumoto, 1987].

Table 2-1. Twinning modes [Matusumoto, 1987]

Twin	K_1	η_1	K_2	η_2	s
{111} Type I	(111)	[.054043 0.45957 1]	(0.24695 0.50611 1)	[211]	0.30961
{111} Type I	(111)	[1.51172 0.51172 1]	(0.66875 0.3375 1)	[211]	0.14222
<110> Type II	(.72053 1 1)	[011]	(011)	[1.57271 1 1]	0.28040
Compound	(001)	[100]	(100)	[001]	0.23848

Nishida *et al.* did a similar study of the transformation twin system in TiNi martensite using high-resolution transmission electron microscopy of room temperature electropolished martensite thin foils. The first observation of this study was that the (001) compound twin was formed by an instability of the martensite during high temperature electropolishing procedures and was not observed at lower electropolishing temperatures. This is in accordance with the theoretical calculations by Matsumoto *et al.*, which show that the compound twin mode should not exist in the martensite. Nishida *et al.* also observed by electron diffraction and microscopy that the <110> Type II twin was found in the martensite. However, the two studies conflicted on the issue of the {111}

Type I twin system, which Nishida *et al.* believed to exist due to the additional mutual self-accommodation between the martensite variants by <110> Type II twinning. The transformation TiNi produces pairs of <110> Type II transformation twins in separate variants that are accommodated by {111} Type I twinning. However, Matsumoto *et al.* believed that this was an artifact of formation of TEM thin foils and was not an accommodation mechanism. Since the Matsumoto study focused on a stress-induced martensite that had a tensile axis orientated such that there was no resolved shear stress on K_1 plane of the {111} Type I twin system, it was concluded that Type I twins do not form during stress induced martensite formation. The basic conclusion of the above studies is that the type of self-accommodating twin structure is governed by both internal and external stress fields in the austenite.

Twin boundaries in the martensite have a low energy and are quite mobile [Durieg, 1990]. If a stress were applied to the self-accommodated twin structures, the variant and twin boundaries between the transformation twins would easily move to produce a shape strain that would accommodate the applied stress. This would result in the conversion of non-stress-preferred variant crystal to the orientation of the stress-preferred variant. If the martensite is sufficiently strained, a single martensite variant can be produced. This mechanism of internal twin boundary motion is termed "detwinning" and is an important aspect of shape recovery in shape memory materials as will be discussed in the following section.

2.1.2 The Shape Memory Effect

The Shape Memory Effect (SME) arises from the crystallographic reversibility of the self-accommodated twin structure [Duerig, 1990]. The martensite phase has a lower symmetry than the austenite. As a consequence, there are many ways in which the martensite variants can be formed and distributed, but only one possible way to revert back to austenite structure due to the high chemical ordering of the austenite phase [Duerig, 1990]. Consequently, biased martensite variant distributions created by detwinning stress must revert to the original lattice orientation, and as a result, any shape strains caused by the detwinning deformation are recovered. This recovery of shape strains incurred by detwinning of martensite is known as the Shape Memory Effect (SME).

The shape memory effect can be described schematically with reference to the cooling and heating curves shown in Figure 2-1. There is no shape change when the austenite is cooled to martensite phase. When the SMA material is deformed below the martensite finish (M_f) temperature, it will remain deformed until it is heated above the austenite start (A_s) temperature. The shape recovery begins at A_s and is completed at A_f. Once the shape is recovered at A_f, a subsequent cooling to M_f does not cause a shape change. The shape memory can only be reinitiated by a repeated deformation of martensite and heating to A_f. Therefore, the shape memory effect shown in Figure 2-1 is a one-time occurrence, which can be referred to as the one-way SME. The operation of SME is defined by the characteristic transformation temperatures of the alloy, M_s, M_f, A_s, and A_f. Figure 2-1 illustrates the use of electrical resistivity versus temperature curves as a means for determining the transformation temperatures of a material. Other methods,

such as differential scanning calorimetry (DSC), are also commonly used to gather transformation temperature and enthalpy data of SMA materials.

In addition to one-way SME, another manifestation of the thermoelastic martensitic transformation is the Superelastic Effect (SE). SE occurs by isothermal reversible martensitic phase transformation at temperatures above Af. When the stress is applied to austenitic alloy, it nucleates a preferred martensite variant within the austenite matrix. The shape strains caused by the accommodation of the preferred martensite variant in the austenite can be recovered by releasing the stress due to the reversible nature of the A/M interfaces. SE can be thermodynamically described by a modification of the Clausius-Claperon Equation, which gives the transformation temperatures as a function of stress.

2.1.3 Equilibrium Phase Structure and Phase Stability of TiNi

Observing the TiNi binary phase diagram, stoichiometric TiNi can exist at high temperature and has a steep solvus boundary on the Ti-rich side and a slight solubility of nickel (see Figure 2-2) on the Ni-rich side of stoichiometry. Under 1250 K, Ti_2Ni will precipitate out of B2 TiNi matrix when the compound is Ti-rich, and $TiNi_3$ is equilibrium precipitate phase in Ni-rich alloys[1]. The equilibrium phase diagram has traditionally shown an eutectoid decomposition of TiNi$\rightarrow$ $TiNi_3$ + Ti_2Ni at 900 K, however, Wasilewski *et al.* proposed that the TiNi may remain a stable phase down to room temperature with a very narrow stoichiometric range, as shown in Figure 2-3. Furthermore, Van Loo *et al.*, Nishida *et al.*, and Kim *et al.* reported the existence of

[1] Its existence depends on temperature and amount of excess nickel, since excess Ni is partially soluble in stoichiometric compound.

metastable phases other than Ni_3Ti on the Ni-rich side, such as Ni_3Ti_2 and Ni_4Ti_3. The equilibrium phase diagram for the Ni-rich side at room temperature is not well established, and the composition and structure of the intermellatic phases have been a source of debate. Most commercially used TiNi SMA is single phase that has small amounts of intermellatic precipitate phase, usually Ni_4Ti_3, distributed in the B2 matrix. These precipitate phases are generally isomorphous with TiNi and produce coherency strains that affect the transformation and mechanical characteristics of the alloy, which is discussed in the following section.

2.1.4 Effects of Composition on Transformation Temperatures TiNi and TiNiX Alloys

The martensitic start temperature (M_s) is strongly dependent on the composition, especially on the Ni-rich side of stoichiometry, as shown in Figure 2-4. The M_s temperature can change up to 100 K per atomic percent enrichment in nickel above stoichiometry. On the Ti-rich side of stoichiometry, the transformation temperatures are only slightly affected by the enrichment of titanium (15-25 K/ per at% Ti). The changes in transformations are related to solubility of nickel and titanium in the B2 matrix and to the formation of precipitates.

The M_s temperature's stronger dependence on nickel content is related to the high solubility of Ni in the B2 matrix above 775 K [Melton, 1990]. The excess nickel dissolved in the B2 matrix causes coherency strains and stresses that suppress the M_s temperatures [Miyazaki, 1999]. In addition, precipitation of nickel rich phases can increase the M_s temperature by forming a more Ti-rich matrix that has a higher M_s temperature [Ishida, 1995]. However, over-aging of nickel-rich precipitates, such as

Ti_3Ni_4 and $TiNi_3$, can create internal stress fields that suppress the M_s temperature by constraining the formation of martensite variants when precipitates become semi-coherent with the matrix [Xie, 1990].

Miyazaki and Ishida explored the aging effect and distribution of Ti_3Ni_4 on the transformation temperatures in Ni-rich TiNi thin films. They reported that as aging time increased, the observed M_s temperature (See Figure 2-5 (a) and 2-6) increased as a result of formation and growth of Ti_3Ni_4, which depletes the dissolved excess Ni in the matrix [Miyazaki, 1999]. In addition, Miyazaki and Ishida [1999] investigated the aging time of Ti-rich TiNi thin films on the transformation temperatures and showed that it had little to no affect on the transformation temperatures, as shown in their results in Figure 2-5 (b) and 2-6. This is expected since Ti is almost completely insoluble in the B2 matrix. The excess titanium forms Ti_2Ni precipitates, which tend to nucleate at the grain boundaries, and the aging and growth of these precipitates has no affect on the M_s temperature [Melton, 1990; Miyazaki, 1999]. Miyazaki and Ishida [1999] observed the presence of the R-phase transformation above the A_f and lower than expected M_s temperatures in Ti-43.9% Ni films (See Figure 2-5 (b)). This was attributed to fine internal metastable Ti-rich precipitates[2], which exist as very thin platelets or GP zones distributed 5-10 nm apart on {100} B2 planes [Miyazaki, 1999]. They believed that these structures have the same effect as dislocations and semi-coherent Ni-rich precipitates in the bulk material, which suppress the M_s temperature [Miyazaki, 1999].

The annealing temperature greatly affects the transformation temperatures due to difference in amount of precipitate formation and growth with temperature. As

[2]These precipitates were observed in Ti-rich film that were crystallized from amorphous as-deposited thin films.

mentioned previously, nickel is slightly soluble in the B2 matrix, and according to the binary phase diagram in Figure 2-2 and at temperatures around 700 ° C, 2-3 at. % excess Ni is dissolved in equiatomic TiNi. Therefore, transformation temperatures can decrease if the high solutionizing temperatures drive excess nickel in the solution. The effect of solutionizing annealing temperature on Ni-rich TiNi thin films is shown in Figure 2-7. Ishida *et al.* observed Ti_3Ni_4 precipitates at the lower annealing temperatures but also observed the absence of these precipitates at the higher annealing temperature of 973 K, which is related to dissolution of excess nickel [Ishida, 1995].

On the other side of stoichiometry, Ti is almost completely insoluble B2 matrix at any temperature. The transformation temperatures of Ti-rich films increase with increasing solutionizing temperature, as seen in Figure 2-8. The increase in annealing temperature will further promote the growth Ti_2Ni precipitates [Ishida, 1995]. However, Ti_2Ni precipitate growth should not affect the transformation temperatures, and Ishida's discussion about the effects of Ti_2Ni growth resulting in increased transformations temperatures is ambiguous and contrary to results shown by Wang [1965] (see Figure 2-4). However, this increase in transformation temperatures can be related to the relief of the localized strain fields in austenite grains due to growth of Ti_2Ni and their incoherence with the austenite crystal, and therefore facilitate growth of the martensite at higher temperatures due to this internal stress relief.

Elemental impurities, such as O, N, C, and H, in TiNi can also affect the transformations temperatures. Since Ti is very chemically reactive, it easily forms compounds with the fore mentioned impurities that deplete the matrix of Ti, making it Ni-rich, which would lower the M_s temperature. According to Melton [1990], the

presence of oxygen in the TiNi alloy can decrease its stoichiometric range and result in the coexistence of both Ti and Ni-rich precipitates (See Figure 2-9). Thus, Ni-rich precipitate phases can be present in Ti-rich NiTi, and Ti_2Ni can be present in Ni-rich alloys. The stable oxide formed with TiNi is $Ti_4Ni_2O_x$ that is isostructural with Ti_2Ni, which makes it difficult to identify.

The addition of ternary elements that substitute for Ni or Ti in stoichiometric TiNi can shift the transformation temperatures and decrease the thermal hysteresis. The substitution of Cu for Ni in TiNi has shown to narrow the thermal hysteresis, as seen in Figure 2-10 [Miyazaki, 1999; Melton, 1990]. This same effect also occurs when Pd is substituted for Ni [Miyazaki, 1997], while the substitution of Hf for Ti widens the hysteresis [Johnson, 1995]. Palladium additions over 10 at. % can dramatically increase the M_s temperature, while Pd content between 6-10 at. % can decrease M_s temperature below 0°C, as seen in Figure 2-11 [Lindquist, 1988].

2.1.5 Mechanical and Metallurgical Studies of Sputtered TiNi SMA Thin Films

2.1.5.1 Binary TiNi

The strength of the austenite controls two key properties in TiNi alloys: its resistance to deformation during manufacturing processes, and the force that the alloy can exert during shape recovery [Duerig, 1990]. High yield strengths can make drawing and forming of TiNi very difficult, at the same time it is desirable to have large temperature ranges for superelasticity and high recovery forces in shape memory alloys. The austenitic strength and total plastic strain of TiNi is a strong function of material composition (See Figure 2-12 and 2-13), since precipitate structures can increase the

strength of the material by impeding dislocation motion, but as consequence, it also reduces the ductility of the material.

The aging of Ni-rich precipitates, such as Ti_3Ni_4, can increase the austenitic strength and critical stress for slip, but over-aging can also decrease the austenitic strength. The size of the Ti_3Ni_4 precipitates has a profound effect on the critical stress for slip when it is less than 100 nm in diameter, as seen in Figure 2-14 [Ishida 1999a]. The high yield stress of Ni-rich films can be attributed to fine Ti_3Ni_4 precipitates and fine grain structure[3] [Ishida, 1996]. In addition, transformational strains are changed by annealing Ni-rich films, which increase with increasing annealing temperature, as seen Figure 2-13 [Ishida, 1995]. This increase in transformation strain is attributed to the growth of Ti_3Ni_4 precipitates, which lose their ability to suppress the growth of preferentially oriented martensite variants as they increase in size [Miyazaki, 1999].

Ti-rich films that are sputtered at room temperature and crystallized at 773 K also exhibit higher tensile strength than equiatomic TiNi thin films, due to precipitate strengthening from the Ti-rich GP zones, as seen in Figure 2-13 [Ishida, 1999]. Bulk (melt-solidified) TiNi materials that have over 1 at. % excess-Ti are very brittle and do not show ductility anywhere near to the 20 % reported by Ishida *et al.* in sputtered films of the same composition [Ishida, 1999]. This lack of ductility is related to the precipitation of Ti_2Ni at the grain boundaries, which promotes intergranular fracture [Matsunaga, 1999]. Ti-rich films sputtered by Ishida *et al.* have a different precipitate structure than bulk materials, and consist of Ti-rich GP Zones that increase the strength of austenite but allow the material to remain ductile. Over-aging or high temperature

[3] Sputtered TiNi films have an average grain size 200-1000 nm, which is much smaller than the bulk materials, where the average grain size is 100-200 μm.

annealing of Ti-rich films leads to a slight increase in tensile strength, but greatly reduces the overall ductility, as seen in Figure 2-16 (a) and (b). The films in Figure 2-16 (b) showed no apparent plastic deformation, but still exhibited a large recoverable deformation strain from stress-induced martensite transformation and martensite variant detwinning [Ishida, 1999]. The effects of annealing temperatures on transformation strain are shown in Figure 2-15 [Ishida, 1995]. The strain-temperature curves at low constant stress have a two-stage transformation hysteresis that is associated with R-phase and martensitic transformation, while high constant stress strain-temperature curves have a single-stage martensitic transformation. As seen in Figure 2-17, there was very little to no plastic strain at low constant stress, while high plastic strains exist at high constant stresses, which suggest that the R-phase transformation can suppress dislocation formation in martensitic transformation [Ishida, 1995].

2.1.5.2 Ti-(Ni+Pd) Structure and Mechanical Properties

As stated earlier, substituting more than 10 at. % Pd for Ni in equiatomic TiNi is useful for increasing the M_s temperature. The Pd content can also change the crystal symmetry of martensite, which is B19' monoclinic for composition less than 15 at. % Pd, B19 orthorhombic for composition greater than 20 at.% Pd, and mixed monoclinic and orthorhombic when compositions are between 15 and 20 at. % Pd [Sivokha, 1983]. Sivokha *et al.* also reported the parent phase of all compositions and additions Pd of Ti-Ni+Pd to be the B2 structure. The effect of Pd composition on the lattice parameters of Ti-(Ni+Pd) B19 martensite are shown in Figure 2-18, which is from the data reported by Lindquist, Sivokha *et al.*, and Shugo *et al.* [Lindquist,1988]. Lindquist reported that 10

at. % Pd alloy was B2 austenite at room temperature (300 K) and had a lattice parameter a=0.309 nm, which was determined using the Cohen method and the diffraction peaks of (211) and (222) [Lindquist, 1988]. The lattice parameter as function of Pd content data collected by Lindquist and Shugo *et al.* are shown in Figure 2-19.

Limited research work has been done on the mechanical properties of sputtered TiNiPd films. However, Miyazaki *et al.* have shown that Ti-26.4 at. %Ni-21.8 at. % Pd films have high transformation temperatures, a high resistance to slip deformation, and a perfect shape recovery at a constant stress of 200 MPa, as seen in Figure 2-20 [Miyazaki, 1999].

2.1.6 TiNi Thin Film Sputtering Composition Experiments

The compositions, crystal structure, morphology, and transformation temperatures of Ti-(Ni+Cu) and periodic multi-layered Ti-(Ni+Cu) and Ti thin films were studied by Chang *et al.* [Chang,1991; Chang 1992]. These films were sputtered using a triode sputter gun, and in the composition results, a Ti depletion in sputtered–deposited films relative to target composition was observed. Chang reported the reason for this depletion was related to energetic bombardment of neutral species on the growing film, resulting in a preferential resputtering effect of Ti [Chang, 1992]. This contradicts published data on the sputtering yield of pure Ti and Ni, since Ni has a much higher elemental sputtering yield than Ti [Waits, 1978]. Thus, a Ni depletion in the growing film may have been produced by a preferential resputtering effect. However, Chang indicated that the sputtering of TiNi compounds might have different sputtering properties than pure elements, which caused the Ti-loss. To understand the sputtering behavior of amorphous

TiNi alloys, Chang designed a series of ion beam assisted deposition (IBAD) experiments and plotted the Ti-depletion as function ion to atom arrival ration (I/A) for various ion energies, which is shown in Figure 2-21 [Chang, 1992]. Ti depletion increases with increasing I/A ratio, and dramatic increase in titanium-nickel sputtering ratio ($Y=Y_{Ti}/Y_{Ni}$) was also observed at low ion beam energies [Chang, 1992]. In low ion energy regimes (<100 eV), the sputtering yield changed dramatically and was sensitive to the slight variation in ion energy. At intermediate level ion energies of 200 eV in argon, pure titanium sputtering yield is 0.2 atoms/ion, while pure nickel has a sputter yield of 0.7 atom/ion [Vossen, 1971]. This would indicate that titanium-nickel sputtering ratio should be less than 1. However, Chang concluded from experiments that the sputter yield of Ti was greater than nickel in the low to intermediate regimes (<500 eV), and the sputter yield ratio of Ti to Ni changed from 9 at 50 eV to 1.75 at 500 eV. These results are inconsistent with elemental sputtering data, but offer an insight into the preferential sputtering Ti in amorphous TiNi alloys. The discrepancy is probably related to the relative binding energies in the pure elements and in the compound.

Table 2-2. Sputtering[4] Conditions and Film Composition [Ishida, 1993].

Run	Ar Gas Pressure (Pa)	RF Power (W)	Substrate Temperature (K)	Film Composition (at. %)	
				Ti	Ni
1	13.3	400	523	50.2	49.8
2	6.7	600	573	50.5	49.5
3	6.7	400	523	50.6	49.4
4	6.7	200	523	51.6	48.4
5	0.67	400	523	48.6	51.4

[4]Target Composition was Ti-50 at. % Ni, and target-substrate distance was 82mm.

Ishida *et al.* produced TiNi thin films using RF magnetron sputtering[5] and reported the composition for different RF powers, working gas pressures, and substrate temperatures, which is shown in Table 2-3 [Ishida, 1993]. Their studies were not intended to observe the effects of sputtering parameters on composition, however it is interesting to observe the tends in composition that resulted. Ishida *et al.* used an electron probe micro-analyzer (EPMA) to determine that composition, which has a precision similar to energy dispersive spectroscopy (EDS) methods (±0.25 at. %). Two interesting titanium composition shifts are noted, a Ti- depletion at low working gas pressure in Run 5, and a Ti enrichment at low RF power in Run 4. This result coincides with the results observed by Chang, who found a Ti-depletion at low working pressures [Chang, 1992]. Reflected neutrals leave the target with a large fraction of the initial ion energy, and these low ion energies might not create reflected neutrals that have sufficient energy to breach the sputtering threshold of Ti at the growing film. Therefore in Run 4, there might not be preferential resputtering of Ti due to low ion energies, which results in Ti enrichment. However, other factors may be involved in this particular observation of Ti-enrichment, such as differential angular distribution of sputter particles and non-steady-state sputter conditions at the target surface. Therefore, none of these results and comments can be conclusive, however the observed composition shifts due to various sputtering parameters is prevalent.

J. C. Lee has also done an insightful investigation on the effects of plasma energy, working pressure, and working distance on the composition of sputtered TiNi thin films. He believed that during steady-state conditions, where the sputter flux has the same

[5] RF magnetron sputtering does not offer any advantage over dc magnetron sputtering, since TiNi is conductive material.

composition as the target, the preferential resputtering of Ti was the dominating effect for the overall Ti-depletion observed regardless of the effects of angular distributions and scattering differences between Ni and Ti [Lee, 1994]. However, when an enrichment of Ti was observed, it corresponded to formation of target surface morphologies exhibiting microscopic cones, etch pits, and ridge structures, which lead to the preferential sputtering of Ti over Ni [Lee, 1994].

Lee also studied the effect of working gas pressure and throw-distance on composition in binary TiNi, which is shown Figures 2-23 and 2-24 [Lee, 1994]. The increase in pressure will thermalize or reduce the energy of incident particles to the growing film and cause sputtering flux to become diffuse due to scattering events. The former effect reduces the energy of energetic neutrals and thus would reduce the resputtering effect, which makes Lee's conclusion of increase in resputtering questionable. However, since Ti is the lighter sputtering species it would scatter more diffusely, and less Ti would reach the growing film, which is a more probable reason for the observed Ti-depletion. The increase in working distance has the same effect as increasing pressure, since more collisions with sputter gas particles and scattering are possible at longer distances. Again, longer distances do not increase resputtering and in fact should reduce the resputtering effect.

Lee also conducted some experiments to examine the effect of sputtering power on the composition of TiNi films. The films sputtered at 150 W had a composition resulting from steady-state sputtering conditions and a Ti-depletion that Lee attributed to resputtering. While, the Ti enrichment observed at 300 W sputtering power was attributed to non-steady state sputtering due to topographical effects, such as the

formation of cones. The off-axis depletion of Ti was attributed to an unbalanced magnetic field that results in an additional bombardment of electrons and ions at the outer edge of the substrate. The enrichment of Ni in sputter flux and film composition at 450 W was concluded to be caused by resputtering effects and rarefaction of the sputtering gas, which is explained by the increase in the plasma voltage as the power increased from 300 W to 450 W.

The conclusions made by Lee are questionable, but his observations and data offer insight on composition control problems in sputter deposition of TiNi and the complexities of the sputtering process, which are discussed in detail in the following sections.

2.2 Sputter Deposition

Sputtering can be defined as the ejection of particles from a condensed matter target material due to the bombardment of energetic projectiles. The greatest advantage of sputter coating is that virtually any target material can used to form a thin film. However, since sputtering is a complex multi-parameter process, it is difficult to create predictable results, especially in the case of alloys. Thus much research has been conducted in order to theoretically understand the physical nature of sputtering and to develop an empirical formula for processing materials of interest by sputtering.

Sputter deposition is a vacuum coating process that employs a target material (source material for the thin film), a substrate where the thin film is grown, a noble or reactive sputtering gas, and sputter gun that provides for water cooling of the target and magnetic enhancement of the plasma. Typically, the substrate is mounted opposite of the

target material in a vacuum chamber, which is initially evacuated to 10^{-6} to 10^{-10} Torr[6]. Then the chamber is backfilled with the sputtering gas to pressure between 1 and 100 mTorr, depending on the type of source and thin film process. A negative potential[7] is applied to the target (cathode) to ionize the gas and initiate ion bombardment of the target, while the substrate (anode) is grounded or kept at a negative potential relative to the sputtering plasma[8]. A schematic of a sputtering apparatus is shown in Figure 2-26, which employs a diode type gun [Bunshah, 1994]. The plasma used in the sputtering process is complex and is discussed in the section below.

2.2.1 Principles of DC Sputtering Glow Discharge

The energetic ions that bombard the target during sputtering are generated by a glow-discharge, which is named for the light emitted from excited atoms. The glow discharge used in sputtering is known as an 'abnormal negative glow' [Coburn, 1980], which is self-sustaining type of plasma in which there are an equal number of positive ions and negatively charged particles [Chapman, 1980]. The voltage-current relationships for a DC discharge are shown schematically in Figure 2-27 [Mahan, 1999]. The primary region of interest on V-C curve is the breakdown regime, where a sudden drop in voltage occurs that sustains the discharge at a fixed current value. During breakdown, ions acquire enough kinetic energy that collisions with the cathode generate secondary electrons, which are emitted from the target surface of the cathode and accelerated towards the anode and collide with sputter gas atoms producing ions. Thus,

---

[6] The ultimate base pressure depends on process and the amount of allowable residual gas contamination, and reactive sputter species can be greatly affected by residual oxygen and water vapor.

[7] Typical voltages range from 5 keV to 200 eV.

the cycle of electron-ion formation is repeated, and the plasma is self-sustaining. After breakdown, current increases at a constant due the increase in secondary electron emission at asperities on the target surface that cause a non-uniform current density across the target surface. The plasma is sustained mainly by impact ionizations in the cathode sheath, but this is not the practical plasma used in sputtering. After normal glow regime, the abnormal glow conditions is reached where the entire target surface area used and current density is uniform. The abnormal glow regime used in DC magnetron sputtering typically obeys the voltage-current relationship given by Equation 1.

$$I \propto (V)^n \qquad (2-1)$$

where n in is the range of 5-15 [Rossnagel, 1988].

The self-sustaining discharge has a particular structure, as seen Figure 2-28. The Crookes Dark Space or Cathode Dark Space, according to Maissel et al. [1970], is the "region of primary interest ... its thickness is approximately the mean distance traveled by an electron from the cathode before it makes an ionizing collision." The term "dark" comes for the fact that this region does not emit light or contain excited particles since too few electrons are present. This region is commonly referred to as the cathode sheath in processing plasmas but it is several times thicker than the actual cathode sheath. The actual cathode sheath[9] in practical plasmas is a region in which ions are accelerated at energy equivalent to the cathode voltage drop ('fall'). This voltage potential between the plasma and cathode is larger than applied negative potential to the cathode since the plasma slightly positive [Mahan, 1999].

---

[8] This is known as biased substrate sputtering.
[9] A sheath is a volume space charge region, where electrical charge density is not equal to zero and it surrounds the cathode and anode.

The negative glow region of the self-sustaining plasma is where primary electrons expend their energy and impact ionizations occur. It has a visible light emission with colors related to the excited neutral species. Classically, the positive column extends from the negative glow to the anode, which has an electrical field sufficient to transport the discharge current to the anode and produce ionization that makes up for wall losses [Bunshah, 1994]. However, most modern sputtering setups place the substrate in the negative glow region, and the positive column does not exist. As a consequence, higher sputtering gas pressures must be used due to the small inter-electrode spacing, which causes loss of electrons to the walls or anode before they collide with gas atoms to produce ions.

2.2.2 Sputtering Mechanisms

Sputtering is a statistical process that results from a momentum-exchange collisional cascade in the near-surface region of the target that is initiated by bombardment with incident energetic projectiles [Bunshah, 1994]. If an ion strikes the target at near surface-normal angles, it is obvious that a single collision will not produce a sputter particle (sometimes referred to as ejected recoil). The momentum of the incident ion will drive atoms into the lattice structure of the solid from the single binary collision, and the momentum vector of the target atom clearly cannot be altered by more than the 90 ° that is necessary for it to leave the solid. Figure 2-29 shows a schematic of collision cascade resulting for an incident ion that creates a sputter particle. Computer simulations on Cu with 600 eV Ar ions shows that the collision cascade radius is on the order of 10 nm, and those that intersect surface and transfer enough momentum to result in recoil are

few [Harrison, 1978]. Statistical analysis shows that sputter ejection rarely occurs from collision cascades that develop more than 5 atomic monolayers below the surface, and most of the energy transferred to the lattice is lost to heat [Bunshah, 1994]. Because of the large amount of heat transferred to the target upon sputtering, most sputtering systems and processes provide for cooling of the targets to avoid equipment damage and bulk diffusion of constituents in multi-element targets.

There are three different energy regimes of collision cascades classified by Sigmund [1981], which are displayed schematically in Figure 2-30. The low energy single 'knock-on regime' is related to low projectile energies just above the threshold energy (energy required to produce sputter atoms) that result in very few sputtered atoms. In this regime, sputtering results from a single binary collision between surface atoms and internally backscattered ions or neutrals. In the linear cascade regime, the sputter yield is proportional to the surface binding energy, and the number of recoils is still low. Most of the models regarding sputter yield assume this type of cascade since it is the dominant mechanism in most commercial and experimental sputtering processes. The last regime is the spike regime that is sometimes referred to as thermal sputtering since atoms are ejected in ways similar to vaporization, which is a thermal process rather than collisional [Sigmund, 1981]. This regime is typified by a high sputtering yield, termed as 'excess yield', and it has a nonlinear type of cascade, which results from a combination of high projectile energies, heavy mass projectiles, and low surface binding energies.

2.2.3 Sputtering Yield

The sputtering process is quantified in terms of sputtering yield, which is defined as the number of recoils per incident ion. The yield is dependent on the surface binding energy of the target, the energy of the bombarding species, the mass of projectile ion, incidence angle of the bombarding ion species, and the amount of target conditioning caused by previous sputtering. The sputtering yield is relatively insensitive to the target temperature in that most sputtering applications that operate in the linear cascade regime, where evaporation rates are orders of magnitude lower than the sputtering rates [Sigmund, 1981].

When the projectile type and energy is held constant, the yield increases with volatility of the target material, which is related to its surface binding energy. Kelly [1984] observed a periodic trend in sputtering yield versus atomic mass of the target material, which was related to the heat sublimation of the material that is roughly equal to the surface binding energy of the material. He determined that the yield was inversely proportional to the surface binding energy. These trends are shown in Figure 2-31.

In the sputtering, a threshold projectile energy must be produced to initiate particle ejection that is also related to the surface binding energy. These values have been measured experimentally for a variety of materials, and the values for Ni and Ti are shown in Table 2-3. Theoretical values of threshold energy can be calculated using a simplified hard sphere collision model that predicts the amount of energy transfer for a projectile to a target atom and their final direction after impact, which can be determined by conservation of momentum. Mahan [1999] used this model and developed the following equation for the threshold energy assuming collision cascade of 4 atoms.

$$E_{th} = \frac{4U_{sb}}{\gamma} \qquad (2-2a)$$

$$\gamma = \frac{4m_p m_r}{(m_p + m_r)^2} \qquad (2-2b)$$

where U_{sb} is the surface binding energy , γ is the projectile energy transfer function, m_p is the mass of the projectile, and m_r is the mass of the target atom.

Table 2-3. Threshold Energy in (eV) for Argon Sputtering.

Element	U_{sb}[a]	γ	Theoretical E_{th}	Experimetal[b] E_{th}
Ti	5.10	0.992	20.6	32
Ni	4.60	0.964	19.1	24

[a] Thermodynamic data, $U_{sb}=\Delta_{sb}H(298\ K)/N_a$, from Weast [1975]
[b] Anderson and Bay [1981]

After the threshold energy is reached, there is a sharp increase in yield with the projectile kinetic energy, followed by constant yield with increased ion energy [Mahan, 1999]. Figure 2-32 shows the yield curves for tungsten as function of the projectile energy. The general shape of the yield curves are due to the energy transfer mechanisms in the collisonal cascade and the nuclear stopping power of the projectile, which is the rate of nuclear energy loss of the projectile per unit distance in the target material [Mahan, 1999]. The downward trend in the Tungsten yield data at high ion energies is due to the decreased nuclear energy loss probability in the near-surface region and the electron energy loss, which is a projectile stopping mechanism that does not generate recoils [Mahan, 1999].

Argon is the typical choice for sputtering gas used in commercial processes because it is inexpensive and gives moderately good yields. However, heavier noble

gases can result in much higher sputtering rates. Figure 2-33 shows the effect of projectile type on sputter yield as a function of target atomic mass in the form of contour plots. For heavy atomic mass targets, the yield increases with increasing projectile mass, while lighter mass targets have a maximum yield at intermediate projectile masses, usually Krypton. The behavior of the projectile mass on sputter yield is related to variations in the projected range of projectiles in the target [Mahan and Vantomme, 1999]. If the projectile can transfer most of its energy to atoms that are near the surface, it will lead to higher sputtering rates. Thus, heavy mass projectiles in light atomic mass targets will have longer projectile ranges and will transfer most of their energy to atoms at deeper depths in the target, which results in fewer ejected recoils.

In addition to projectile mass, the angle of incidence of the energetic ion can affect the sputtering yield. The increase in sputtering at specific angles is related to the penetration depth in atomic lattice, where shorter depths lead to higher sputtering rates. Thus, the yield is inversely proportional to depth. Assuming a given, the projected range of a projectile at a fixed ion energy and mass, the depth of penetration varies with the cosine of the angle of incidence measured from the surface normal (depth=$R_p\cos\theta$). This would indicate that maximum yield would be obtained at glancing angle near 90°. However due to high probability of reflection or escape of the still-energetic projectile at high angles of incidence, the number of recoils produced is greatly reduced, and thus the sputter yield is reduced [Mahan, 1999]. Yamamura *et al.* have performed experimental studies on angle of incidence and developed empirical relations of yield as a function of projectile incidence angle. Figure 2-34 shows Yamamura's theoretical calculations of

yield compared with experimental results that show a yield maximum for incidence at around 70° for several materials.

Lastly, target condition has a strong effect on the sputtered yield. The presence of oxide layers, evolution of surface morphologies during sputtering, and the accumulation of implanted ions can cause reproducibility problems in yield results [Mahan, 1999]. Towsend *et al.* recommended that yield measurements be performed on targets which have achieved steady state by previous conditioning such that the yield is constant with further sputtering. The acceptable steady state of the target surface is accomplished for an ion dose of 10^{16} ions/cm^2 that amorphorizes the surface without blistering[10]. The effects of the target surface morphology on sputtering will be discussed in more detail later.

Much of the sputtering yield data found in literature are determined experimentally, and many of the theoretical models and formulae are empirically related to experimental data. Matsunami *et al.* [1984] has compiled a broad range of sputtering yield data and developed at empirical yield formula that is described below.

The empirical formula for yield by Matsunami is as follows.

$$Y(E) = 0.42 \frac{\alpha^* Q s_n(\varepsilon)}{U_{sb}[1 + 0.35 U_{sb} s_e(\varepsilon)]} \bullet \frac{8.478 Z_p Z_r m_p}{(Z_p^{2/3} + Z_r^{2/3})^{1/2}(m_p + m_r)} \bullet \left[1 - \left(\frac{E_{th}}{E}\right)^{1/2}\right]^{2.8} \qquad (2-3)$$

where U_{sb} is the surface binding energy, Zp and Zr are the atomic number of projectile and target respectively, m_r and m_p are the mass of recoil and projectile, and E is the energy of the projectile. The three empirical parameters are α^*, Q, and E_{th}, which physical meaning were not explained in detail. α^* and E_{th} are calculated using the

[10] Macroscopic erosion phenomena caused by occluded gas [Scherzer, 1983].

following empirical formulas, and Q is tabulated in Appendix B of Chapter VII in Physical Vapor Deposition of Thin Film by Mahan [1999].

$$\alpha^* = 0.08 + 0.164 \bullet \left(\frac{m_r}{m_p}\right)^{0.4} + 0.0145 \bullet \left(\frac{m_r}{m_p}\right)^{1.29} \qquad (2-4)$$

and

$$E_{th} = U_{sb} \bullet \left[1.9 + 3.8 \bullet \left(\frac{m_r}{m_p}\right)^{-1} + 0.134 \bullet \left(\frac{m_r}{m_p}\right)^{1.24}\right] \qquad (2-5)$$

The reduced energy is given by the following.

$$\varepsilon(E) = \frac{0.03255}{Z_p Z_r (Z_p{}^{2/3} + Z_r^{2/3})^{1/2}} \bullet \frac{m_r}{m_p + m_r} E \qquad (2-6)$$

Lindhard's elastic (nuclear) reduced stopping cross section is approximated with Equation 2-7.

$$s_n(\varepsilon) = \frac{3.441\sqrt{\varepsilon}\ln(\varepsilon + 2.718)}{1 + 6.355\sqrt{\varepsilon} + \varepsilon\left(-1.708 + 6.882\sqrt{\varepsilon}\right)} \qquad (2-7)$$

The inelastic (electronic) reduced stopping cross section is approximated in Equation 2-8.

$$s_e(\varepsilon) = 0.079 \bullet \frac{(m_p + m_r)^{3/2}}{m_p^{3/2} m_r^{1/2}} \bullet \frac{Z_p^{2/3} Z_r^{1/2}}{(Z_p^{2/3} + Z_r^{2/3})^{3/4}} \varepsilon^{1/2} \qquad (2-8)$$

Table 2-4 displays yield calculations for Ti, Ni, and Pd for various projectile energies using Matsunami *et al.* formulas along with experimental data by Vossen. The empirical calculation of yield using Matsunami are close to the values reported by Vossen but slight differences exist, and the disparities increase with increasing ion energy and recoil mass. The disparties between experimental and empirical calculated yield can be explained by a deviation from the assumed binary collision model that occurs at high ion energies and in materials with low surface binding energies and high mass [Mahan, 1999]. In general, Matsumani et al. formulas are well established and are used by many researchers, hence

their yield data calculated for Ni, Ti, and Pd will be in the remaining discussion. As will be seen later, the critical question regarding the use of these empirical equations such as these concerns the correct valve of U_{sb} for a species in the alloy. Though U_{sb} may be higher for Ti than Ni in monoatomic targets, it is not at all clear that this would be the case for the same species bound in the intermetallic compound.

Table 2-4. Sputtering Yield Data for Ni, Ti, and Pd.

Element	**Nickel**	**Titanium**	**Palladium**
Surface Binding Energy in eV (Weast, 1975)	4.6	5.1	4.22
Surface Binding Energy in eV (Gschneider, 1964)	4.47	4.9	3.91
Surface Binding Energy in eV (Matsunami, 1984)	4.44	4.85	3.89
Usb, best	4.50	4.95	4.01
Q (Matsunami, 1984)	1.06	0.58	1.1
Atomic Mass	58.6934	47.867	106.42
Z	28	22	46
alpha-star	0.295	0.275	0.374
Sputtering Threshold Energy, Eth	21.2	25.9	15.1
epsilon(E)	0.00382	0.0035	0.00193
Sn(epsilon)	0.154	0.149	0.119
Matsunami Yield at 200 eV (atoms/ions)	0.45	0.19	0.75
Matsunami Yield at 300 eV (atoms/ions)	0.66	0.3	1.1
Matsunami Yield at 600 eV (atoms/ions)	1.1	0.52	1.73
Vossen Experimental Yield at 200 eV (atoms/ions)	0.7	0.2	1.0
Vossen Experimental Yield at 600 eV (atoms/ions)	1.5	0.6	2.4

2.2.4 Sputtering Sources

2.2.4.1 Magnetron Planar Diode

Magnetron Sources were developed in the early 1970s and are capable of higher deposition rates than simple diode sources. In simple diodes, the secondary electrons

emitted from the target are typically lost to anode or walls. Thus, secondary electrons in a simple diode have a low probability to impact ionize the sputtering gas. If the path of an electron were lengthened then it would have a higher probability to impact an ion. Magnetron sources use a magnetic field, which is parallel to the target surface and perpendicular to the applied electrical field, to trap electrons near the surface of the target. The trapping effect occurs by the drift of electrons in the –E x B direction creating a cycloidal motion, as shown Figure 2-35. Since many of the electrons are confined near the surface of the target, there is a higher probability to ionize the neutral atoms. Thus, the plasma is intensified in this region due to increased impact ionization. This leads to a higher ion current density that results in a higher deposition rate, and sputtering is possible at much lower pressure with magnetron than with a simple diode.

The motion of the electrons in a planar–ring magnetron is shown schematically in Figure 2-36 (c). The radius of the electron motion is defined in Equation 2-9 and 2-10 [Mahan, 1999].

$$F = qv \times B \tag{2-9}$$

where F is exerted force on the electron, q is the charge of the electron, v is the velocity of the electron, and B is strength of the magnetic field.

$$r = \frac{m_e v}{qB} \tag{2-10}$$

where r is radius of gyration of the electron and m_e is the mass of the electron.

Assuming the electron is initially at rest on the target, it is deflected away from the target when a negative voltage or electrical field is applied. The force of the magnetic field deflects electrons back towards the target at a radius described in Equation 2-10.

The maximum height of the electron's deflection from the target surface is defined in Equation 2-11 [Green, 1976].

$$y_{max} = \frac{1}{B}\left[\frac{2m_e}{q}(V - V_T)\right]^{1/2} \qquad (2-11)$$

where y_{max} is the maximum deflection and $(V\text{-}V_T)$ is the cathode fall.

The continuous path of the electrons is annular in shape due to the E x B field that develops a high concentration of ions above a region, which is called the plasma ring. Subsequently, the target is eroded much more quickly in this region and creates a macroscopic erosion profile known as a 'racetrack' [Bunshah, 1994]. Thus, the main disadvantage of a planer ring magnetron is poor target material utilization. Later, we will discuss whether or not the development of this profile can affect composition in conjunction with the angular distribution of the sputter flux.

2.2.4.2 Triode Source

Triode magnetrons use an additional electrode independent of the target to sustain the plasma. A typical triode configuration is shown in Figure 2-36 [Bunshah, 1994]. Electrons are emitted by a thermionic filament and are used to replenish the plasma electron density in addition to the secondary electrons emitted by ion bombardment. This relaxes the ionization requirement for sustaining a discharge, and consequently, low working gas pressures and cathode voltages[11] can be used. Confining the electrons with an axial applied magnetic field minimizes the radial plasma losses, however the field produces distortions that cause uneven distribution of ion current over the area of the

[11] Pressure between 0.5 and 4 mTorr and applied voltage (100-500 V) can have ion currents of several amperes [Bunshah, 1994].

target. Typically, the target is eroded in the shape defined by the parallel path of the electrons across the target, and due to the axial confinement of the magnetic field, the outer edges of the target are eroded less efficiently. This causes a U-shaped profile known as 'saddling'. The saddling profile is somewhat less pronounced than the 'racetrack' profile of the diode magnetron and does not create steep sloping surfaces. This may be the reason for more compositional uniformity in sputtered films as compared to magnetron diodes.

Triodes achieve much higher deposition rates than simple planar diodes at lower gas pressures and voltages. However, triodes are less accepted in industrial plasma processes due to problems in scalability, complex and expensive power supplies, and vulnerability of the thermionic filament to reactive gases [Busch, 1977].

2.2.5 Film Growth and Sticking Coefficients

It has been observed by electron microscopy that films form in a series of stages. These stages are shown schematically in Figure 2-37 and are as follows:

1. Nucleation- small nuclei are statistically distributed over the surface of the substrate
2. Growth of the nuclei and formation of large islands
3. Coalescence of the islands and formation of a connected network of empty channels.
4. Filling of the Channels to form a continuous film.

As the sputter particles impinge on the surface, they are adsorbed and are referred to as adatoms. The energy loss of the particle as it impinges on the surface is characterized by

the accommodation or sticking[12] coefficient that is defined in Equation 2-12 [Eckertova, 1977].

$$\alpha = \frac{T_c - T_v}{T_c - T_s} \qquad (2-12)$$

where T_c is the temperature corresponding to the energy of the incident particle, T_v is the temperature of emitted particle, and T_s is the substrate temperature.

The sticking coefficient varies from 0 to 1, where 0 refers to elastic reflection of the particle and 1 refers to complete accommodation or sticking on the surface. It has been found that the sticking coefficient is generally 1 if the incident particles are less than or equal to 25 times the desorption energy on the substrate, which is around 1-5 eV for most materials [Eckertova, 1977]. Considering the energy distribution of sputter particles for a linear cascade defined by the Thompson[13] formula (Equation 2-13), most of sputter particles ejected for the target have energies equal to half the surface binding energy.

$$dY / dE_o \propto \frac{E_o U_{sb}}{(E_o + U_{sb})^3} \qquad (2-13)$$

where Y is the yield and E_o is the energy of the recoil.

Most materials have surface binding energy 1.5 –8 eV, and the energy of particles impinging on the substrate is typically much less due to scattering and thermalization events during transport through the sputter gas. Therefore, most sputtered particles do not posses the energy to readily desorb from the surface, even at high substrate temperatures. The kinetic energy that the sputtered particles do posses aides in nucleation and island formation by encouraging migration of adatoms thru surface diffusive jumps. The

[12] This sometimes is also referred to as condensation coefficient, and different literature sources interchange the names of this parameter but all have same general meaning.

probability of desorption is estimated by considering the mean diffusion time to physically or chemically absorb at preferred nucleation sites, and the mean residence time of adatoms [Eckertova, 1977]. Typically, diffusion times and distances are short due to high deposition rates in sputtering, and re-evaporation or desorption does not significantly reduce the condensation rate of the growing film.

There are many factors that can affect the quality of the growing film, like substrate temperature, chemical nature, crystallographic structure, and surface roughness [Eckertova, 1977]. In addition, the number density of residual reactive gas particles is an important factor since they can affect the composition and mechanical properties of the film. As discussed earlier, the ultimate base pressure is below 10^{-7} Torr, and the use of pure sputtering gas sources can greatly reduce the partial pressures of these containments. Sputtering gas incorporation[14] can also have adverse effects of the mechanical properties by reducing ductility of the film. In addition, energetic neutrals, negative ions and high-energy electrons that are accelerated across the Crookes Dark Space strike with high energy, and at high doses they can transfer a significant amount of thermal energy to the growing film. This can occur especially in the case of the so-called unbalanced magnetron that has magnetic flux lines that intersect the substrate and causes electrons to reside near the surface of the substrate, as shown schematically in Figure 2-38. The energy of incident sputter particles and the heat generated by particle bombardment on the substrate plays an important role in the growth and development film microstructures.

---

[13] The formula shows a maximum number of sputter particles at $U_{sb}/2$ and a rapid $(1/E_o)^2$ falloff at higher energies.

[14] This is caused by energetic sputtering gas ions and neutrals, which are reflected by the target during sputtering, striking the surface of growing film.

Thus, sputter parameters, such as working gas pressure, substrate temperature, and sputtering power, can have key effect development of certain microstructures.

2.2.6 Sputter Deposition of Alloys

An important advantage of sputter deposition is that the films formed have the same composition as the target, provided that the following conditions exist [Bunshah, 1994]:

1. The target is maintained sufficiently cooled such that bulk diffusion of constituents does not occur.
2. The target does not decompose.
3. Reactive gas and containments are not present.
4. The sticking coefficients are the same for all the components.
5. The gas-phase transport is the same for all the components, such that composition shifts of the film relative to target do not occur due to differences in thermalization and angular distributions of sputter species.
6. Preferential resputtering of a particular component does not occur.

The sputtering of alloys is complex and films compositions are in reality affected by deposition parameters given in the above list. The sputtering yields of components in alloys will not be the same as yields measured and calculated for pure elements, since the surface binding energies are different in the alloy [Bunshah, 1994]. If the surface binding energies are similar, the component with lighter mass will sputter more readily, and if the masses are similar, then the more weakly bonded species will sputter faster [Sigmund,

1980; Coburn, 1979; Anderson, 1981]. Preferential sputtering yields in alloys will have an effect on surface morphology as well films composition, which is discussed below.

2.2.6.1 Topographical Evolution of Multi-component Targets

The details of ion/surface interactions of multi-component materials are poorly understood and quite complex. Consider the case of a homogenous target that is composed of two elements that have different sputtering yields. During the initial stages of target sputtering, the component with higher yield will sputter more readily from the surface, which enriches the sputter flux in that component, and the composition of the target surface will become lean in the high sputtering component. This surface development continues until the lower sputter yield component surface concentration becomes high enough that sputtering yields of both the high and low components equilibrate (see Figure 2-39). This surface condition is known as the steady state altered layer, which creates a sputter flux equal to the bulk target composition. The transition period to form this alter layer depends on the method of target manufacture, the alloy, and deposition process. This transition period to a steady state condition can be long for hot pressed targets made for coarse powders (50-130 μm), which may require 20 μm of target material to be sputtered to achieve steady state. [Dahlgren, 1972]. The thickness of this surface altered layer is a measure of the escape depth of recoils, which depends on the target material and sputtering conditions [Bunshah, 1994; Mahan, 1999]. Typically, thickness can range from a few nanometers to several μm [Eltoukhy, 1980; Gillam, 1959; Greene, 1978].

Sputtering of two-phase alloys in which the phases have significantly different sputter yields can develop an irregular surface topography [Navinsek, 1976; Nobes, 1969; Carter, 1971; Sigmund, 1973]. The faster sputtering material will erode quickly and remove material around the slower sputtering phase or impurity. This results in etch pits, ridges, and a surface topography phenomena known as cones, which are shown schematically in Figure 2-40. The angles of the cones are related to incident ion angle that results in the highest sputter yield. Lee [1994] observed the formation of etch pits, ridges, and cone in the sputtering of Ni-rich TiNi targets containing precipitates, which are shown in Figure 2-41. These cones will eventually be sputtered away but will expose new impurities and second phases, which will result in the formation new cones.

The sputter flux will reach steady state and have the same composition as bulk target after an incubation time required to develop the altered surface layer and cone structures. This period of time is typically referred to as the target "burn in" [Bunshah, 1994], and most commercial sputtering processes presputter the target before depositing a thin film. Since there are many factors that can affect the required time for burn in, little is known about the sputtering times required to condition the target surface, which could be a few minutes to several hours. Mahan [1999] suggests that the appropriate target 'burn-in' is accomplished by presputtering for 1 hour. Evidence in this study for powder-metallurgy Ti, Ni, Pd targets indicates that this period may be considerably longer.

2.2.7 Effect of Recoil Angular Distributions on Film Composition

Behrisch [1981] stated, "For normal incidence that angular distribution may mostly be described in a first approximation by a cosine distribution." However, Wehner

et al. [1960] has observed differences in angular distribution between elements, and Olson et al. [1979] has found differences in the angular distributions between constituents in alloys that vary with incident ion energy. The cosine law of emission is given by the following equation.

$$j_{\Omega}(\theta) = Yz^{+}\cos\theta/\pi \qquad (2-14)$$

where j_{Ω} is the angular distributed emission flux, Y is the sputter yield, z^{+} is the ion impingement rate, and θ is emission angle.

This cosine law is related to isotropic angular distribution of recoil velocities in the collision cascade over an infinitesimal area on an ideal sputter source, but in general, the extended source overall can be described with an under-cosine type of distribution [Mahan, 1999]. Blech *et al.* developed an expression for describing angular distributions for real sputtering sources, which is shown in Equation 2-15.

$$\frac{dY}{d\Omega} = Y_{total} \bullet \frac{\cos\theta}{\left(\rho^2 \sin^2\theta + \cos^2\theta\right)} \qquad (2-15)$$

where Y_{total} is the total integrated yield, ρ is an empirical parameter, and $d\Omega$ is the differential solid angle in the direction of emission.

$\rho<1$ gives an under-cosine distribution, and $\rho>1$ give an over-cosine distribution. Information on the mass and Z-dependence of ρ are scant in the literature, but the data ,which exists, strongly suggests that ρ is more overcosine for less massive species in an alloy [Olson, 1979].

The type of angular distribution is related to the preferred angle of ejection. If the preferred direction of emission is normal to the target, the angular distribution has an over-cosine shape. Likewise, if the preferred direction of emission is more parallel to the

target, the distribution has an under-cosine shape. These distributions are shown schematically in Figure 2-42. As mentioned above, the lighter species of an alloy will tend to have over-cosine distribution when the ion energies are greater than 100 eV [Olson, 1979]. This is related to binary collisions between two species that have different masses. The lighter mass species is more likely to backscatter at angles that would tend to favor ejection in normal direction, based on the reflective collision model developed by Olson [1979].

Murakami *et al.* used Olson's model to explain the lateral composition shifts in binary alloy Tb_xFe_{1-x}. Using an experimental setup that collects films at various angles with the target, they showed that the lateral composition shift was significant and had opposite compositional effects for two different types of targets[15]. The setup and results of their experiment are shown in Figure 2-43. The composition shift in the compound (alloy) target was explained to have resulted by mechanisms described by the Olson's reflective model. The observed enrichment of the lighter mass Fe at center positions was attributed to a preferred emission normal to target (over-cosine), while Tb was concluded to have an under-cosine distribution causing enrichment at lateral position away from the target. The films that were deposited from the composite (powder) target enriched in Tb in the center and Fe at lateral position away from the center of target, which was opposite of the trend observed in the compound target. The composite target was composed of large distinct regions of pure elements, and the sputtering mechanism can be assumed to be similar to pure materials. Thus, the angular distributions were concluded to be similar to pure elemental results. Since Ni, Mo, Fe, Pt, and Ge were reported to have under-

cosine distribution by Wehner *et al.* [1960], it was assumed that elemental Tb had a more over-cosine distribution than Fe and thus enriched at the center positions. It is obvious from work of Murakami *et al.* that angular distributions can have a strong effect on film composition.

For oblique ion incidence, the angular distribution has an asymmetric distribution, where the maximum yield is shifted to the opposite side (as compared to the incidence angle) of the surface normal. These asymmetric distributions were observed in Si at an oblique angle of 60° by Okutani *et al.* [1980], and the preferred ejection angle from the surface normal was found to be 4.9° for 10 keV Ar^+. Betz *et al.* [1970] correlated the sputtering yield to preferred emission angle and developed a universal curve to describe the relationship, which is shown in Figure 2-44. At high yields (over 50 atoms/ion), the emission angle is nominally zero, while emission angle approaches 90 ° for yields under 2 atoms/ion.

2.2.8 Effects of Thermalization on Thin Film Composition and Microstructure

Most ballistic trajectory models for sputtering and evaporation assume that the mean free path is much longer than the throw distance (the distance from the substrate to the target). In evaporation and ion beam assisted sputtering[16] that operate at pressures of 10^{-6} and 10^{-4} Torr, respectively, the mean free paths of both processes would be greater than 30 cm. Thus, the assumption of longer mean paths than throw distances is valid for typical film deposition setups that use throw distances of 5-10 cm. In the case of

---

[15] The compound target was a homogenous alloy manufactured by hot pressing powders. The composite target was manufactured by randomly embedding 8mm Tb disk into 125 mm Fe plate.

[16] This is a method of sputtering using a separate ion gun to generate the projectiles.

magnetron sputtering processes that operate at pressures on the order of 1-5 mTorr, the mean free path is on the order of a few centimeters, furthermore, non-magnetic assisted diodes that operate at high pressures have even shorter mean free paths. Thus, the sputtering flux in magnetron deposition may be appreciably scattered and diffuse [Mahan, 1999].

The scattering is caused by collisions between the energetic sputter particles or reflected neutrals and sputter gas. This transfers energy for energetic particles to the sputtering gas that can reduce the characteristic temperature[17] of sputter particles (several thousand degrees) to the temperature characteristic of plasma sputter gas (~500 K). This process is termed thermalization. The reduction in energy of these particles can affect properties of the growing films, particularly the microstructure. Thermalization can be beneficial since it increases film thickness uniformity by creating a diffuse distribution of sputter particles that gives better composition control by reducing the preferential resputtering of constituents in alloy films, which is discussed in the next section.

The fraction of thermalization can be defined by the following equations by Mahan [1999].

$$F = 1 - e^{-y/k'\lambda} \qquad (2-16)$$

where y is the throw distance, k' is an empirical parameter (often on the order of 10), and λ is the mean free path defined by equation 2-17 and is the distance traveled before the first collision occurs.

$$\lambda = \frac{kT}{\sqrt{2}\pi d^2 P} \qquad (2-17)$$

[17] 5 eV is equivalent to 60,000 K, which is a typical value from Thompson's assumption of sputtering particles having half the surface binding energy.

here, k is the Boltzman constant, P is the pressure, d is the particle diameter, and T is the temperature.

Table 2-6 shows mean free paths of Ti, Ni, Pd, and Ar at various pressures and temperatures.

Table 2-5. Mean Free Paths[18] of Ti, Ni, Pd, and Ar.

Mean free path at 300 K (mm)				
Pressure (mTorr)	2.5	3	4	4.5
Nickel	45.6	38	28.5	25.3
Titanium	32	26.7	20	17.8
Palladium	37.3	31.1	23.3	20.7
Argon	19.1	15.9	11.9	10.6
Mean free path at 800 K (mm)				
Pressure (mTorr)	2.5	3	4	4.5
Nickel	121.5	101.3	75.9	67.5
Titanium	85.3	71	53.3	47.4
Palladium	99.5	83	62.2	55.3
Argon	50.9	42.5	31.8	28.3

It is obvious from Table 2-5 that nickel has the longest mean path of all the species, since it has the smallest atomic diameter. The mean free path is a strong function of temperature, which is related to the reduction of gas density at higher temperatures and thereby reduces the probability of interactions with sputter particles. Table 2-6 shows the thermalization fraction for Ti, Ni, and Pd at different working gas pressures and distances assuming k'=10.

[18] The values chosen for pressure, temperature, and working distance will become obvious in Chapter 4, since these values correspond to experimental setup parameters.

Table 2-6. Thermalization Fractions of Ti, Ni, Pd, and Ar.

	Fraction of Thermalization at 300 K, 2.5 mTorr, and y=131 mm (%)	**Fraction of Thermalization at 300 K, 3 mTorr, and y=131 mm (%)**	**Fraction of Thermalization at 300 K, 4 mTorr, and y=131 mm (%)**	**Fraction of Thermalization at 300 K, 4.5 mTorr, and y=131mm (%)**
Nickel	25	29.2	36.9	40.4
Titanium	33.6	38.8	48.1	52.2
Palladium	29.6	34.4	43	46.8
Argon	49.6	56.1	66.6	70.9
	Fraction of Thermalization at 300 K, 2.5 mTorr, and y=75 mm (%)	**Fraction of Thermalization at 300 K, 3 mTorr, and y=75 mm (%)**	**Fraction of Thermalization at 300 K, 4 mTorr, and y=75 mm (%)**	**Fraction of Thermalization at 300 K, 4.5 mTorr, and y=75 mm (%)**
Nickel	15.2	17.9	23.2	25.6
Titanium	20.9	24.5	31.3	34.4
Palladium	18.2	21.4	27.5	30.3
Argon	32.5	37.6	46.6	50.7
	Fraction of Thermalization at 300 K, 2.5 mTorr, and y=67 mm (%)	**Fraction of Thermalization at 300 K, 3 mTorr, and y=67 mm (%)**	**Fraction of Thermalization at 300 K, 4 mTorr, and y=67 mm (%)**	**Fraction of Thermalization at 300 K, 4.5 mTorr, and y=67 mm (%)**
Nickel	13.8	16.2	21	23.3
Titanium	18.9	22.2	28.5	31.4
Palladium	16.4	19.4	25	27.6
Argon	29.6	34.4	42.9	46.8
	Fraction of Thermalization at 800 K, 2.5 mTorr, and y=75 mm (%)	**Fraction of Thermalization at 800 K, 3 mTorr, and y=75 mm (%)**	**Fraction of Thermalization at 800 K, 4 mTorr, and y=75 mm (%)**	**Fraction of Thermalization at 800 K, 4.5 mTorr, and y=75 mm (%)**
Nickel	6	7.1	9.4	10.5
Titanium	8.4	10	13.1	14.6
Palladium	7.3	8.6	11.4	12.7
Argon	13.7	16.2	21	23.3
	Fraction of Thermalization at 300 K, 2.5 mTorr, and y=67 mm (%)	**Fraction of Thermalization at 300 K, 3 mTorr, and y=67 mm (%)**	**Fraction of Thermalization at 300 K, 4 mTorr, and y=67 mm (%)**	**Fraction of Thermalization at 300 K, 4.5 mTorr, and y=67 mm (%)**
Nickel	5.4	6.4	8.4	9.4
Titanium	7.6	9	11.8	13.2
Palladium	6.5	7.6	10.2	11.4
Argon	12.3	14.6	19	21.1

The effect of the mean free path on thermalization is obvious, since the species with the lowest mean free path will have the highest amount thermalization. Large relative differences in thermalization can affect the composition of the film by the preferential reduction in the flux of one species relative to the other even at steady state conditions where the sputter flux has the same composition as the target.

Turner *et al.* [1992] calculated the fraction of the incident flux which would reach the substrate after suffering scattering events during transport, as function of atomic mass and pressure, using Monte Carlo simulations at a throw distance of 5 cm in Argon, which is shown in Figure 2-45. They considered both the mass of the species and its binding energy, which was introduced to account for the initial energy of the sputtered species in the sense that higher binding energy would imply higher initial energy. Turner did not explicitly simulate deposition rates for Ni or Ti, but did produce results for Na, Sn, C, Cd, Pd, Nb, Pb, Au and W. These results are shown in Figure 2- 46 with a superimposed set of estimated contour lines giving the percent of atoms that actually reach the substrate, as a function of binding energy (y-axis) and mass (x-axis). The contour lines indicate that Ti and Ni would suffer the same amount of scattering and reduction incident flux.

The thermalization distance was quantified by Westwood [1978], which was calculated as function of pressure for a variety of mass and energy regimes that are shown in Figure 2-47. His result shows that thermalization distances are short for most sputter particles masses at pressures commonly used during sputter desposition.

Somekh [1984] did computer simulations on the thermalization of different atomic mass sputter species in different types working gas with primary interest in the effective energy reduction of particles according to Thompson sputter particle energy

distribution. He based his results (see Figure 2-48) on pressure- throw distance products and showed that light mass atoms retain more of their initial energy than heavy mass atoms above 100 Pa-mm. The unambiguous conclusion of these studies is that thermalization is significant under practical sputter conditions, and its effect on composition and microstructures of sputtered thin films cannot be ignored.

2.2.9 Effects Preferential Resputtering and Sputter Yield Amplification on Composition

Resputtering is removal of sputter deposited material by bombardment of energetic neutrals or energetic ions. Resputtering can reduce the net condensation flux as an inadvertent result of the bombardment of the target by energetic ions, which recoil or reflect as neutrals from the target surface at energies on the same order of magnitude as the cathode fall potential [Hoffman, 1990]. Resputtering of the film can be as little as few percent to values that approach 100 %. Applying a negative voltage to the substrate can increase the resputtering rate, thru increased ion bombardment, which is know as biased substrate sputtering. This is beneficial for microstructure control since the heat generated by ion bombardment can increase diffusion processes and the development preferred microstructures. Hoffman [1990] measured the intrinsic resputtering of films for a variety of projectile types and target materials, and he found that the fraction of resputtering falls on a universal curve. Figure 2-49 shows the Hoffman results for the fraction of resputtered material as a function of atomic mass parameter (AMP) and the resputtering fractions of the Ti, Ni, and Pd (the AMP for these elements are shown in Table 2-7).

Table 2-7. Atomic Mass Parameters (against Argon).

Nickel	Titanium	Hafnium	Palladium	Copper
0.19004	0.09018	0.63424	0.45414	0.22801

Hoffman's results show that for heavy sputtering gas and light target atoms (AMP <0), the resputtering is a constant 3.5%, which is probably due to self-sputtering. While light gas atoms and heavy target atoms (AMP >0) are linearly related with the atomic mass, which is due to an increase in reflected neutrals from the sputter target as the target mass increases.

Resputtering can have an effect on composition when atomic species have intrinsic resputtering yield differences, like those that occur by sputter yield amplification. The sputter yield amplification (SYA) effect is an enhancement of partial sputter yields to values larger than those of pure elements [Berg, 1999]. The increase in partial sputtering yield is related to underlying substrate material and the thickness of the sputtering layer.

The mechanisms for SYA are related to the collisional cascades within the thin film. As mentioned earlier, typical collision cascades that result in ejected recoils occur at depths of few monolayers of atoms (1-2 nm). If the film thickness is on same order as the depth of the collision cascade and the underlying substrate is composed of heavier mass atoms (as compared to the film), a substantial fraction of the lighter film atoms in the collision cascade will be reflected off the heavier substrate atoms and back towards the surface. Since reflection occurs at small impact parameters, this mechanism is sensitive to the relative difference of atomic mass and not the atomic density of the materials. Furthermore, the lighter film atoms will lose very little energy due to a small

kinematical factor, thus reflection through multiple collisions between film and substrate atoms is a reasonable explanation for sputter yield increase [Berg, 1999]. The end result of increased backscattering of the lighter atoms is an increase in the density of collisional cascades, which are confined to the surface, and thus enhance the sputtering yield. Berg *et al.* performed computer simulations of partial sputtering yield of 1 nm thick Al layer on different Z (atomic number) substrates and show that as Z increases the partial sputtering yield increases (see Figure 2-50). This confirms that there is a possible SYA effect, since at high Z substrates the yield is amplified by twice the sputtering yield measured for pure Al.

For thin sputtering layers one or two monolayers thick, the mechanism is different than the one previously mentioned. The partial sputtering yield is independent of the atomic number of the substrate but it is dependent on the atomic density of the substrate. This is due to small thickness of the sputtering layer; the majority of the collision cascade density occurs in the substrate. Thus, the sputtering of a thin layer depends the collision cascade density of the substrate, which is roughly proportional with the atomic density of the substrate [Berg, 1999].

In addition, the SYA effect is observed in alloy target materials containing elements of differing mass [Berg, 1999]. The enhancement of the sputtering yield is related to projected range of the bombarding species, which is related to masses of the target material and projectile. The increase in energy loss of the projectile is in the near surface of the target. If a target is doped with a heavy species, the projected range of the projectile will decrease with increasing concentration of the heavier mass species. Thus, most of the projectile energy will be transferred to regions near the surface that increase

the density of collision cascades, resulting in an increased sputtering yield. Another result of the heavier species/ion interactions is that the ion will retain much more energy on reflection as compared to the interaction with the lighter mass species, due to kinematical fraction differences. Thus, the reflected ion can transfer more energy to near surface atoms. The consequence of doping the target with a heavier species is that the partial sputter yield of the light component can be double the value of the pure material yield. This conclusion is important when considering preferential sputtering, since the species in multi-element alloy target, which are preferential sputtered is not obvious from the pure element sputter yield data.

Preferential sputtering in target exists at early stages sputtering. However as mentioned earlier, the sputter flux will eventually be equivalent to the target composition due to the conservation of matter. This steady state condition does not occur in processes where preferential sputtering exists thru the whole process, like the resputtering of a growing film. Preferential resputtering will tend to decrease the composition of a species even though the steady state sputter flux is the same as the target composition. Thus, the film composition will have a different composition compared to the target. Preferential resputtering has been observed in a number of multi-component sputtering processes. For instance, Grace *et al.* have observed the selective resputtering of Bismuth in Bi-Sr-Ca-Cu-O films. Their results stated that Bi loss was strongly related to the working gas pressure, where increased loss was found at low working gas pressures and compositions that resemble the target stoichiometry at high pressures. Resputtering caused by the bombardment of growing film by energetic neutrals, and since thermalization of neutrals increases with increasing pressure, the resputtering rate was a strong function of the

working gas pressure. Selinder *et al.* also observed a preferential resputtering of Cu in YbaCuO films that was eliminated at high working gas pressure (>9 Pa). They also observed that Cu loss was a strong function of substrate temperature and concluded that relevant differences in sticking coefficients of the components resulted in the diminished Cu. Neither Selinder nor Grace *et al.* eluded to mechanisms which drive preferential resputtering. However, conclusions can be made based on the SYA effect and increase sputtering yields for the lost species.

CHAPTER 3 MATERIALS AND METHODS

The goal of the present work has been to study the effect of sputter deposition parameters on the composition of TiNi and TiNiPd thin films. The binary TiNi thin films were formed by two methods, d.c. magnetron and d.c. triode sputtering, and experiments were conducted to compare the effects of target erosion on composition between these two methods. Additional experiments were conducted to observe the effects of deposition parameters on the composition of TiNiPd from sputtered from powder-metallurgy targets. This chapter discusses the procedures used to fabricate the thin films and to gather data on composition, thickness, and transformation temperatures.

3.1 Materials

3.1.1 Binary TiNi Targets

The dc magnetron sputtering targets used in the binary composition study had a composition of $Ni_{51}Ti_{49}$, as supplied by Special Metals, Inc. and were electrical-discharge machined (EDM) from 76.2 mm wrought bar into 3" diameter 1/4" thick disks. The targets used in triode sputtering experiment were EDM-cut from the same bar stock as the diode targets but were machined into 2-1/4" diameter 3/8" thick disks. The surfaces of these targets were polished before use with 600 grit SiC paper to remove the hydrocarbon deposits caused by the EDM process, and then ultrasonically cleaned in acetone and isopropyl alcohol.

3.1.2 TiNiPd Targets

The targets used in TiNiPd experiments were produced by Pure Tech, Inc. and shipped to MSU Material Science Department by Al Knebel of Delpi Energy and Engine Management Systems. Each TiNiPd target was a 3" diameter, 1/8" thick powder metallurgy (P/M) disk that had the following composition as reported by Pure Tech, Inc.

Table 3-1. Nominal TiNiPd P/M Sputtering Target Compositions.

Target #	Composition, atomic %		
	Ti	Ni	Pd
Pd1	53.5	21.5	25.0
Pd2	53.5	20.25	26.25
Pd3	53.5	19.5	27.0

The three TiNiPd target composition were chosen to provide SMA sputtered thin films that would have 50 at. % Ti and 27 to 29 at. % Pd that would produce an austenite finish temperature between 200-225°C, that was determined from literature results shown in Figure 3-1 and 3-2. The additional 3.5 at. % Ti-enrichment was chosen to compensate for the expected Ti loss during sputtering observed in previous results [Grummon, 2000].

3.1.3 TiNiPd Target Chemical and Microstructural Analysis

Energy dispersive spectroscopy (EDS) was performed on the targets to gather information on composition to confirm the reported values by Pure Tech. However, due

to the extreme variability of the measurements, the results were inconclusive. This may have been a result of inappropriate standards, which were solid thin films rather than P/M materials similar in nature to the target. ZAF corrections were accomplished using software that accompanied the LINK EDS system.

Optical microscopy and metallography were performed to gain information about the P/M TiNiPd target microstructure. Target Pd1 was mechanically polished for metallographic observation with a sequence of silicon carbide papers and crystalline diamond polishing compounds to 0.25μ finish, and then ultrasonically cleaned in acetone and rinsed with isopropyl alcohol. To reveal the microstructure, a modified aqua regia etchant[1] was used that contained 2ml HCl and 10ml HNO_3. An optical photomicrograph was taken at 50X from target Pd1 and is shown in Figure 3-3. The microstructure is coarse and inhomogeneous with large features on the order of 200 μm. At a magnification of 500X, void porosity and reaction zones were visible, as well as zones of apparent unreacted pure metals, as seen in Figure 3-4. The observation of zones that contained pure metals coincided with slightly magnetic nature of the targets, since elemental Ni is magnetic.

Figure 3-5 displays a secondary electron image[2] of target Pd1 at 100X. The microstructure consisted of regions of pure Ti, Ni, and Pd, complex intermellatic regions, and numerous voids. When higher magnifications were used, like the SEM photomicrograph in Figure 3-6 taken at 1200X, the microstructure revealed complex

[1] The modified aqua regia is general etchant for nickel and palladium based superalloys and does not etch titanium.
[2] SEM images were acquire at an accelerating voltage 25KeV, a beam emission current of 140μA, a #3 objective aperture, and working distance of 8-6mm. Pd1 target was prepared using the procedure for metallographic observation.

reaction zones that may have resulted from partial melting during the manufacturing of the target. The inhomogeneous distribution was also apparent from X-ray EDS maps, which is displayed in Figure 3-7 at 1000X that show regions of elemental Ni, Ti, and Pd along with melted/reaction regions of combination of these elements.

A stereographic analysis was performed to determine the approximate void fraction in target Pd1 using the grid pattern shown in Figure 3-8. The volumetric void fraction was determined using $V=Q/N$, where Q is the number of grid points intersecting voids, and N is the total number of grid points (see Figure 3-8). The void volume fraction calculation was performed 10 times with different grid sizes, and the results were averaged. The volume fraction of void porosity was found to be ≈7.1%. The target was therefore concluded not to be hot isostatically pressed (HIPed), but was rather uniaxially hot pressed or simply sintered.

3.1.4 P/M Target Performance

The three TiNiPd powder-metallurgy (P/M) targets used in this study performed well in the 3" Torus 3M guns, allowing reliable plasma ignition at pressures below 2.5 mTorr. Early in the work, copper backing plates were soldered to the targets to increase their thickness to 1/4" in order to achieve the proper ground-shield gap in an older model of the 3" Torus-3M gun[3]. In one case, target heating at 250-watt power levels caused

[3] The Torus 3M design uses an enhanced magnet structure specifically designed for sputtering magnetic materials. Two guns were used in the study: One, built in 1990 (designated as the 'old' gun in Table 1) had apparently been damaged by overheating and was later replaced with a new unit. The old gun had a substantially weaker magnetic field but was still capable of producing high-quality films.

melting of the solder[4] holding the plate. For subsequent tests using a newly purchased gun, these plates were removed.

High void porosity was found during metallographic analysis, as discussed previously. This did not cause obvious problems, such as large virtual leaks from the voids, nor did the slight magnetic character of the targets. The latter factor would, however, need to be taken into account for thicker targets or for use in standard magnetron guns not equipped with enhanced magnet structures since it can reduce the deposition rate. The guns used in these studies did use an enhanced magnet structure specifically intended for magnetic materials, which gave good plasma performance at the expense of less efficient target utilization.

As mentioned previously, some question remained at the end of the study with respect to the actual target compositions, or the possibility that compositional uniformity had been compromised by uneven distribution of the powder components during manufacture. Finally, it should also be mentioned that no attempt was made here to determine the oxygen content of the as-supplied targets. Though none of the results implied that film oxidation had occurred, and oxygen contamination of TiNi alloys is notoriously difficult to identify[5] and cannot be completely excluded.

3.1.5 Substrates

Binary TiNi thin films were deposited on glass slides that were 3" X 1" X 1/8" thick, which were used in composition measurements as a function of cathode wear and

[4]The solder has a melting point of around 160 °C.
[5] Ti_2NiO oxides are isostructrual with Ti_2Ni, therefore making distinctions between the phases is almost impossible.

lateral distance from the cathode. The slides were adhered to the wafer platen with vacuum grade copper tape after cleaning with 15% HF solution, and rinsing with isopropyl alcohol, respectively. 2.5" square, 1/4" thick flint glass plates were used as substrates for the triode experiments, and were cleaned in the same manner as the glass slides. One corner of the glass plates was cut to use as a locater for the position of the plate with respect to the thermionic filament of the triode gun. 5" wafers of (100) p-type silicon wafers were used for TiNiPd thin film experiments. In addition, 5" silicon wafers with 100 nm oxide layers were used for TiNiPd thin films deposited and annealed at high temperatures. The silicon oxide layer acted as a diffusion barrier to stop the interdiffusion of Si in TiNiPd at high temperatures, which was known to cause the films to become brittle and have no apparent SME quality.

3.2 Sputtering Deposition Process

3.2.1 Binary TiNi Magnetron Diode Deposition Setup

Films were sputtered in a 28" Kurt J. Lesker (KJL) Supersystem-II apparatus equipped with CT 8 cyropump capable of ultimate pressures below $1X10^{-8}$ Torr (see Figure 3-9). The chamber was internally heated with quartz lamps to temperatures greater than 150°C for 24 to 48 hours to outgas residual water vapor and improve the vacuum. All films were deposited with base pressure better than $5x10^{-7}$ Torr. A 24.5" diameter aluminum octagon shaped substrate holder was constructed for this experiment, which had eight 2.5" square hole substrate positions (see Figure 3-10). Three glass slides were centered over the 2.5" square hole and adhered to substrate holder with vacuum grade copper tape. A KJL Torus 3-M magnetron sputter source (see Figure 3-11) was fitted

with a 3" diameter, 1/4" thick $Ti_{49}Ni_{51}$ target. Eight thin films[6] approximately 12.3μm thick were sputtered sequentially onto flint glass microscope slide substrates at ambient chamber temperature using a sputtering power of 250 watts, an argon working gas pressure of 4.5 m Torr, and a substrate-target distance of 78mm. Each deposition lasted for 3 hours, and the eight depositions (including a 30 minute cathode burn-in period) was predicted to have consumed approximately 75% of the total cathode life based on the estimated target thickness at the end of the deposition series.

3.2.2 Triode Deposition Setup

The triode experiments were conducted on a Simard Type 383 source and used a binary 2-1/4" diameter, 3/8" thick $Ti_{49}Ni_{51}$ target. The 2.5" square glass plates were placed over nine 2" holes, as seen in Figure 3-12. The cut end of the glass plate corresponded to the position relative to the thermionic filament. A system base pressure of $4x10^{-8}$ was obtained before deposition. The thin films were deposited at power 440 watts[7] with a thermionic filament current of 30A, an argon working gas pressure of 2.8mTorr, and working distance of 131 mm. This setup achieved a sputtering rate 0.8 nm/s with 2 hour sputtering time that produced nine films with an approximate thickness of 6.1μm. The target showed erosion profile known as "saddling", which is convex shaped erosion formed by path of energetic electrons emitted by the thermionic filament across the target. This profile can be avoided by rotating the target, which allows for better target

[6] One thin film deposition run deposited a thin film on three glass slides, and there were eight available positions on the substrate holder, which gives a total of 24 glass slides with deposited thin films.
[7] 440 watts sputtering corresponded to a sputtering voltage of 550Vand a current of 0.8A.

utilization. However, the target was not rotated in these experiments to observe the worse possible effects of the target profile on the compositional shift of the films.

3.2.3 TiNiPd Magnetron Sputtered Thin Film Deposition

Films were sputtered in KJL 28" chamber shown in Figure 3-9 with KJL Torus 3M magnetron sputtering source in a working gas of ultra-high purity argon. All the thin films were deposited at 250 watts on the constant power regulation setting of the Advanced Energy MDX1K sputtering power supply, which is capable of delivering 1kW at 1000V. A schematic of the thin film deposition chamber in Figure 3-13 shows the relative positions of pumps, sputter gun, furnace, and wafer platen. The typical setup for film deposition was a "sputter down" configuration where the gun was above substrates and the wafers were heated on the backside. The chamber, wafer furnace, and wafers were outgassed at 150, 600, and 575 °C, respectively, for 24-48 hours before sputtering to improve the vacuum. A few hours before each deposition runs a titanium sublimation pump, specially built for these experiments, was used to getter reactive gases, such as O_2 and H_2O, by evaporating Ti[8] unto the water-cooled walls of the sublimation pump. Typical oxygen partial pressures were below the measurement sensitivity of the Ametek Dycor Quadrupole residual gas analyzer ($P_{O2}<10^{-10}$ Torr), and water vapor partial pressures were below 1×10^{-8} Torr. All the films were deposited with initial base pressure better 5×10^{-7} Torr and most often better than 8×10^{-8} Torr.

Wafers were heated using a US Inc. four-inch non-contact inconel substrate heater that radiatively transfers heat to the backside of the wafer. The wafer temperature was

measured with a K-type 1/16" stainless steel sheathed grounded-tip thermocouple in contact with center of the wafer on the backside (see Figure 3-13). A 304 stainless steel wafer platen was specially constructed for this research and had eight positions that centered the wafers under the sputter gun (see Figure 3-14). The wafers were held in place by 1-2 oval shape clips that were bolted to wafer platen.

During deposition, thermal equilibrium with the sputtering process flux energy was reached approximately 20 minutes into the deposition run. When no furnace power was applied, the wafer backside temperature typically equilibrated about 175°C. Working distances of 75mm and 67mm were used, and the working pressure, which was held at 2.5 or 4.0 mTorr for most deposition runs, was carefully controlled with a micrometer flow valve and measured with an MKS capacitance manometer. Extreme care was taken to avoid atmospheric contamination of the working gas lines by careful purging of the lines before use and maintaining them at a constant 60-psi positive pressure.

The choice of deposition temperature was made on the basis of the measured crystallization temperature of the amorphous TiNiPd film, and deposition temperatures were explored above and below this crystallization temperature. A TA Systems 2250 DSC apparatus was used to measure the crystallization temperature of a film sputter from target Pd1 at room temperature. The unit was calibrated using a 99.9% pure Zn sample a heating rate of 5°C/min, and TA Systems DSC commercial software. Two DSC samples from specimen #0224001 were made from film delaminated from the Si substrate with sample weights of 5.5 and 4.4 mg, respectively. These samples were scanned at 5°C/min

[8] Titanium was evaporated from 85%Ti-15%Mo filament with 40A/3V sublimation power supply for 2 minutes at 15-minute intervals.

rate under a N_2 shield gas, and the crystallization temperature was found to be 480 °C, as shown in Figure 3-15.

A master table of deposition parameters and thin film characterization results for the TiNiPd films used in the composition study is given in Table 3-2. The designation old and new sputter gun used refers to identical KJL Torus 3M gun designs, however, tests on the older sputtering gun revealed the permanent magnetic assembly had been damaged and was replaced with new gun that had a stronger[9] magnetic field.

3.3 Qualitative Assessment of Film Appearance and Performance

Qualitative assessment of room-temperature ductility, adhesion, and shape memory were performed on all samples listed in Table 3-2[10]. Ductility was assessed by deforming a mechanically peeled sample by manual crumpling. If the film fractured it was considered to be brittle. Shape recovery was assessed for ductile films by observation of deformed films during indirect heating[11]. The adhesion test was based on the ease that the film could be delaminated from the wafer. Released films were often observed to curl extensively inward due to through-thickness stress variations.

[9] The new KJL Torus 3M gun had magnetic field strength of 1650 Gauss 10mm above the cathode cooling plate, while the old gun had 423 Gauss magnetic field strength.
[10] G,F,P symbols in Table 3-2 corresponds to a good, fair, and poor qualitative rating.
[11] Films were heated in an aluminum pan by butane lighter.

Table 3-2. Deposition Parameters and Properties

Specimen #	#02240001	#02250001	#03010001	#03020001	#03020001-AN-0518-500	#03030001	#03090001	#03100001
Gun Used	old	old	old	old	new	old	old	old
Target Pd%	25	25	25	25	25	25	27	27
Substrate	Si/ 5"	Si/ 5"	Si/ 5"	Si/ 5"	Free Film	Si/ 5"	Si/ 5"	Si/ 5"
Sputtering Power (watts)	250	250	250	250	250	250	250	250
Sputtering Voltage (V)	380	376	371	365	365	359	352	346
Deposition Temperature (°C)	165	615	556	530	530	531	174	605
Working Gas Pressure (mTorr)	2.5	2.5	2.5	2.5	2.5	2.5	2.5	2.5
Working Distance (mm)	75	75	75	75	67	75	75	75
Base Pressure ($1x10^{-8}$ Torr)	20	10	0.8	0.8	0.8	0.9	0.6	0.36
Sputter Time (Min)	62	95	93	90	90	90	60	90
Thickness (μm)	2.3	5.46	5.24	5.18	5.18	5.23	3.58	4.35
Post Anneal Temperature (°C)	-	-	-	-	505	500	-	-
Post Anneal Time (Min)	-	-	-	-	1440	5	-	-
Base Pressure at Heat Treatment ($1x10^{-8}$ Torr)	-	-	-	-	0.8	0.8	-	-
Crystallization Temperature (°C)	479	479	479	479	479	479	481	481
DSC Test Performed	yes	yes	yes	yes	no	no	no	no
Resistivity Test Performed	no	yes	yes	yes	no	yes	no	yes

Table 3-2 (cont'd).

Specimen #	#03220001	#04250001	#05160001	#05160001-AN-0605-750	#05290001	#05290002	#05290003	#05290004
Gun Used	old	new	new	new	new	new	new	new
Target Pd%	27	27	27	27	27	27	27	27
Substrate	Si/ 5"	Si/ 5"	Quartz	Free Film	Si/ SiO_2 5"	Si/ SiO_2 5"	Si/ SiO_2 5"	Si/ SiO_2 5"
Sputtering Power (watts)	250	250	250	250	250	250	250	250
Sputtering Voltage (V)	334	329	300	300	298	296	295	294
Deposition Temperature (°C)	549	509	480	480	601	574	518	548
Working Gas Pressure (mTorr)	2.6	2.5	2.5	4.0	4.1	4.1	4.0	4.0
Working Distance (mm)	75	67	67	67	67	67	67	67
Base Pressure ($1x10^{-8}$ Torr)	10	0.2	0.3	0.8	0.8	0.65	0.75	0.8
Sputter Time (Min)	91	105	90	90	45	45	45	45
Thickness (μm)	5.78	8.12	6.97	6.97	3.55	3.67	3.45	3.53
Post Anneal Temperature (°C)	-	615	-	557	-	-	-	-
Post Anneal Time (Min)	-	90	-	75	-	-	-	-
Base Pressure at Heat Treatment ($1x10^{-8}$ Torr)		0.3	-	30	-	-	-	-
Crystallization Temperature (°C)	481	481	481	481	481	481	481	481
DSC Test Performed	yes	no	no	no	yes	no	no	no
Resistivity Test Performed	no	no	no	no	yes	yes	no	no

Table 3-2 (cont'd).

Specimen #	#05290004-AN-0605-750	#05290003-AN-0624-750	#05290003-AN-0625-650	#05290004-AN-0628-600	#05290004-AN-0702-550	#07270003	#08030001	#08080001
Gun Used	new	new	new	new	new	new	new	new
Target Pd%	27	27	27	27	27	25	26.25	26.25
Substrate	Si/ SiO_2 5"	Si/ SiO_2 5"	Si/ SiO_2 5"	Si/ SiO_2 5"	Si/ SiO_2 5"	Si/ 5"	Si/ SiO_2 5"	Si/ 5"
Sputtering Power (watts)	250	250	250	250	250	250	250	250
Sputtering Voltage (V)	294	295	295	294	294	328	328	331
Deposition Temperature (°C)	548	518	518	548	548	425	425	425
Working Gas Pressure (mTorr)	4.0	4.0	4.0	4.0	4.0	4.0	4.0	4.0
Working Distance (mm)	67	67	67	67	67	67	67	67
Base Pressure ($1x10^{-8}$ Torr)	0.8	0.8	0.8	0.8	0.8	0.8	0.8	0.8
Sputter Time (Min)	45	45	45	45	45	60	60	60
Thickness (μm)	3.53	3.45	3.45	3.53	3.53	4.64	4.34	4.46
Post Anneal Temperature (°C)	575	748	655	600	550	-	-	-
Post Anneal Time(Min)	75	60	60	60	60	-	-	-
Base Pressure at Heat Treatment ($1x10^{-8}$ Torr)	30	50	55	20	0.45	-	-	-
Crystallization Temperature (°C)	481	481	481	481	481	479	482	482
DSC Test Performed	no	no	no	no	no	no	no	no
Resistivity Test Performed	no	no	no	yes	yes	yes	yes	yes

3.4 Resistivity Measurements

To gather accurate transformation temperatures in a non-destructive test, an electrical resistivity device was constructed (see Figure 3-16). The apparatus used a Jandel Macor four-point probe with a spring-load tungsten pins spaced 1 mm apart. The two outer probes were used to apply a constant current of 100mA, and the inner probes measured the voltage drop. The specimen was heated and cooled at constant 5°C/min by OMEGA PID temperature controller that measured temperature with a fine thermocouple wire near the contacting probes. The inner probe voltage drop and thermocouple voltage was output to a chart recorder, which plotted the voltage drop verses temperature.

3.5 Differential Scanning Calorimetry (DSC)

A TA Systems model 2250 DSC system using LN2 chiller was used to gather information about the transformation temperatures of TiNiPd thin films. The DSC was calibrated using a 21 mg pure indium sample at a heating rate of 10 °C/min. The DSC samples were prepared from film delaminated from the substrates, which were weighed on an electronic scale. The delaminated film was placed in specially designed TA Systems aluminum DSC pans, which were then sealed using a commercially supplied pan crimper. The DSC was programmed to equilibrate at 75°C, heat to 220°C at a rate 10°C/min, and cool to 75°C at a rate 10°C/min. The DSC curves were graphed and analyzed using the Universal Analyzer program supplied by TA Systems.

3.6 Thin Film Composition Measurements

3.6.1 Binary TiNi Composition Shifts Measurements due to Cathode Wear

Film compositions were measured by energy dispersive X-ray spectroscopy (EDS) on a Hitachi S-2500C scanning electron microscope (SEM) that was equipped with Link EDS X-ray spectrometer using the following setup for all measurements: objective aperture setting #3; detector-specimen angle 45°; specimen working distance of 15mm; accelerating voltage 25 keV; LaB_6 filament current 90μA; acquisition setup requiring a total spectral integral count of 10,000 Ti-Kα counts under a Ti Kα energy window between 4.347-4.668 keV; Ni Kα energy window between 7.287-7.668 keV; a dead time about 15% and count rate 1 kcps[12]; and beam rastered over a scan area of 3.3x4.1 mm (30x magnification setting). Since the films were thicker than 6μm, it was assured that no characteristic X-rays were generated from the substrates. The relative horizontal distance from the center of the cathode on the glass substrate was measured by the SEM stage micrometers and aligned by fudicial marks on the stage. Sixty X-ray spectra were taken for each specimen at the measured center-cathode position, while 30 spectra were taken at distances away from the cathode center for each specimen. The composition was determined by a ZAF correction of integral count ratio using a standard with a composition of $Ti_{49}Ni_{51}$.

[12] The count rate was constant for each specimen by an adjustment of the condenser lens setting.

3.6.2 TiNiPd Thin Film Composition Measurements

The composition study was performed on a Hitachi S-2500 C SEM that was equipped with Link EDS X-ray spectrometer operated a 25 keV with 140 μA emission current. The collection parameter were as follows: 50x magnification, 15 mm working distance, detector-specimen angle 45°, 2 kcps count rate, 30% deadtime, and 60 second preset livetime. Thin Film standards were used along with a Link ZAF correction software. The standards used were taken from sample #03020001, which was assumed to have a composition $Ti_{50}Ni_{20}Pd_{30}$ based on observed transformation temperatures and TEM microstructure analysis (see the section below). Spectra from the standard were collected first to develop the necessary ZAF correction factors and profiles[13], and then spectra from the unknown TiNiPd thin films were collected. Thirty spectra were collected for each unknown, which were tabulated and statistically analyzed.

3.6.2.1 TiNiPd Thin Film Composition Standard Preparation

Transmission electron microscopy (TEM) examination of a film that has been heat-treated to achieve thermodynamic equilibrium can be useful since the amount and type of precipitates formed gives unambiguous information on deviation from equiatomic stoichiometry. Typically in binary TiNi alloys, a long heat treatment of 24 hours at 500°C[14] will drive excess Ni out of solution and form Ni_4Ti_3 precipitates. Long hold times cause temperature cause the formation of large incoherent precipitate particles. If the alloy is titanium-rich, Ti_2Ni will be commonly observed, which are spherical in shape, and

[13] The ZAF correction factors and profiles were standardized every 15-20 minutes during the unknown spectra collection process.

often form at grain boundaries and other high-energy sites. Since palladium substitutes for nickel in the ternary alloys, the heat treatment processes and trends should be similar to binary alloys, but little is known on the precipitate structures that form in ternary compositions. An equilibration heat-treatment of a free standing TiNiPd thin film was performed on sputtered sample #03020001. A piece of this specimen was sandwiched between two quartz plates and vacuum annealed at 505°C for 24 hours to produce the specimen designated as 03020001-An0518-500 (See Table 3-2).

Figure 3-17 shows a schematic of sample preparation configuration. The specimen was placed on a wafer substrate heater in the sputter chamber and held in place by the slight tension of a thermocouple wire. The temperature of the film was calculated by averaging the temperature measured on the surface of the substrate heater and backside of the top quartz plate. The vacuum chamber was pumped down to a base pressure $6x10^{-8}$ Torr with a water partial pressure of $2x10^{-9}$ Torr and oxygen partial pressure of $4x10^{-10}$ Torr. The temperature was slowly ramped to 505°C for 1 hour then held at that constant temperature for 24 hours at which time the substrate heater was turned off to let the film cool slowly to room temperature. Subsequent TEM observation showed the existence of martensite a room temperature with structure shown in Figure 3-18. The foils could be made to transform *in- situ* to the austenite phase by using TEM heating stage, yielding microstructures as shown in Figure 3-19. A small number of precipitates with sizes under 20 nanometers were visible, mainly at austenite grain boundaries. These precipitates were

[14] This annealing temperature is well below the solutionizing temperature for excess nickel.

too small to adequately index with SAED diffraction methods, but were assumed to be $Ti_2(Ni+Pd)$[15] particles.

The transformation temperatures of the post-annealed specimen were approximately 50°C higher than in the as-deposited condition, which according to Figure 3-1 corresponds to a minimum of 30 at. % Pd[16]. The composition of the calibration specimen was therefore estimated to be approximately 50.2 at. % Ti, 30 at. % Pd, and 19.8 at. % Ni.

3.7 TEM Microscopy

3.7.1 TEM Sample Preparation

The TEM foil preparation was began by adhering a 3mm molybdenum support ring that had a 1 mm hole to the thin films using M-Bond 610 adhesive. This epoxy resin was post cured at 175° C for 12 hours. After curing the resin, excess thin film was cut away using scissors, which was done very carefully so cutting process would not damaged the adhered film and bend the support ring causing unwanted dislocations and bend fringes in observed TEM photomicrographs. These 3 mm disks were then electropolished on a Struers Tenupol-3 twin jet electroplisher using 25% concentrated Sulfuric acid in Methanol. The best foils that were observed used a current density of 0.7 A/cm^2, 8V, an electrolyte temperature of –20 °C, and flow rate setting of 3. The foils were rinsed in water for 1 min and then rinsed in methanol.

---

[15] This assumption was based on their size, shape, and observed location.
[16] The observed martensite start temperature was 223°C, which about 30 at.% Pd in Figure 3-2.

3.7.2 TEM Microscope Setup

The TEM samples were observed a using double-tilt holder, and TEM was aligned using #2 condenser aperture and a spot size of 5 μm. The objective and condenser astigmatism was corrected as needed during TEM observation. The #5 SAD aperture was inserted at in the thin area to observe the crystallinity and phase of the material, and diffractions patterns were taken at different camera lengths and an exposure time of 15 seconds. The #6 objective aperture was inserted and centered on the transmitted beam to form bright field images at various magnifications.

To image *in-situ* phase transformation and the austenitic structure of TiNiPd, a double tilt stage equipped with electro-resistive furnace was employed. The temperature of this furnace and TEM foil was measured by Pt-PtRh thermocouple, whose output was displayed on an mV meter and was converted to temperature in Celsius using the manufacturer's calibration curve. The furnace was outgassed for 2-hours at 600°C to remove contamination and absorbed gases before use. During *in-situ* transformation observation, the furnace was ramped slowly from room temperature to 300°C at rate 10°/min. After the furnace temperature reached 300°C, the foil was allowed to equilibrate and fully transform to austenite before taking photomicrographs.

3.8 Thin Film Thickness Measurements

The thickness of the as-deposited films was used to calculate the deposition rate of the sputtering process. To obtain the thickness profile, a Dektak II profilometer was used to scan 1 mm wide. 5-10 thickness measurements were made for each sample and averaged.

CHAPTER 4 RESULTS AND DISCUSSION

The sputter deposition of alloys is complex and complicated by the large number of physical and chemical processes involved. Previous discussions on the mechanisms of sputtering as well some process parameter effects on film composition was presented in Chapter 2.

The first part of this chapter will present data gathered from compositional studies of sputtered TiNi and TiNiPd films. This includes a discussion on magnetron sputtered TiNi film composition as compared to the triode results, and in addition experimental data on composition and the transformation temperatures of TiNiPd films will be presented.

The second part of chapter will discuss the mechanisms possibly responsible for the film composition shifts, which include the following: partial yields, angular distributions of the sputter particles, thermalization, mechanisms that effect composition of the growing film such as sticking coefficients and resputtering, and surface diffusion in the target.

Definitive conclusion will not be made on the actual mechanisms that affect the film compositions, however, experimental results will show that film compositions do vary with the deposition process making composition control problematic. Suggestions for further experiments will be made in Chapter 5 that may lead to a better understanding of these mechanisms and a solution to composition control problem.

4.1 Sputtered Binary TiNi Composition Experiments

Films were sputtered in a 28" Kurt J. Lesker (KJL) Supersystem-II apparatus equipped with a KJL Torus 3-M magnetron sputter source, which was fitted with binary 3" diameter, 1/4" thick $Ti_{49}Ni_{51}$ target. Eight thin films approximately 12.3μm thick were sputtered sequentially onto flint glass slide substrates. Each film was sputtered for 3 hours at ambient chamber temperature using a sputtering power of 250 watts, an initial base pressure better than $5x10^{-7}$ Torr, an argon working gas pressure of 4.5 mTorr, and a substrate-target distance of 78mm. Figure 4-1 shows the ZAF corrected film composition measured at the center of the each film as a function of elapsed time on the binary TiNi cathode at the end of each deposition. The results show that the film composition changes continuously with time, beginning in the Ti-enriched range (relative to the sputter cathode composition), and ending in a Ni-enrichment of the film with an overall change in Ni composition around 2 %. The film composition matches that of the sputter cathode material only for a brief period after 12 hours of sputtering at 250 watts. A quasi steady-state condition is apparently approached at 14 hours of sputtering at a composition that is Ni-rich relative to the target composition.

Figure 4-2 shows a surface plot of both the lateral and the temporal variation in film composition. The latter variation is measured as a function of the radial distance away from the projection of the diode cathode center. If the scatter in composition data with lateral distance was assumed to be related to random errors and poor counting statistics, the surface can be smoothed to give the surface plot shown in Figure 4-3. The variation in the Ni content with lateral distance seems to diminish as the sputtering time increases. This is also apparent in the 2-D plots shown in Figures 4-4 and 4-5. The linear

fit through all the data points in Figure 4-5 would indicate that the Ni content does not change significantly with lateral distance from the cathode center at long sputter times. However at initial sputtering of the target, variation in the composition is evident, where a Ti-enrichment is apparent toward the edge of the specimen and above the weartrack of the target. This data may be compared with results of a similar experiment using a triode-type sputter gun, which is discussed below.

Nine 6 μm thick thin films were deposited from Simard 383 triode source using a binary 2-1/4" diameter, 3/8" thick $Ti_{49}Ni_{51}$ target at power of 440 watts[1] with a thermionic filament current of 30A, an argon working gas pressure of 2.8mTorr, and working distance of 131 mm. These films were used to observe the composition change verses sputtering time behavior of the triode source, which is shown in Figure 4-6. Although even greater overall Ti-depletion is apparent, it can be seen that the output of the triode source is nominally constant with time, showing approximately 0.25% shift from beginning to end of the run, which is an order of magnitude better than the performance of the diode source. Figure 4-7 additionally shows slightly worse lateral in-plane composition uniformity for the triode output as compared to the diode performance. This Ni-content of the films was found to increase by about 0.75 at % at distances of 20 mm for the cathode center.

[1] 440 watts sputtering corresponded to a sputtering voltage of 550Vand a current of 0.8A.

4.2 Studies of Films Sputtered from P/M Composite TiNiPd Target

4.2.1 Composition Studies of Sputtered TiNiPd Thin Films

Table 4-1 gives a master list of the films fabricated, together with their characteristics and some of their deposition parameters (their depositions parameters are shown in detail in Table 3-2). Targets used in this study were made with 53.5 at. % Ti, or 3.5 at. % in excess of equiatomic stoichiometry. The results show that the titanium content of as-deposited films ranged from 49.4 at% to 52.9 at%. The Ti depletion during sputtering was not as high as was anticipated. The mean Ti content of 25 films was 51.4 at%, for an average overall Ti-loss during sputtering of 2.1%. The standard deviation in the measurements of the Ti-content for the same 25 films was 1.2 at%. The scatter[2] in the EDS data was minimal as compared to overall variation in Ti-content, which is indicative of substantial process parameter and target erosion effects on film composition, as will be discussed further below.

4.2.2.1 The Effect of Target Erosion on Composition in TiNiPd Thin Films

Figure 4-8 shows composition of films made from target PD1 as a function of the time for a cathode that has been sputtered at 250 watts. In this case, the titanium 'output' is initially depressed by over 4% relative to the nominal 53.5 at% in the as-fabricated cathode, but rises over the first 5 hours of cathode wear, finally stabilizing at near 50 at%. The trend toward overall Ti-depletion in the sputtered films is therefore similar to that for both diode and triode sputtering from the binary melt-solidified target, but the trend toward increased Ti output over time is the opposite case observed for the binary material

2 The standard deviation in the composition measurement of single specimen ranged between 0.25 and 0.5 at. %.

sputtered in a similar diode gun. Palladium content of the films is enriched with respect to the 25 at% cathode composition, and the output of this species also rises over the first 8 hours of cathode life. The nickel output is also initially enriched, but over time drops to nearly the initial as-fabricated cathode composition. This is also different from the trend observed in the binary alloy experiments using the diode source. Thus, both Ni and Pd were initially enriched in the films at the expense of Ti. The latter species steadily increased whereas the Ni level dropped during the first 8-10 hours of sputtering. For all three species, and apparent steady-state output condition was reached, but not before the cathode was approximately half consumed.

Table 4-1. TiNiPd Film Deposition Parameters and Properties

Specimen	Target Pd (at. %)	Composition (at. %)			Deposition Temp. C°	Gas Pressure (mTorr)	Substrate Distance (mm)	Thickness	Cloudiness	Adhesion	Ductility	SME	M_s (C°)	M_f (C°)	A_s (C°)	A_f (C°)	M_{s2} (C°)	M_{f2} (C°)	A_{s2} (C°)	A_{f2} (C°)
		Ti	Ni	Pd																
#02240001	25	49.1	21.2	29.7	165	2.5	75	2.3	no	F	P	-	-	-	-	-	-	-	-	-
#02250001	25	49.4	20.8	29.8	615	2.5	75	5.46	yes	F/P	F/P	G/F	172	155	179	189	155	97	117	168
#03010001	25	49.6	20.4	30	556	2.5	75	5.24	yes	F	G	G	171	160	187	197	157	140	143	156
#03020001	25	50.1	19.9	30	530	2.5	75	5.18	no	F	G	G	170	162	178	188	156	132	155	171

Table 4-1 (cont'd).

Specimen	Target Pd (at. %)	Composition (at. %)			Deposition Temp. C°	Gas Pressure (mTorr)	Substrate Distance (mm)	Thickness μm	Cloudiness	Adhesion	Ductility	SME	M_s (C°)	M_f (C°)	A_s (C°)	A_f (C°)	M_{s2} (C°)	M_{f2} (C°)	A_{s2} (C°)	A_{f2} (C°)
		Ti	Ni	Pd																
#03020001-AN-0518-500	25	50.1	19.9	30	530	2.5	67	5.18	no	-	G	G	-	-	-	-	-	-	-	-
#03030001	25	49.9	20	30.1	531	2.5	75	5.23	no	F	G	G	167	153	170	185	153	147	160	170
#03090001	27	51.4	18	30.6	174	2.5	75	3.58	no	G	-	-	-	-	-	-	-	-	-	-
#03100001	27	51.2	18.1	30.7	605	2.5	75	4.35	yes	G/F	P	P	174	167	162	189	167	110	123	162

Table 4-1 (cont'd).

Specimen	Target Pd (at. %)	Composition (at. %)			Deposition Temp. C°	Gas Pressure (mTorr)	Substrate Distance (mm)	Thickness μm	Cloudiness	Adhesion	Ductility	SME	M_s (C°)	M_f (C°)	A_s (C°)	A_f (C°)	M_{s2} (C°)	M_{f2} (C°)	A_{s2} (C°)	A_{f2} (C°)
		Ti	Ni	Pd																
#03190001	27	49.7	18.5	31.8	565	2.5	75	4.3	yes	P	P	P	-	-	-	-	-	-	-	-
#03220001	27	51	18.5	30.5	549	2.6	75	5.78	yes	G/F	P	F	145	117	113	159	-	-	-	-
#04250001	27	50.4	18.4	31.2	509	2.5	67	8.12	frosty	G	P	none	113	84	102	128	-	-	-	-
#05160001	27	50.3	18.1	31.7	480	2.5	67	6.97	no	G	P	-	-	-	-	-	-	-	-	-

Table 4-1 (cont'd).

Specimen	Target Pd (at. %)	Composition (at. %)			Deposition Temp. C°	Gas Pressure (mTorr)	Substrate Distance (mm)	Thickness µm	Cloudiness	Adhesion	Ductility	SME	M_s (C°)	M_f (C°)	A_s (C°)	A_f (C°)	M_{s2} (C°)	M_{f2} (C°)	A_{s2} (C°)	A_{f2} (C°)
		Ti	Ni	Pd																
#05160001 -AN-0605-750	27	50.3	18	31.7	480	4	67	6.97	no	-	G	-	-	-	-	-	-	-	-	-
#05290001	27	52.4	18.4	29.2	601	4.1	67	3.55	yes	F	P	F	147	119	167	175	-	-	137	167
#05290002	27	52.3	19	28.7	574	4.1	67	3.67	yes	G	P	P	143	112	155	177	112	108	-	-
#05290003	27	52.6	18.4	29	518	4	67	3.45	no	G	F	-	-	-	-	-	-	-	-	-

Table 4-1 (cont'd).

Specimen	Target Pd (at. %)	Composition (at. %)			Deposition Temp. C°	Gas Pressure (mTorr)	Substrate Distance (mm)	Thickness µm	Cloudiness	Adhesion	Ductility	SME	M_s (C°)	M_f (C°)	A_s (C°)	A_f (C°)	M_{s2} (C°)	M_{f2} (C°)	A_{s2} (C°)	A_{f2} (C°)
		Ti	Ni	Pd																
#05290004	27	52.9	18.5	28.6	548	4	67	3.53	no	G	F	-	-	-	-	-	-	-	-	-
#05290004 -AN-0605-750	27	52.9	18.5	28.6	548	4	67	3.53	hazy/ frosty	P	-	-	-	-	-	-	-	-	-	-
#05290003 -AN-0624-750	27	52.6	18.4	29	518	4	67	3.45	no	G	P	-	-	-	-	-	-	-	-	-
#05290003 -AN-0625-650	27	52.6	18.4	29	518	4	67	3.45	hazy	G	-	-	228	212	227	244	212	198	219	227

4.2.2.2 The Effect of Deposition Temperature on Composition

Figure 4-9 shows titanium content for as-deposited (not annealed) films as a function of deposition temperature. Although hot-substrate depositions showed slightly elevated Ti levels as compared to the few runs conducted at ambient temperature conditions (solid trendline in Figure 4-9), the trend for elevated-temperature deposition shows that Ti to decreases slightly with increasing substrate temperature (dashed trendline). The effects of deposition temperature on the atomic fraction of all elemental species from Ti 53.5%/ Ni 19.5 %/ Pd 25% Target is shown in Figure 4-10. Overall trends in composition (solid trendline) show that Ti and Pd content increase with temperature, while the Ni content decreases. If the low temperature result is excluded, the trend is the opposite; Ni content increases with temperature while Ti and Pd decrease (dashed trendline). The latter trend is probably more valid, since composition measurement of the low temperature non-crystalline films may be in error[3].

4.2.2.3 The Effect of Working Gas Pressure on Composition

Deposition pressure exerted a more pronounced effect on composition, as shown in Figure 4-11, which plots the effect of the P•D (pressure x working distance) product on thin film composition. Figure 4-12 is a plot of composition verse working pressure alone. In Figure 4-12, it can be seen that as pressure was increased, the titanium and nickel levels increased while the palladium concentration dropped by a complementary amount. This suggests that the primary effect of increasing pressure is to diminish to the concentration of the heavier species in the deposition flux.

---

[3] Slight errors in composition can result was analyzing amphorous materials with crystalline standards in ZAF correction, since electron scattering and channeling are different between amorphous and crystalline materials.

4.2.2 Transformation Temperatures of Sputtered TiNiPd Thin Films

Transformation temperatures were determined for selected films by differential scanning calorimetry (DSC) and by electrical resistivity measurements. Results for as-deposited films are shown in Tables 4-2 and 4-3 (For DSC and Resistivity results respectively), and in Figure 4-13. A number of depositions could not be evaluated by DSC since the high degree of adhesion achieved and the lack of material that could be removed from the silicon substrate (about 10 mg was needed for each test).

Table 4-2. Transformation Temperature Data for TiNiPd films from DSC Curves.

Sample #	M_{s1} (°C)	M_{f1} (°C)	A_{s1} (°C)	A_{f1} (°C)	M_{s2} (°C)	M_{f2} (°C)	A_{s2} (°C)	A_{f2} (°C)	M_{s3} (°C)	M_{f3} (°C)	M* (°C)	A* (°C)
02250001	165	154	172	190	147	115	145	169	-	-	161	184
03010001	173	161	176	192	161	151	145	167	124	112	158	188
03020001	137	125	149	161	123	93	101	148	-	-	110	133
03220001	149	125	102	144	125	90	-	-	-	-	106	126
05290001	144	100	118	166	-	-	-	-	-	-	117	142

Table 4-3. Transformation Temperature Data from Electrical Resistivity Curves.

Sample #	M_{s1} (°C)	M_{f1} (°C)	A_{s1} (°C)	A_{f1} (°C)	M_{s2} (°C)	M_{f2} (°C)	A_{s2} (°C)	A_{f2} (°C)
02250001	172	155	179	189	155	97	117	168
03010001	171	161	187	197	157	140	143	156
03020001	170	162	178	188	156	132	155	171
03030001	167	153	170	185	153	147	160	170
03100001	174	167	162	189	167	110	123	162
03220001	145	117	113	159	n/a	n/a	n/a	n/a
04250001	113	84	102	128	n/a	n/a	n/a	n/a
05290001	147	119	167	175	n/a	n/a	137	167
05290002	143	112	155	177	112	108	n/a	n/a

The DSC and resistivity curves generally exhibited two and sometimes three transformation peaks, which indicates that sequential transformations occurred on both heating and cooling. Sequential transformations involving orthorhombic martensite can be eliminated as a cause for this behavior, as well as any Monoclinic or R-phase

transformations, which are known to be fully suppressed by Pd substitution [Lindquist, 1988]. One possible cause for the multiple transformation peaks is through-thickness structure gradients (such as finer grain size near the film-substrate interface) allowing lamellar transformation zones to develop in association with differentiated near-surface and near-substrate microstructures or stress-states. Another possibility, which is indicated by composition study data, is that composition varies with thickness, and thus different phases can form through the thickness, such as precipitates. As discussed earlier in Chapter 2, precipitates can have an adverse effect by suppressing the martensite transformation, and differing densities of precipitates in the film would explain the existence of multiple transformations at different temperatures. However, at present the reasons for the multiple peaks remain unclear.

Transformation temperature data for as-deposited films plotted as a function of palladium content are shown in Figure 4-13, and for reference, are superimposed on the literature data by Lindquist in Figure 4-14. The observed as-deposited transformation temperatures fell within the range predicted by previous work but are generally on the low side, which probably reflects the fine grain size of the films in comparison to ingot-metallurgy alloys used in most of the studies in the literature. The annealed thin films transformation temperature coincided with the literature, which indicates that the palladium content measured by EDS is close to the true value. However, it is unclear how off-stoichiometric compositions and precipitate formation affects the transformation temperature, thus further heat-treatment and TEM studies are necessary.

The M_s temperature was observed to increase by approximately 11 degrees per at% increase in Pd content, which is close to the 13 degree per at% slope from Wayman's

1990 study (see Fig. 3-2). The [A_f-M_f] hysteresis varies widely, from as high as 65 °C to as little as 22 °C, with low values of hysteresis tending to occur for high transformation temperatures. The M_s temperature also was noted to vary sharply with Ti-content in the films as shown in Figure 4-15, with the maximum in M_s occurring, as expected, at near-stoichiometric compositions, but dropping by about 12.5 °C per at% Ti. This result is similar to composition relationship between Ti and M_s temperature in binary bulk materials that Wang [1965] observed, which had about 15°C per at. % Ti trend (See Figure 2-4).

The two outliers observed in Figure 4-15 could be related to the sputter deposition temperature. At low deposition temperatures, a mixture amorphorous and fine grain structure can be produced that can depresses the M_s temperature. This could be attributed to the low observed M_s temperature of the outlier that was deposited at 549 °C. In the case of the high M_s temperature outlier, the deposition temperature was 605 °C and observed M_s temperature was higher than the observed trend. This film may have developed a higher degree of lattice ordering that does not sufficiently depress the M_s temperature.

As shown above, deposition temperature can exert a strong effect on transformation temperatures, as shown in Figures 4-16a and 4-16b. In films sputtered form targets Pd1 and Pd2, the transformation temperatures increased with increasing deposition temperature. This may be related to the ultra fine grain size that is possibly being formed at low deposition temperatures and is suppressing the M_s temperature. Larger grains are generally formed at high temperature temperatures that do not depress the M_s temperature, which may account for the higher transformation temperatures.

In summary, the transformation temperatures are strong function composition as well as film microstructure. As expected, the transformation temperature increased with increasing Pd content. The comparisons with literature data show that in general TiNiPd films were close to stoichiometry. It is not clear how off-stoichiometric composition effect composition, but excess Ti seems to decrease the M_s temperature. Some comment is appropriate at this point regarding the sputtering mechanisms that are possibly affecting film composition. This mechanism will be discussed in detail below.

4.3 Mechanisms that Affect Film Composition

There are several aspects of the alloy deposition process that have a significant effect on the film composition: partial sputtering yields, angular distributions of sputter particles, mechanisms that affect composition at the film surface such as sticking coefficients and resputtering, and surface diffusion in the target. These mechanisms will be discussed in terms of experimentally observed composition trends in proceeding paragraphs.

4.3.1 Partial Sputtering Yields

Sputtering is mechanism of ballistic ejection of atoms from the cathode in which the accelerated ion first penetrates the target surface, and then undergoes a series of atomic collisions (known as a collisional cascade) which eventually transfer sufficient momentum to near-surface atoms to cause ejection. The likelihood of the ejection event is primarily dependent on the surface binding energy of the cathode species, but also

depends on its mass and the mass of the projectile. Hence, the probability of ejection (sputter yield in atoms per incident ion) is species dependent.

Pure Ti has a lower sputter than Ni because its surface binding energy is higher and its atomic number density is lower. Furthermore, energetic ions bombarding pure Ti targets will penetrate and transfer most of their energy at greater depths than in Ni, therefore making it less probable that recoils will have enough energy to over come the surface binding energy resulting in a lower yield. If pure material sputter yield data are assumed, Ni would be expected to be preferentially sputtered from the TiNi target since Ni has more than twice[4] the sputter yield of Ti as calculated using the Matsunami formulation (see Table 2-4). This would cause the film to enrich in Ni at earlier stages of sputtering, which is contrary to the observed Ti rich composition at 3hrs in Figure 4-1. Thus, we must consider sputtering in TiNi alloy.

In TiNi alloys, the surface binding energies, atomic number densities, and projectile depths should be the same for Ti and Ni atoms, since their bond structures are similar. In this case, Ti has as lighter mass that is closer to the projectile mass (Ar) than Ni, thus, more projectile energy is transferred to Ti atoms than Ni, and Ti recoils are more likely to be ejected from the surface. It is possible that Ti rather than Ni would have the higher sputter yield, which may be amplified and exhibit a higher sputtering yield than the pure material. This could account for the Ti-rich composition at 3 hrs in Figure 4-1, but contradicts the observed Ni rich composition in the triode films. However, it should be noted that the film composition in triode could be affected by resputtering which in fact favors the idea of preferentially sputtered Ti. This will be discussed in more detail later. The key factor in increased partial yields is the mass

[4] Ni had a sputter yield of 0.66 at 300 eV, and Ti had 0.3 sputtering yield.

relationship between the projectile and sputter species, thus partial yields of Ni and Ti can change with projectile type, which is discussed below.

If the above theory for preferential sputtering is true, Ni would preferential sputtered when Krypton is used as sputtering gas, which is closer in mass to Ni. This implies that amount and type of preferentially sputter species is a function of difference between recoil and projectile mass. A calculation can be made of relative yield in which U_{sb} and Z_r has been held constant, and by only varying the recoil mass in the terms from Matsunami's empirical sputter yield formula (Equation 2-3) that are not associated with the energy loss cross section. This analysis gives the result shown in Figure 4-18 for Argon projectiles. The magnified portion of the curve given in the inset shows the isolated mass effect (as it impacts the values of E_{th} and α^* in Equation 2-3) and indicates that, other factors being equal, Ti (mass 47.88) should sputter faster than Ni (mass 58.7) by a factor of approximately 1.3%. Heavier species should sputter at even lower rates, and in case of TiNiPd ternary alloy, Pd should not be enriched since it has highest mass of the constituents, which is not observed. However, the assumption for equal binding energies for ternary compositions is less obvious than the in the case for the NiTi binary compound, and the above model may be less valid. Some comment is appropriate at this point regarding the performance of composite targets (made up of incompletely reacted elemental powders by hot-pressing).

During the 'burn-in' period, composition can be expected to shift sharply as the effective cathode surface composition shifts to account for the different sputter-yields of the components. It is not known at present exactly how long this burn-in period should be expected to last, but the triode experiment indicates that it is not longer than two

hours. Also, to a first approximation the alloy and P/M composite targets should reach steady state by similar mechanisms, but may have a sufficiently longer burn in time as apparent in Figure 4-8 in which it apparently takes 5 hours before steady state is reached. The surface of the target is initially depleted in the more rapidly sputtered species, whose effective sputtering rate then drops as fewer atoms (or particles) of that type are left exposed at the surface. Eventually, a surface "alter-layer" develops that equilibrates the partial sputter yield between species, which schematically shown in Figure 2-40. Barring continuous resupply of this element to the surface by bulk diffusion, steady state (if attained) must correspond to a condition where the sputter flux precisely matches the composition of the cathode. In the case of the P/M target, surface composition is determined by the relative distribution of the powder particle types at the surface, but the steady state argument applies once a depth of a few particle diameters has been eroded. In fact, diffusion conditions for the achievement of steady state are somewhat less stringent for P/M materials, and bulk diffusion is not likely to be a significant factor in a target composed of pure materials, since no continuous concentration gradients exist. However, the development of local sputter topography, such as etch pits, in the case of powder targets may be at least, in part, responsible for the changes over the cathode life since erosion of the rapidly sputtering species will tend to cause it to become occluded by slower-sputtering particles in a way that encourages redeposition onto other particles in the aggregate, as indicated schematically in Figure 4-19. This would not affect the steady-state argument to the first approximation but could alter the cosine-distribution of the flux, which tends to narrow the distribution of the more rapidly sputtering element relative to the other species in the cathode. From the target wear results it seems this

surface morphology takes at least 5 hours to develop. After its development, there seems to be a steady state film composition with target wear, but it is different from target.

As alluded to above, even if the flux at the cathode surface matches the bulk composition, the angular distribution (under- or over-cosine) of the ejected atoms will still be capable of altering the flux composition, and thus the film composition, at any distance away from the cathode surface. Little is presently known about factors affecting these angular distributions, but atomic mass is expected to play a role in determining the over- or under-cosine nature for a given species in an alloy. At this point, a discussion on composition effects of differential angular distributions is appropriate.

4.3.2 Composition Effects Resulting from Differential Angular Distributions

Difference in angular distribution of sputter particles can affect composition by enriching the substrate in one species relative to the other at positions defined by a preferred angle of ejection. In the case of P/M targets, the angular distributions of sputter particles should be similar to pure elements. Wehner *et al.* found Ni to exhibit an under-cosine distributions, however, there are no results in the literature regarding the type of distribution Ti and Pd exhibit. Thus, it is difficult to explain the possible effects that the angular distributions might have on the P/M film composition. However, the above model for P/M target erosion would suggest that Pd (the fast-sputter species) has forward bias distribution and may account for observed enrichment in the film.

In the case melt-solidified alloys, the angular distributions should be different than pure materials. According to Olson's reflective collisional model of mass effects on angular distribution, the lighter species (Ti) would have preferential emission normal to

the target surface and would enrich at the substrate positions above the cathode center. As a result, Ni should enrich at lateral distances away for the wear track. In the case of magnetron sputter targets that develop a wsertrack, Ti should be enriched directly above the wear track, while Ni would be enriched at location above the cathode center. This is consistent with the results shown in Figure 4-4 at early hours of sputtering. In the case of triode composition a result, a slight enrichment (relative to lateral positions) of Ti at center of the film is noted (see Figure 4-7) which is consistent with favored normal ejection angles for Ti.

If this is true, the above analysis would predict a continual enrichment of titanium in the central region of the growing film, and thus it is of little help in explaining the observed composition shifts. It may, however, bear on this issue of composition shifts over the life of the cathode in diode sputtering, where cathode depletion is accompanied by the formation of a pronounced surface 'wear-track' topography. The evolution of the wear track alters the orientation of the local surface normal with respect to the substrate plane. If one species is sharply overcosine with respect to another, this change in orientation may cause composition to change as the wear track develops. Experimentally, this possibility is strongly supported by data (shown in Figure 4-1 and 4-6) showing that composition shifts quite markedly in the case of the diode sputter gun, but shifts hardly at all when a triode sputter source is used, which has a very even, flat cathode erosion profile. However, this model is very inconclusive, since there is no literature data or theoretical models that support this phenomenon. In addition, the differential angular distribution does not support the observed Ti-loss in triode film.

However, thermalization could offer a possible mechanism which might explain the Ti depletion in the films.

4.3.3 Thermalization

Sputtered cathode species and reflected neutral working gas atoms may suffer collisions with gas atoms during transport to the substrate. Such collisions reduces energy of both the sputter flux, which leaves the cathode surface with as much as 10 eV (equivalent to a temperature of ~100,000 Kelvins), and the reflected neutral atoms that has an energy an order of magnitude higher than sputter atoms. Thermalization has two key implications: First, thermalization of the cathode alloy species disperses the flux in a way that is mass (and therefore species) dependent, and secondly, thermalization reduces the energy of the reflected neutrals and diminishes any effects due to resputtering of the growing film. The former mechanism may account for titanium loss in the films, as discussed later.

The fraction of sputter particles that reach the substrate is related to thermalization distance, the mass of sputtered atom, the mass of the sputtering gas atoms, and the energy of the ejected the sputter particle. Turner et al. calculated the fraction of sputtered atoms which reach the substrate after suffering scattering events during transport. He considered both the mass of the species and its binding energy, which was introduced to account for the initial energy of the sputtered species in the sense that higher binding energy would imply higher initial energy. As in the Hoffman study, Turner did not explicitly simulate deposition rates for Ni or Ti, but did produce results for Na, Sn, C, Cd, Pd, Nb, Pb, Au and W. These results are shown in Figure 2-47, on which we have

superimposed a set of estimated contour lines giving the percent of atoms that actually reach the substrate, as a function of binding energy (y-axis) and mass (x-axis). It is apparent from this data that thermalization should not affect the composition in the case of TiNi films since both Ti and Ni fall on the same contour near 82.5%.

The initial energy of most of the ejected recoils is approximately half its surface binding energy [Behrisch, 1981; Thompson, 1981]. In the case of ejected recoils of Ti and Ni from pure element targets, the recoils would have higher initial energy for Ti since it has a higher surface binding energy. However, since the mean path and thermalization distance is lower for Ti (see Table 2-6 and 2-7), it will transfer more of its energy or thermalize at shorter distances than Ni. In addition, the less massive Ti atoms are scattered more diffusely than the heavier mass Ni atoms. A combination of higher initial energies, lower thermalization distance, and higher scattering probability of Ti could result in its reduction in the incident flux as compared to Ni, as seen in Figure 2- 46 where Ni and Ti lie on the same contour line. The key difference between pure materials of Ni and Ti and the binary alloy is that surface binding energies and initial energies of the recoils can be assumed to be the same in the TiNi alloy. If these assumptions were true, Ti would have a lower incident flux than Ni, because it is less massive and has shorter thermalization distances. This would create a continual flux to the substrate that is Ni rich. Even though, this theory is probable, it cannot be concluded as the dominating effect for Ti-depletion since other mechanisms can affect composition at substrate such as sticking coefficients and preferential resputtering, which are discussed in the below.

4.3.4 Mechanisms that Affect the Composition at the Film Surface

4.3.4.1 Sticking Coefficients

The sticking coefficient is probability that an incident atom is adsorbed by the substrate. If the sticking coefficients are less than 1, only a fraction of the incident flux will condense on the surface. Thus, if there are differences in the sticking coefficients between two sputtered species, the growing film will be lean in the species with lower sticking coefficient. The sticking coefficients are thought to be close to unity for metals with high melting points [Mahan, 1999]. However, small differences between the sticking coefficients of Ti and Ni could account for the observed Ti-loss during sputtering. If a difference in sticking coefficient does exists, it would most likely be lower for Ni since Ti is more reactive and thus is easier to be chemically absorbed by the substrate. Furthermore, the energy of the sputtered particles promotes rapid surface diffusion, allowing them to find traps more quickly and thus be less likely to desorb. Unfortunately, there is no data on the sticking coefficients for Ni and Ti that can conclusively eliminate it as the cause for observed Ti depletion.

Additional mechanisms need to be considered with respect to events occurring at the surface of the growing film. Resputtering has been mentioned above, and can alter the composition of the growing film via any mechanism in which the probability of resputtering for one species is greater than another.

4.3.4.2 Preferential Resputtering

Ion projectiles (i.e., Ar) may be elastically backscattered from the cathode and can then (having been neutralized) travel with high energy in the direction of the substrate.

Thus, the growing film is also subject to projectile bombardment that causes a portion of the film to be 'resputtered'. Here, the species dependence of the sputter yield becomes important in determining film composition.

Preferential sputtering of alloys can cause a film to have different composition than the deposition fluxes and occurs from differences in surface binding energy and non-proportional kinetic energy transfer between the constituents due to differences in kinematical factors. Preferential sputtering of the target only exists at the early stages of sputtering, and eventually due to conservation of mass, the target and deposition flux composition will equilibrate. This steady state condition does not occur in the resputtering of films, since material is continually being deposited, and the surface is continually being depleted in the preferentially sputtered material. Thus, the film composition will be lean in the preferentially resputtered species with respects to deposition flux. The differences in resputtering rates for Ti and Ni are discussed in the following paragraphs.

Hoffman's data on intrinsic resputtering shown in Figure 2-50, predicts that the resputtering percentages of Ni and Ti are similar and would not account for preferential loss of Ti. Further, if a difference between resputtering rates were derived from Hoffman's data, Ni would be found to be preferentially lost rather than Ti, since it has a slightly higher atomic mass parameter. However, Hoffman used data gathered from the resputtering of pure materials, thus his results may not reflect the resputtering rates that occur for the same species in alloys. As mentioned above, it is possible that there are sputtering mechanisms in TiNi, which could result in higher Ti sputtering rates than Ni

(using Argon). Thus Ti rather than Ni would be preferentially resputtered, which is plausible explanation for the Ti depletion observed in the Triode films.

If the sputtering yields of Ni and Ti in the binary alloy were assumed to be similar and do not cause the Ti-depletion in the films, there could be another mechanism to explain the preferential loss of Ti. For instance, if Ni diffuses into the bulk and creates a Ti rich surface composition, more Ti than Ni will be lost due to resputtering, resulting in a overall film composition depleted in Ti. The diffusion of Ni from the surface, rather than Ti, assumes that Ni is the more rapidly diffusing species, but there must be a driving force for diffusion. Normal fickian diffusion as a result of concentration gradients is not an obvious mechanism for the Ni diffusion, since we assume that Ni increases in concentration away for the surface. However, Ni could diffuse by the Soret effect, which is diffusion down an activity gradient which arises from the presence of a temperature gradients. There certainly are very steep temperature gradients in the first few monolayers that could be as high as several hundred degrees Kelvin per micrometer due to the heat generated by ion bombardment [Bunshah, 1994]. These temperature gradients could lead to large activity gradients, and Ni, being a rapid diffuser, could diffuse in the bulk film via the Soret Effect and thus protect itself to the same degree from resputtering.

An experiment was conducted by Ellesworth [2000] to calculate the Soret coefficients for Ti and Ni. The composition of TiNi alloy was not observed in this experiment to change in the direction of the temperature gradient, and it was concluded that the temperature gradients did not create a sufficient activity gradient for Soret effect diffusion to occur.

Despite this negative result, the possibility still exists that the surface free energy of Ti is lower than that of Ni, which would lead to the same consequence. For the pure elements, the surface energy of Ti is indeed lower than that of Ni (γ_{Ti} = 1.69 J/m^2 whereas γ_{Ni} = 1.81 J/m^2). If this difference holds for binding in the intermetallic compound, then Ti might again find itself preferentially exposed to resputtering events. In this context it should be remembered that for this mechanism, as well as for the other phenomena discussed here, only a small difference in diffusion properties between Ni and Ti is necessary to account for the observed composition shifts. It is the exquisite sensitivity of the shape- memory effect to composition that makes the understanding of these subtle phenomena important from a manufacturing standpoint.

None of the above mechanisms can account for the composition trend seen in Figure 4-1. Preferential resputtering, thermalization, and differences in sticking coefficients can only shift this composition trend to higher or lower relative composition and cannot account for the observed time-evolution. Thus, a different mechanism must be responsible for the trend such as target surface diffusion, which is discussed below.

4.3.5 The Effects of Target Surface Diffusion on Film Composition

In the case of alloys with different sputter yields, a surface altered-layer forms at steady state that is depleted in the fast sputtering species. The erosion and formation of new altered-surface layers are self-perpetuating such that after its initial formation, a steady-state condition exists with continued target erosion. Assuming above arguments on preferential sputtering, Ti will be the fast sputtering species and thus depleted in the alter-layer. This surface altered layer creates a large composition gradient in the direction

normal to the target surface which will drive a diffusive flux of the rapid-sputtering species from the bulk to the surface. However, if the cathode is well-cooled, and the target erosion rate is high enough, bulk diffusion will not have sufficient time to influence the surface composition significantly before it is simply eroded away. A steady-state condition is theoretically attained in which the sputtered flux must match the bulk composition of the cathode. In the case of the diode magnetron, however, a second complication arises. As a result of the inhomogeneous magnetic field strength that gives rise to the racetrack profile, the overall sputtering rate will be at a maximum at the center of the racetrack. Since the erosion rate is highest at this point, depletion of the rapid-sputtering species will occur here first, leading to the formation of a surface composition gradient. This gradient will occur in a region of the cathode that is probably quite hot, that is also under continual ion bombardment, so the surface diffusion rates can be expected to be quite high. This could lead to a continual supply of the rapidly-sputtering species from the edges of the wear track to the center of the track. This would, in turn, tend to deplete the cathode at the edges of the wear track in the rapid-sputtering species, under circumstances where steady state is not achieved due to the low erosion rate. The result would thus be twofold. First, the initial enrichment in the rapid-sputtering species would be larger, and the time required to achieve steady-state conditions would be longer than would be otherwise expected. Secondly, the surface-diffusion mechanism would result in a steady rise in output of the slow-sputtered species as the cathode becomes steadily less and less able to supply the high-rate species from the edge to the center of the wear track. This surface diffusion process is schematically shown in Figure 4-17.

It should be noted that for the case of sputtering from the triode source, where the racetrack topography does not form, the relatively even cathode erosion profile would not result in surface composition gradients, and steady state would be achieved vary rapidly under conditions where the bulk cathode was well-cooled. In addition, non steady state conditions due to surface diffusion are not likely to be a significant factor in a P/M target composed of pure materials, since no continuous concentration gradients exist.

In conclusion, this surface diffuse mechanism is a possible cause for the composition shift, but it needs to be verified by quantitative analysis before it can be attributed to the time-evolved composition trend.

CHAPTER 5 CONCLUSIONS

It is apparent from the experimentally observed composition shifts that the deposition process is problematic for producing desired film compositions. Due to the complexity of the sputtering process, it was difficult to determine the principle mechanisms and parameters that determine composition in sputtered TiNi and TiNiPd alloys. Instead a list of possible mechanisms were discussed in terms of the of the observed composition trends, which are outlined below. Further experiments will be presented that may clarify composition problem.

The following composition trends were observed during sputtering of TiNi and TiNiPd:

1. Magnetron sputtered TiNi film compositions showed a continually changing composition with target erosion. The film composition varied from 2 at. % Ti-rich at 3 hours of sputtering to 1.5 at.% Ni enrichment at 24 hours of sputtering, with an overall composition change of 3.5 at. %. There was an enrichment of Ti at lateral positions and especially above the wear track at earlier hours sputtering, which diminishes as sputtering time increases.
2. Triode film compositions were nominally constant with target wear. The film composition showed a consistent 3.5 at. % Ti-loss relative to the target composition, and a slight lateral increase Ni content from the center position.
3. In the case of TiNiPd film compositions, titanium was initially depressed by over 4 at. % relative to the 53.5 at. % cathode composition, but raised over the first 5

hours of cathode wear to finally stabilize at near 50 at. %. Ti content was observed to decrease with increasing substrate temperature and was observed to increase with working gas pressure. Pd content was also observed to decrease with increasing substrate temperature and working gas pressure. Composition and deposition temperatures showed a strong effect on film transformation temperatures.

The following mechanisms may possibly cause the experimentally observed film compositions shifts:

1. The partial sputter yields of Ti in the alloy may exhibit higher yields than pure materials.
2. Formation of surface topography that creates a preferential forward ejection of fast sputtering species.
3. Differences in the angular distributions of the sputter flux between alloy species.
4. Differences in sticking coefficients.
5. Differential reduction in incident sputter flux caused by scattering due to collisions with gas neutrals.
6. Preferential resputtering of the fast sputtering species or by a surface enrichment of the slow diffusing species.
7. Surface diffusion of titanium into the wear track that causes a continually changing sputter flux and film composition with target erosion.

Triode sources give good compositional uniformity over the life of the cathode, however, they create a Ti depletion in the films. It is difficult to determine the dominating mechanisms that cause Ti-loss. It is possible that a combination of preferential resputtering, differences in sticking coefficients, and the reduction in incident flux due to scattering are responsible for the Ti depletion. The observed enrichment of Ni at lateral positions in these films may be related to differential angular distributions, due to a mass effect and energy transfer difference between species that prefers the forward ejection of Ti and enriching it in the films at the center and Ni at lateral distances.

Both the melt-solidified and P/M targets seem to have composition control problems related to formation of surface topography in magnetron sputtering. In the case of melt-solidified targets, it is possible the formation of the wear track, and the new surface altered-layers promotes a continually changing Ti surface diffusion flux into the wear track that may be responsible for non-steady state composition shift with time. P/M targets may have long burn time associated with the formation of a pitted surface morphology before steady state composition flux is reached. Also, this surface morphology may create a preferred ejection of Pd normal to the target that results in an enrichment of Pd in the center of the film.

To gain a more definitive understanding of sputtering process effect on composition further experiments are necessary. The following list suggests some the experiments that could clarify the compositional control problem:

1. The surface diffusion Ti into wartrack may be understood by a quantitative analysis that models mean surface diffusion time as function erosion rate of target and partial sputter yields of Ni and Ti.
2. Further investigations must be conducted on the effects of target wear and racetrack surface evolution on angular distributions of Ti and Ni. One such investigation is the development of computer simulated models that track angular distribution and film composition change as function of surface angle change using integrated sputter yields summed form a collection of points on the target surface. This simulation may also explain the variation of Ni and Ti content with lateral distances, which are not completely understood.
3. There should be further experiments in process techniques that eliminate rather understand composition effects of angular distribution. For example, an investigation of the film compositions created by a substrate that oscillates over the target, which will collect sputter atoms at central and lateral positions of target at all positions of the substrate. In theory, this should result in more uniform film composition.
4. Experiments at high working gas pressures should be investigated since uniform film compositions can be created due to the significant scattering of sputter particles and the elimination of any preferred angular distribution. In addition, the resputtering rate should be significantly reduced at high working gas pressure due thermalization of energetic neutrals. If the Ti-loss is not observed at higher pressures (9 Pa), it may prove that resputtering is a dominating factor in the change film of composition. High pressure also can reduce composition changes

scattering by fully thermalizing both species and randomizing the deposition flux such that there is not a overall difference in incident flux between Ti and Ni. In general, the high working gas pressure may solve the compositions by it has been known to create films with poor mechanical properties

5. If you assume that resputtering causes the Ti depletion in the thin films due to differences in the partial sputter yield between Ti and Ni, then mixtures of Ar and Kr sputtering gas can be used to enhance the sputtering rate of Ni in the alloy. Krypton will transfer more energy to Ni atoms rather than Ti, since it is more similar in mass to Ni. The addition of krypton may increase the Ti content in the films, but it does not solve the problem of the temporal variation in the composition. It may be possible given a certain set of fixed sputtering parameters (such as working gas pressure, substrate-target distance, sputter power, initial target composition) to calibrate the variation of composition with time and the ratio Ar/Kr, such that composition no longer varies with time. This could be done thru a set of experiments that measure composition variation using different Ar/Kr ratios, and then by using a computerized gas controller, the gas ratio is varied precisely with target erosion. This may be a good method for solving the composition problem, but it will give no scientific explanation fro the occurrence of the composition variation with time.
6. Insight could be gained in the preferential sputtering nature of binary alloy by conducting sputter Auger composition measurements. The Auger surface compositions can be measured for unsputtered piece of binary TiNi and compared with surface compositions after a few minutes of sputtering. If differences in

surface composition exist, then it is indicative of preferential sputtering. These experiments may bring clarity to the effects of resputtering and partial yield amplification.

7. Finally, composition studies of cylindrical magnetron sputtered films should be investigated. In cylindrical magnetron sputtering, the substrate lies in the center of a hollow cathode, and substrate receives sputter flux for all angles. This would smear out any effects of differential angular distributions. Furthermore, the sputtering occurs in a closed system, therefore the film must have the composition due conservation of mass. This type of deposition may solve the composition problem entirely.

BIBLOGRAPHY

BIBLIOGRAPHY

Anderson, H. H. and H. L. Bay, "Sputtering Yield Measurements," in Sputtering by Particle Bombardment I, ed. Behrish, Springer-Verlag, Berlin, 1981

Anderson, H. H, in "Symposium on the Physics of Ionized Gases 1980," B. Cobic, ed., Boris Kidric Austria Nuclear Sciences, Belgrad, Yugoslavia (1981)

Behrisch, R., "Introduction and Overview," in Sputtering by Particle Bombardment I, ed. R. Behrish, Springer-Verlag, Berlin, 1981

Berg, S. and I. V. Katargdjiev, "Preferential Sputtering Effect in Thin Film Processing," Journal of Vacuum Science Technology, A17(4), 1999

Betz, G., R. Dobrozemsky and F. P. Viehbock, Bed. Tijdschr. Voc. Tech., 8, 203 (1970)

Binary Alloy Phase Diagrams, Vol. 2, ed. T. B. Massalski, American Metals Society, Metals Park, (1987), 1768

Bunshah, R. F., Handbook of Deposition Technologies for Films and Coatings, Science Technology and Applications, Park Ridge, New Jersey, Noyes Publications, 1994

Busch, T. and E. D. McClanahan, Thin Solid Films, 47:291 (1977)

Chapman, B., "Glow Discharge Processes", John Wiley & Sons, New York (1980)

Chang, L. and D. S. Grummon, Scripta Metall., 25(1991), 2079

Chang, L., Ph.D. Dissertation, Michigan State University, (1992)

Chattopadhyay, G. and H. KleyKamp. Z Metallkd., 74 (1983), 1982

Carter, G., J. C. Colligon and M. J. Nobes, J. Mat. Sci., 6:115 (1971)

Coburn, J. W. and M. Chen, J. Appl. Phys., 51, 3134 (1980)

Coburn, J. W., Thin Solid Films, 64:371 (1979)

Duerig, T. W., K. N. Melton, D. Stockel, and C. M. Wayman. Engineering Aspects of Shape Memory Alloys, Butterworth-Heinemann: London 1990

Eckertova, L., Physics of Thin Films, Plenum Press, New York, 1977

Ellesworth, K., Unpublished Data, Bachelor Thesis, Michigan State University, 2000

Eltoukhy, A. H. and J. E. Greene, J. Appl. Phys., 51:4444 (1980)

Gillam, E., J. Phys. Chem. Solids, 11:55 (1959)

Grace, J. M., D. B. McDonald, M. T. Reiten, J. Olson, R. T. Kampwirth, and K. E. Gray, "Selective Resputtering of Bismuth in Sputtered Bi-Sr-Ca-Cu-O Films", Journal of Applied Physics, Vol. 70 (7), 1 Oct. 1991, pp 3867-75

Green, F. A. and B. N. Chapman, J. Vac. Sci. Technol., 13 (1970), 165

Greene, J. E., B. R. Natarian and F. Sequeda-Osorio, J. Appl. Phys., 49:417 (1978)

Gschneider, K. A. "Physical Properties and Interrelationships of metallic and Semimetallic Elements", Sol. St. Phys. 16, 275, 1964

Harrison, D. E., P. W. Kelly, B. J. Garrison, and N. Winograd, Sur. Sci., 76:311 (1978)

Hodgson, D. E. and J. W. Brown, "Using Nitinol Alloys" Shape Memory Application, Inc., (2000) SMST-2000

Hoffman, D. W., "Intrinsic Resputtering-Theory and Experiment", J. Vac. Sci. Technol., A8(5), 3707, 1990.

Ishida, A., M. Sato and S. Miyazaki, "Mechanical properties of Ti-Ni shape memory thin films formed by sputtering", Mat. Sci. and Eng., A273-275 (1999a), 754-757

Ishida, A. and S. Miyazaki, "Microstructure and Mechanical Properties of Sputter-Deposited Ti-Ni Thin Films", Journal of Engineering Materials and Technology, Jan. 1999, Vol. 121.

Ishida, A., M. sato, A. takei, K. Nomura and S. Miyazaki, Metall. Trans. A, 27A (1996), 3753

Ishida, A., M. Sato, A. Takei and S. Miyazaki, "Shape Memory Behavior of Ti-Ni Annealed at Various Temperatures", Mat. Re. Symp. Proc., Vol. 360 (1995)

Ishida, A., A. takei and S. Miyazaki, Thin Solid Films, 228 (1993), 210

Jardin, P., "Deposition Parameters for Sputter-Deposited Thin Films TiNi", Mat. Res. Soc. Symp. Proc., Vol. 360, 1995, pp. 293-8

Johnson, A.D., V. V. Martynov and R. S. Minners, J. Phys. (France), IV 5 (1995) C8-783

Kay, E., Adv. Electronics and Electron Phys., 17 (1962), 245

Kelly, R., "The Mechanisms of Sputtering-Part. I Prompt and Slow Collisional Sputtering", Sol. St. Phys. 16, 275, 1984

Kim, J. J., P. Moine and D. A. Stevenson, Scripta Metall., 20 (1986), 243

Leawer, K. D. and B. N. Chapman, "Thin Films", Wykeham Publication, London, 1981

Nobes, M. J., J. C. Colligon and G. Carter, J. Mat. Sci. , 4:730 (1969)

Oechsner, H., "Sputtering of Polycrystalline Metal Surfaces at Oblique Ion Bombardment in 1 keV Range", J. Phys. 261, 37, 1973

Okutani, T., M. Shikata, S. Ichimura and R. Shimizu, "Angular Distributions of Si Atoms Sputtered by keV Ar^+ ions", J. Appl. Phys., 51(5), 1980

Olson, R. R., M. E. King and G. K. Wehner, "Mass Effects on Angular Distribution of Sputtered Atoms", J. Appl. Phys., 50(5), 3677, 1979

Rossnagel, S. M. and R. S. Robinson, J. Vac. Sci., 20(1982), 506

Rossnagel, S. M. and H. F. Kaufman, "Current-Voltage relations in Magnetrons", J. Vac. Sci. Technol. A6(2), 233, 1988

Selinder, T. I., G. Larsson and U. Helmersson, "Resputtering Effects on the Stoichiometry of $YBa_2Cu_3O_x$ Thin Films", Journal of Applied Physics, Vol. 69(7), 1 Jan. 1991, pp 390-5.

Scherzer, B. M. U., "Development of Surface Topography Due to Gas Ion Incorporation", in R. Behrisch, ed., Sputtering by Particle Bombardment II, Springer-Verlag, Berlin, 1983

Shugo, Y., Y. Yagi and T. Honma, Bull. Res. Inst. of Mineral Dressing and Metallurgy, Tohoku University, 43 No. 2, 139(1987)

Sigmund, P. and C. Claussen, "Sputtering from Elastic Collision Spikes in Heavy –Ion – Bombardment Metals", Phys. Rev. 184(2), 383, 1981

Sigmund, P., J. Vac. Sci. Technol., 17:396 (1980)

Sigmund, P., J. Mat. Sci., 8:1545 (1973)

Sivokha, V. P., A. S. Savvinov, V. P. Vornin and V. N. Khachin, Phys. Met. Metal., 56 (112-116), 1983

Somekh, R. E., "The Thermalization of Energetic Atoms during the Sputtering Process", J. Vac. Sci. Technol., A2(3), 1285, 1984

Townsend, P. D., J. C. Kelly and N. E. W. Hartely, Ion Implantation, Sputtering, and their Applications, Academic Press, London, 1976

Turner, G. M., I. S. Falconer, B. W. James and D. R. Mckenzie, "Monte Carlo Calculation of the Properties of Sputtered Atoms at a Substrate Surface in a Magnetron Discharge", J. Vac. Sci. Technol., A 10(3), 455, 1992

Van Loo, F. J. J., G. F. Bastin and J. H. Leenen, Journal of Less Common Metallurgy, 57 (1978), 11

Vossen, J. L., J. Vac. Sci. Technol., 8:S12 (1971)

Waits, P. K., in "Thin Film Processes", eds. J. L. Vossen and W. Kern, Academic Press, New York, (1978), 131

Wang, F. E., W. J. Buehler, and S. J. Pickart, Journal of Applied Physics, Vol. 36, 1965, pp. 3232

Wasilewski, R. J., S. R. Butler, J. E. Hanlon and D. Worden, Metall. Trans., 2(1971), 229

Wayman, C. M., "Phase Transformation, Nondiffusive", Physical Metallurgy, 3rd ed. Elsevier Science Publishers (1983), pp. 1032-78

Weast, R. C., ed., Handbook of Chemistry and Physics, 56th, CRC Press, Cleveland OH, 1975

Wehner, G. K. and D. Rosenberg, "Angular Distribution of Sputtered Material", J. Appl. Phys., 31(1), 1960

Westwood, W. D., "Calculation of Deposition Rates in Diode Sputtering Systems", J. Vac. Sci. Technol., 15(1), 1, 1978

Xie, C. Y., L. C. Zhao and T. C. Lei, Scripta Metall., 24(1990), 1753

Yamamura, Y., Y. Itikawa and N. Itoh, Angular Dependence of Sputtering Yields of Monoatomic Solids, Research Information Center, Institute of Plasma Physics, Nagoya University, Japan, 1983

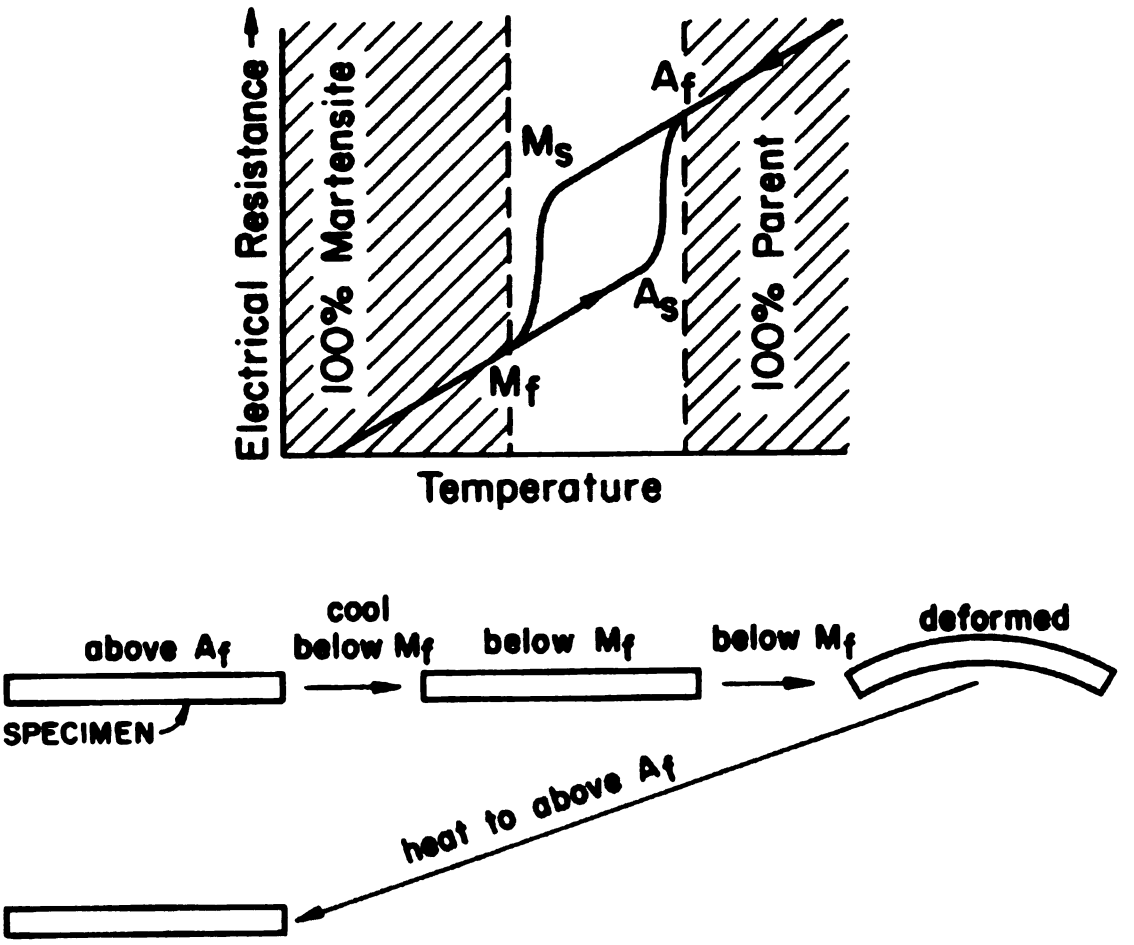

Figure 2-1 Schematic of Shape Memory Effect and Transformation Temperatures Observed in Electrical Resistivity vs. Temperature Plot [Duerig, 1990].

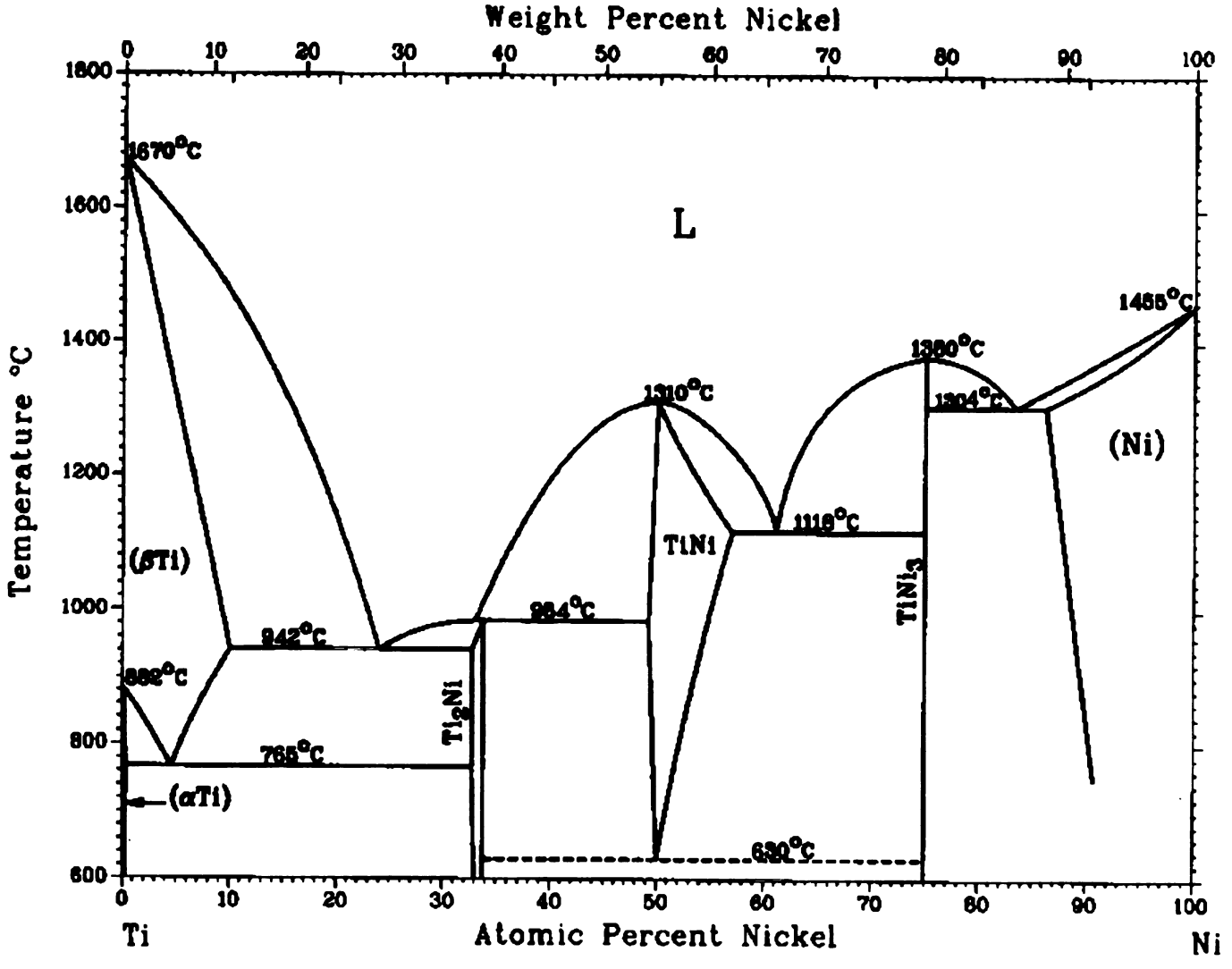

Figure 2-2 Binary Phase Diagram of TiNi [Binary Alloys Phase Diagram (ASM), 1987].

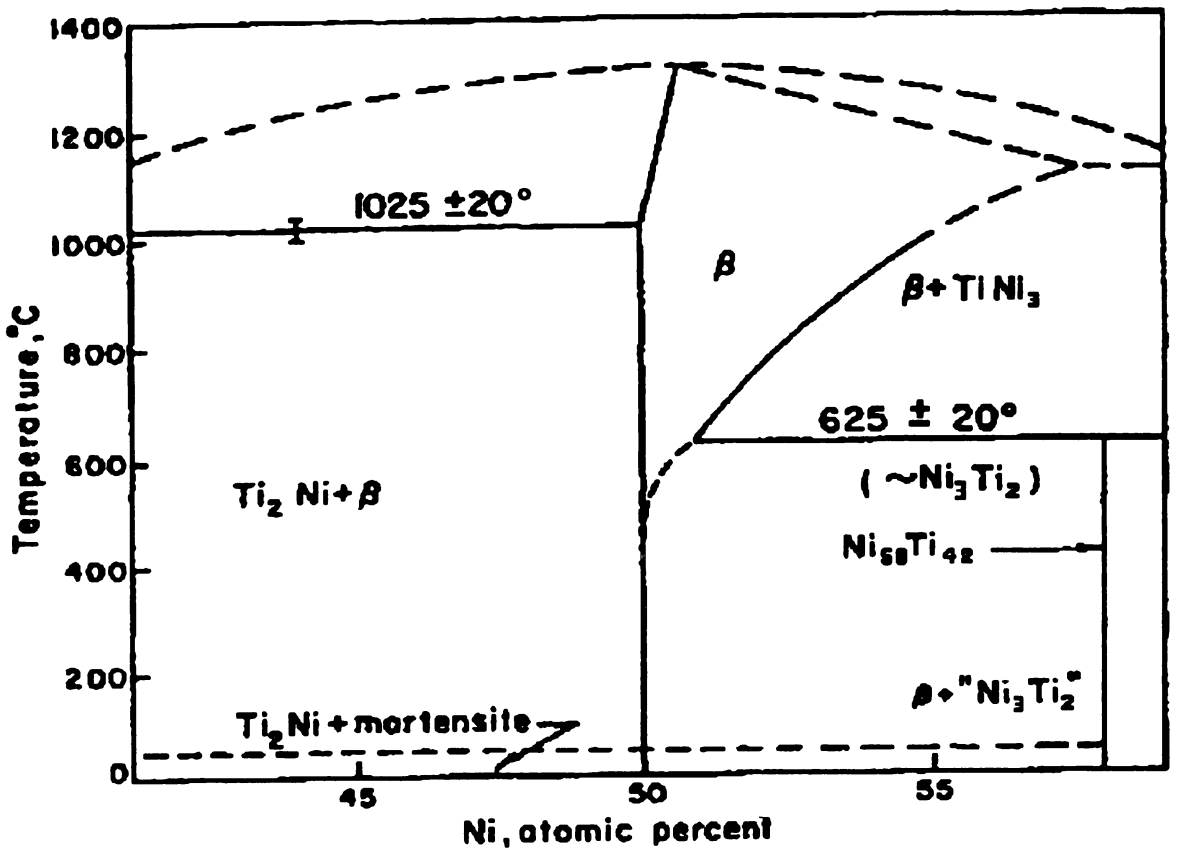

Figure 2-3 Equilibrium Phase Diagram Near Equiatomic Composition at Low Temperature of TiNi Binary System Proposed by Wasilewski *et al.*

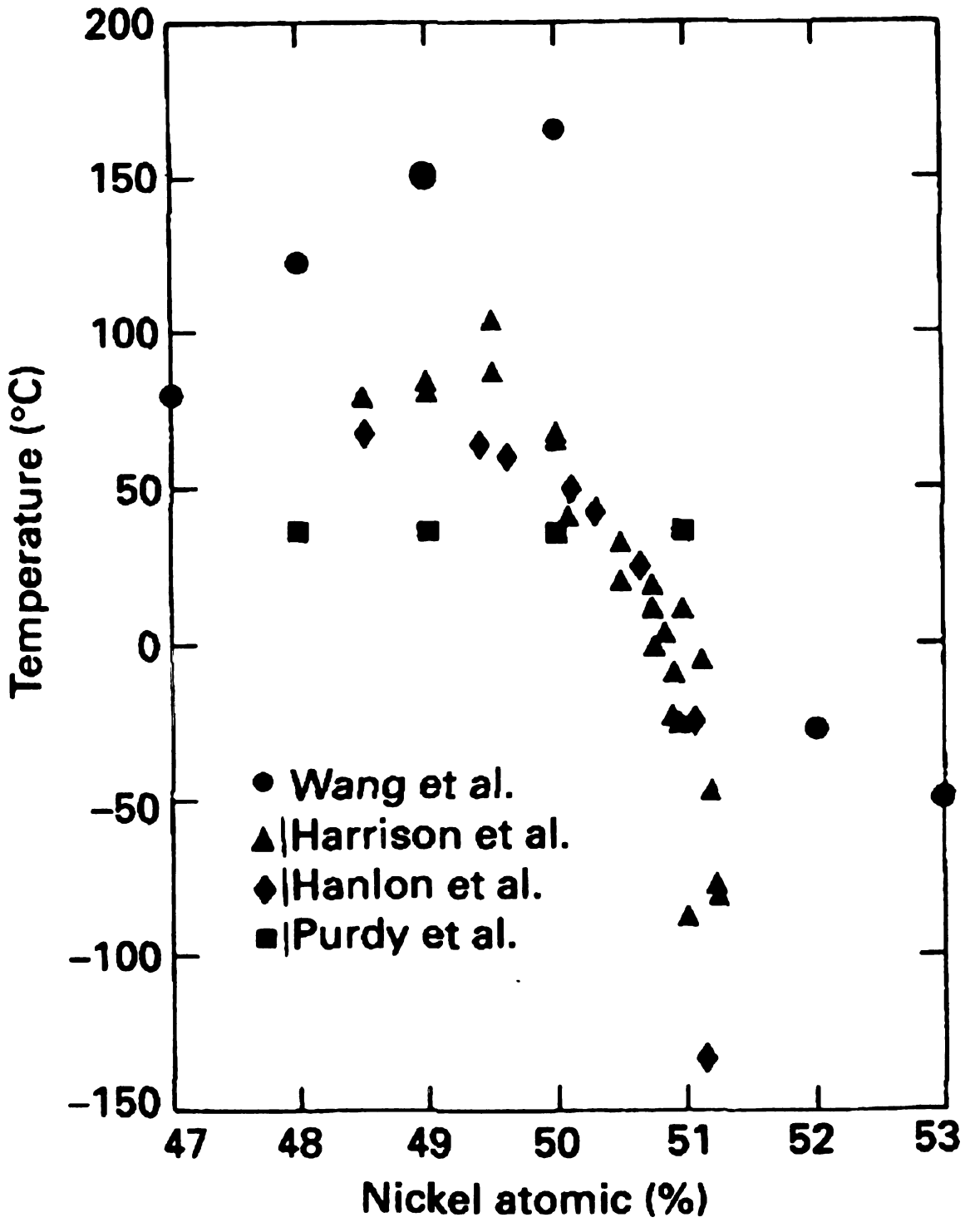

Figure 2-4 Martensite Start Temperatures as a Function of Ni Content [Melton, 1990; Wang, 1965].

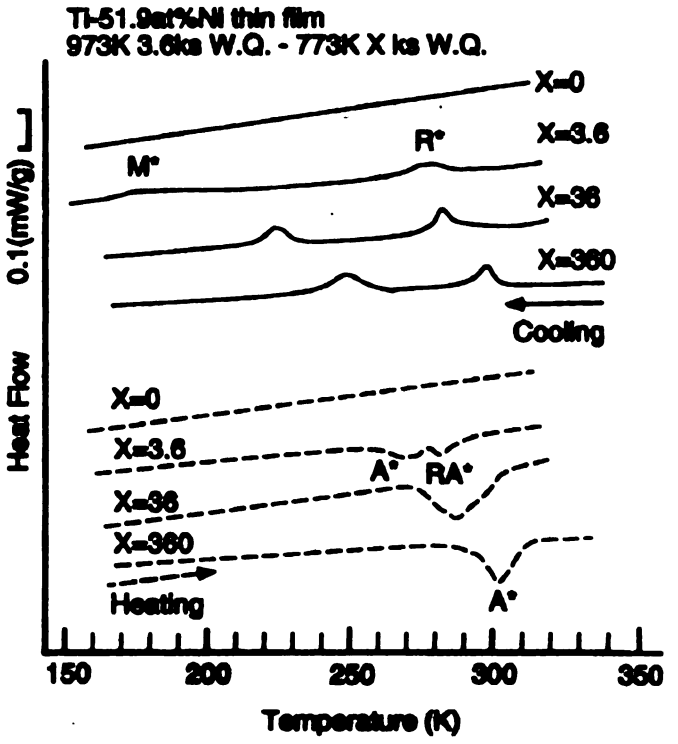

Figure 2-5 (a) Effect of Aging Time on Ni- rich TiNi Thin Films [Miyazaki, 1999].

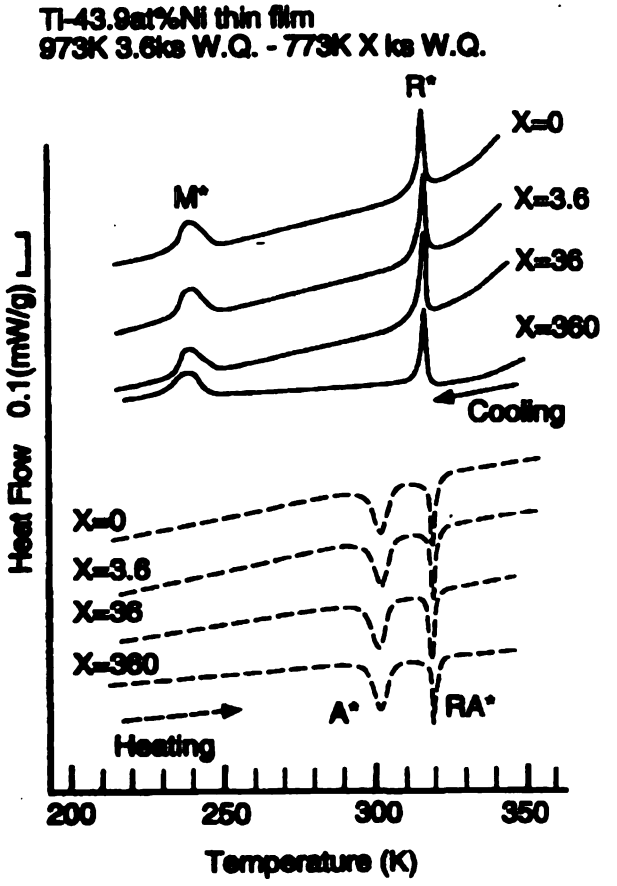

Figure 2-5 (b) Effect of Aging Time on Ti- rich TiNi Thin Films [Miyazaki, 1999].

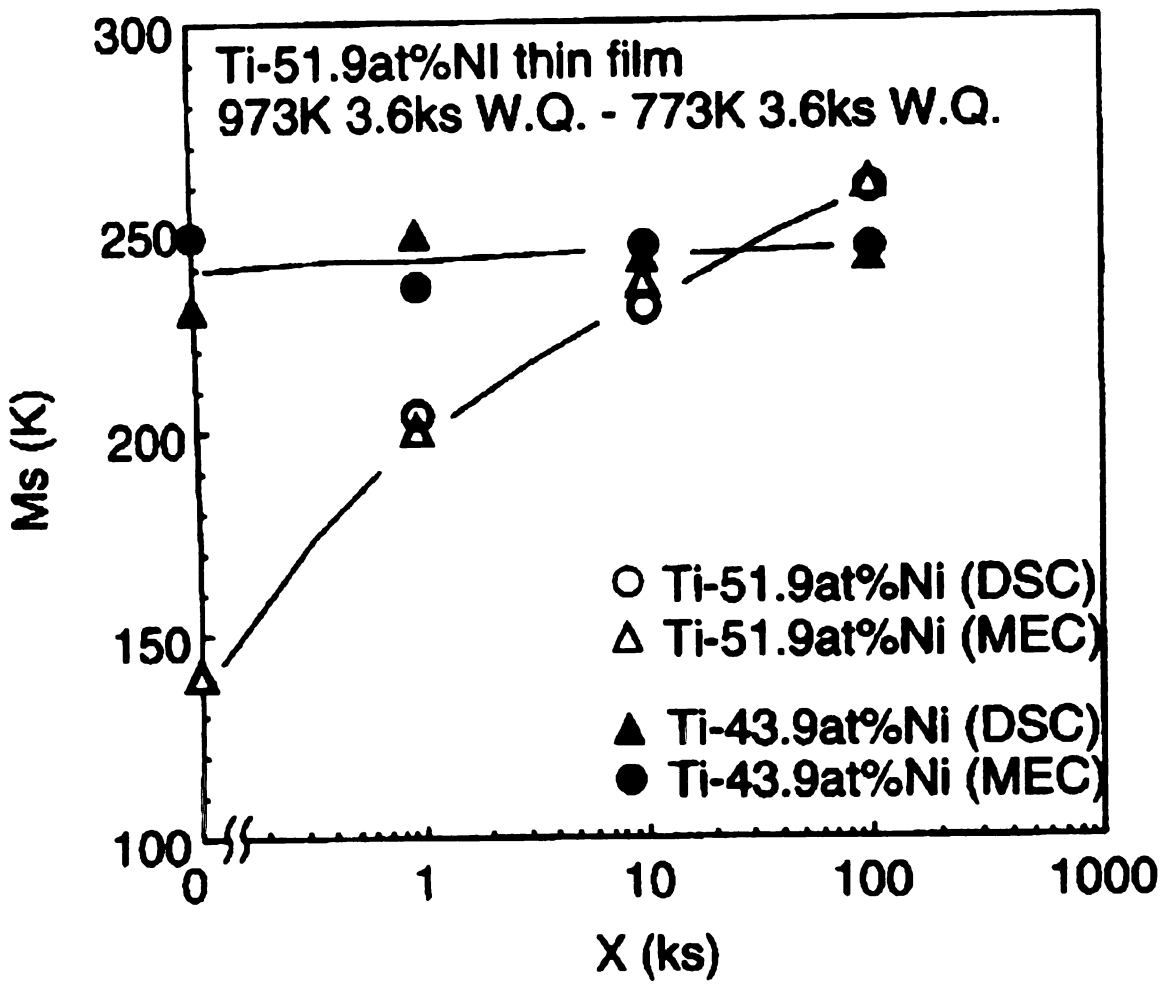

Figure 2-6 DSC Results of the Effects of Aging Time on M_s Temperature for Ni and Ti-Rich TiNi Thin Films [Miyazaki, 1999].

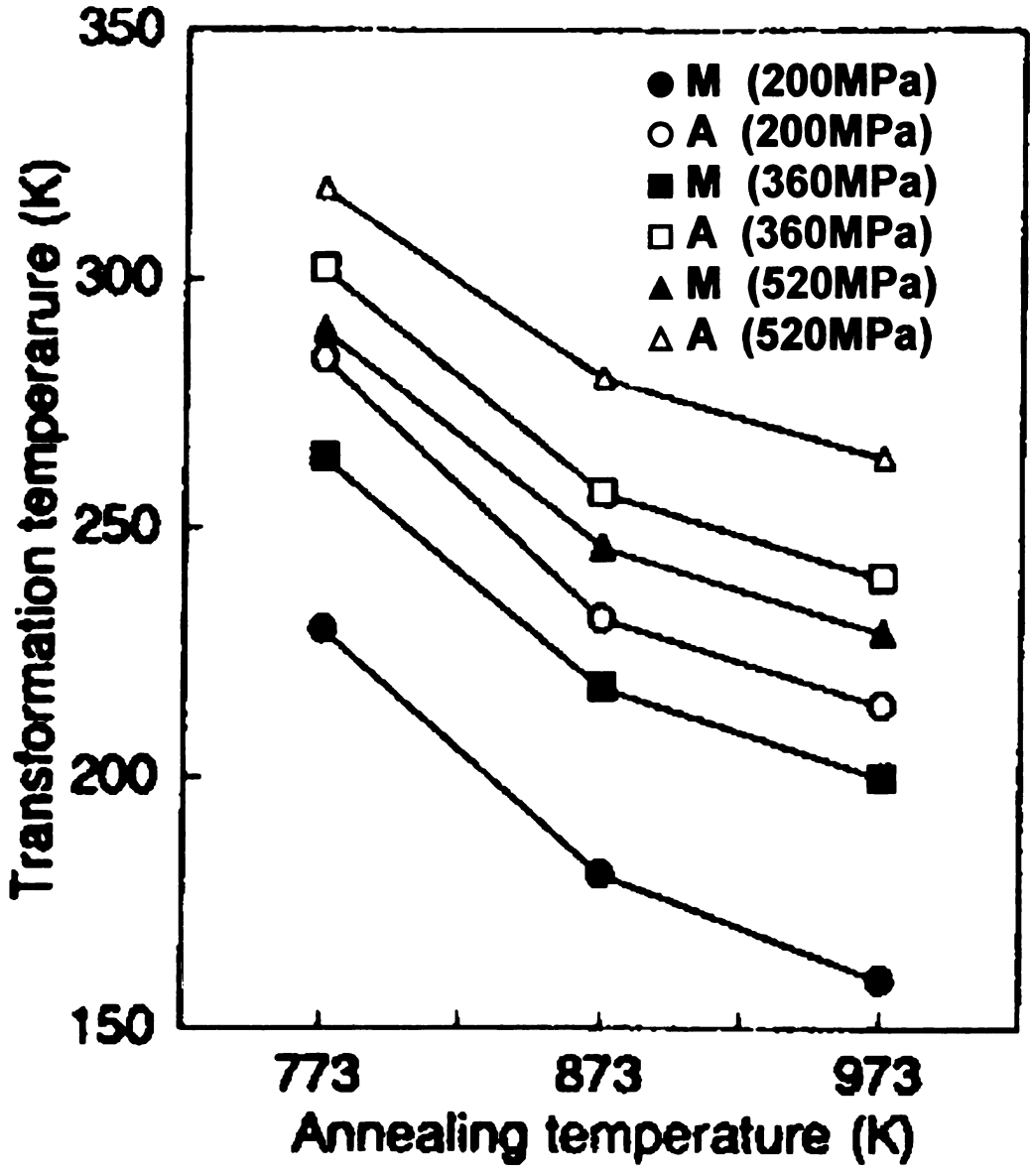

Figure 2-7 The Effect of Solutionizing Temperature on Transformation Temperatures in Ni-rich TiNi Thin Films Observed by Strain-Temperature Curves at Constant Stress [Ishida, 1995].

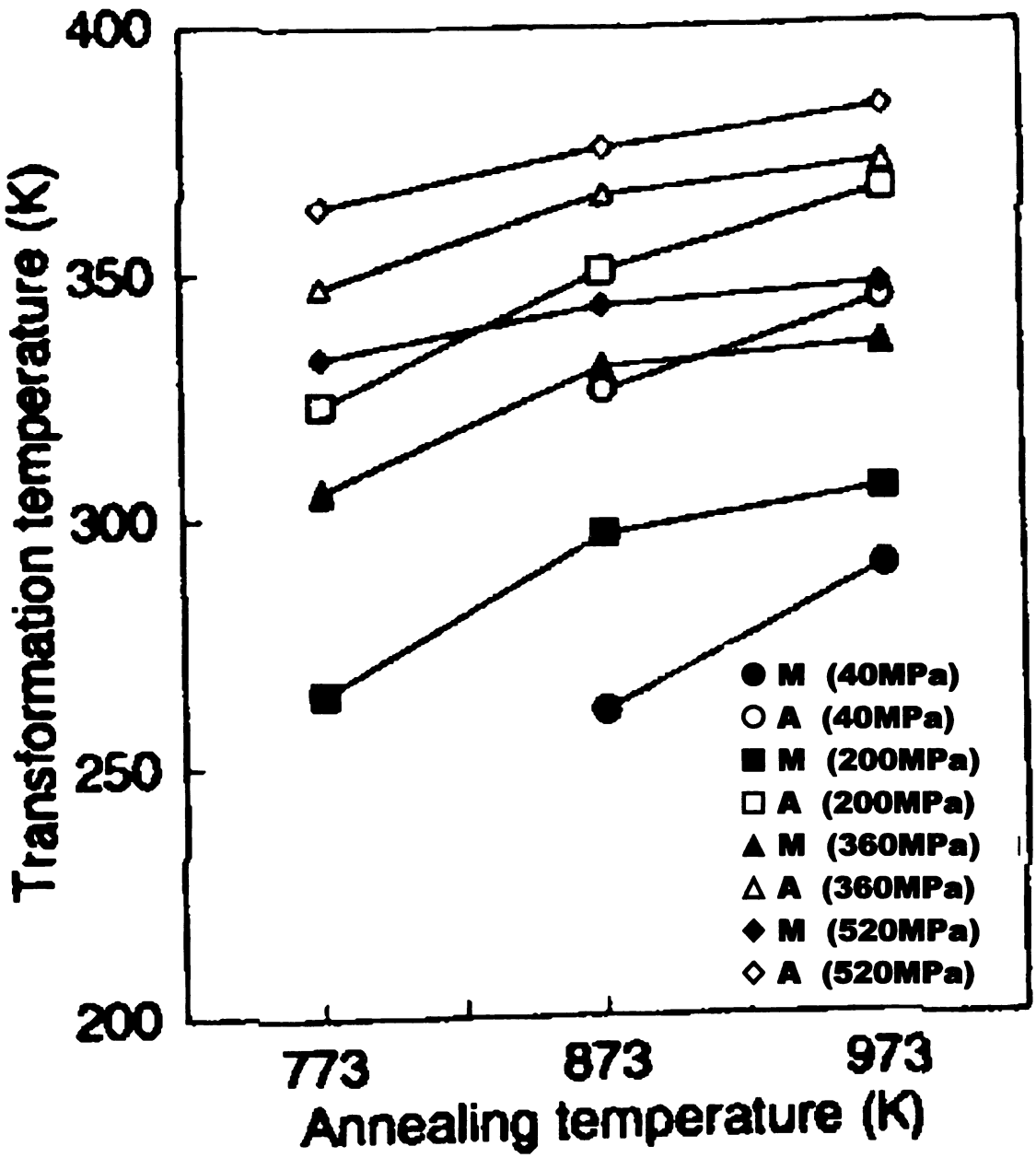

Figure 2-8 The Effect of Solutionizing Temperature on Transformation Temperatures in Ti-rich TiNi Thin Films Observed by Strain-Temperature Curves at Constant Stress [Ishida, 1995].

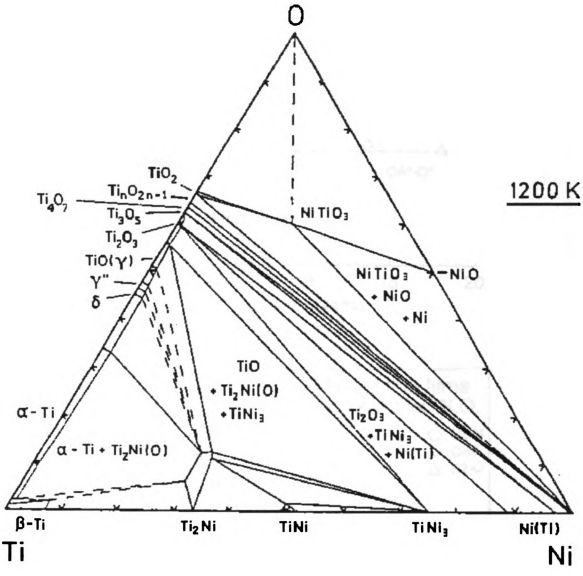

Figure 2-9 Titanium-Nickel-Oxygen Phase Diagram [Chattopadhyay, 1983].

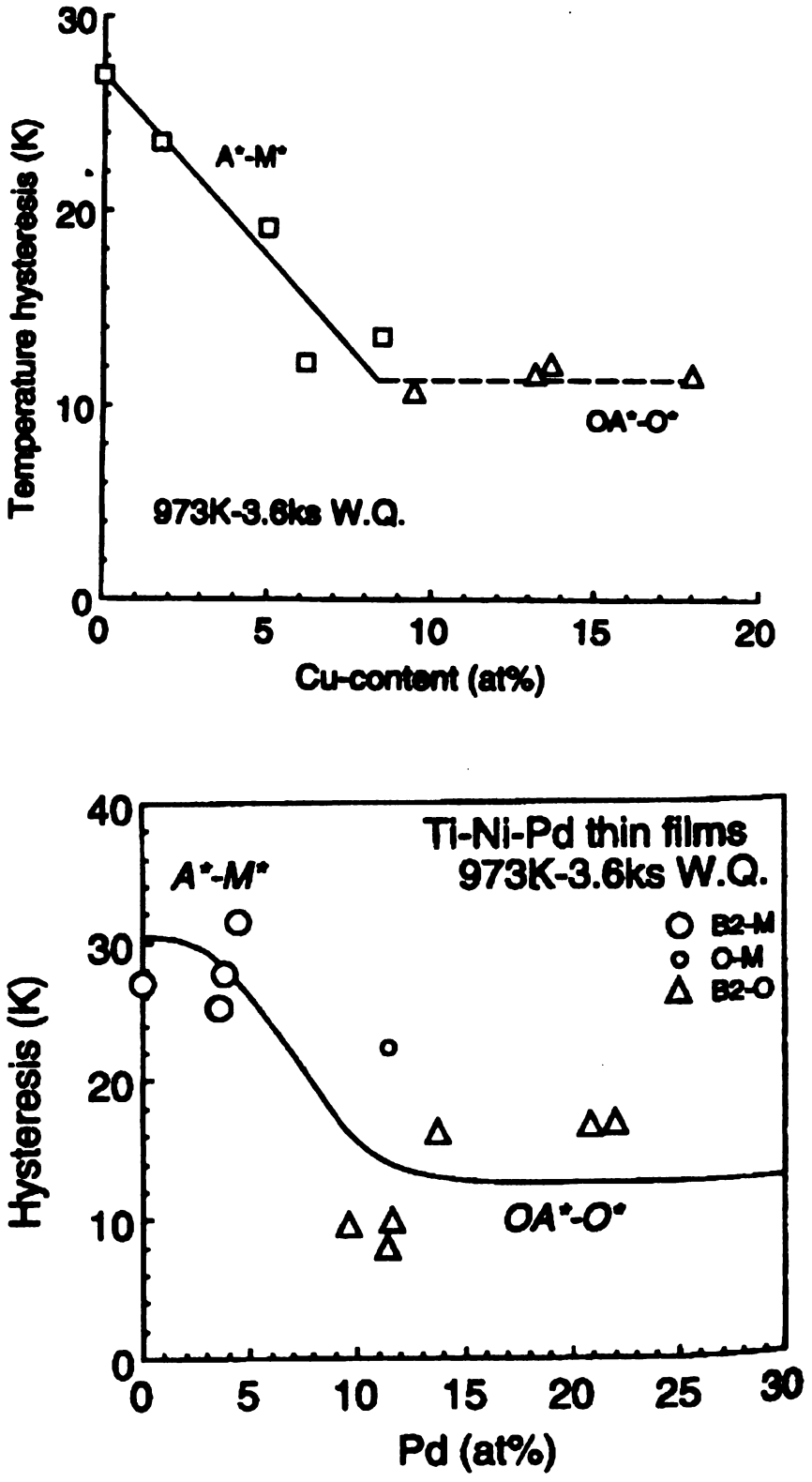

Figure 2-10 The Effect of Cu and Pd Content on the Thermal Hysteresis[Miyazaki, 1999].

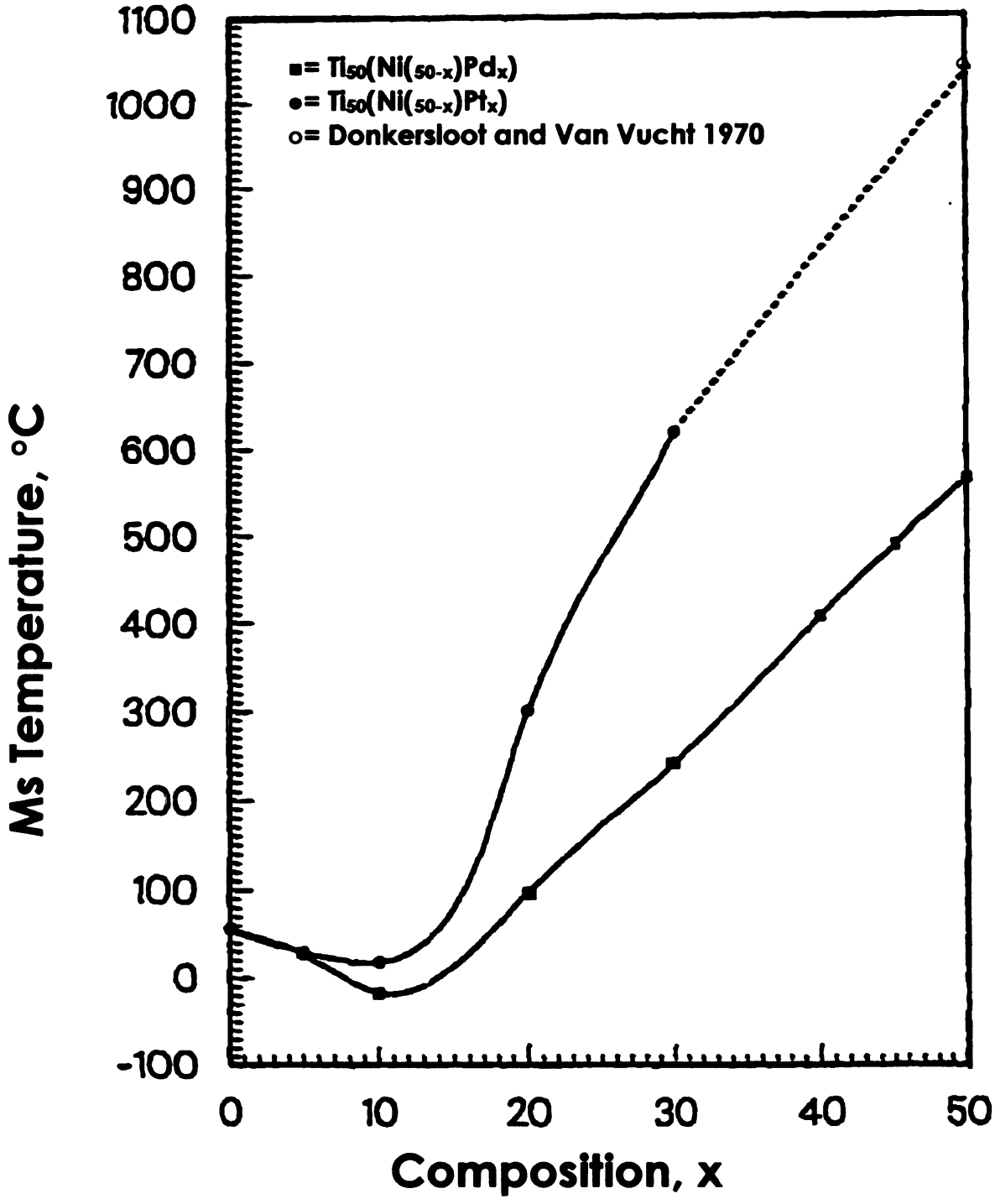

Figure 2-11 M_s Temperature as a Function of Pd and Pt at. % [Lindquist, 1988].

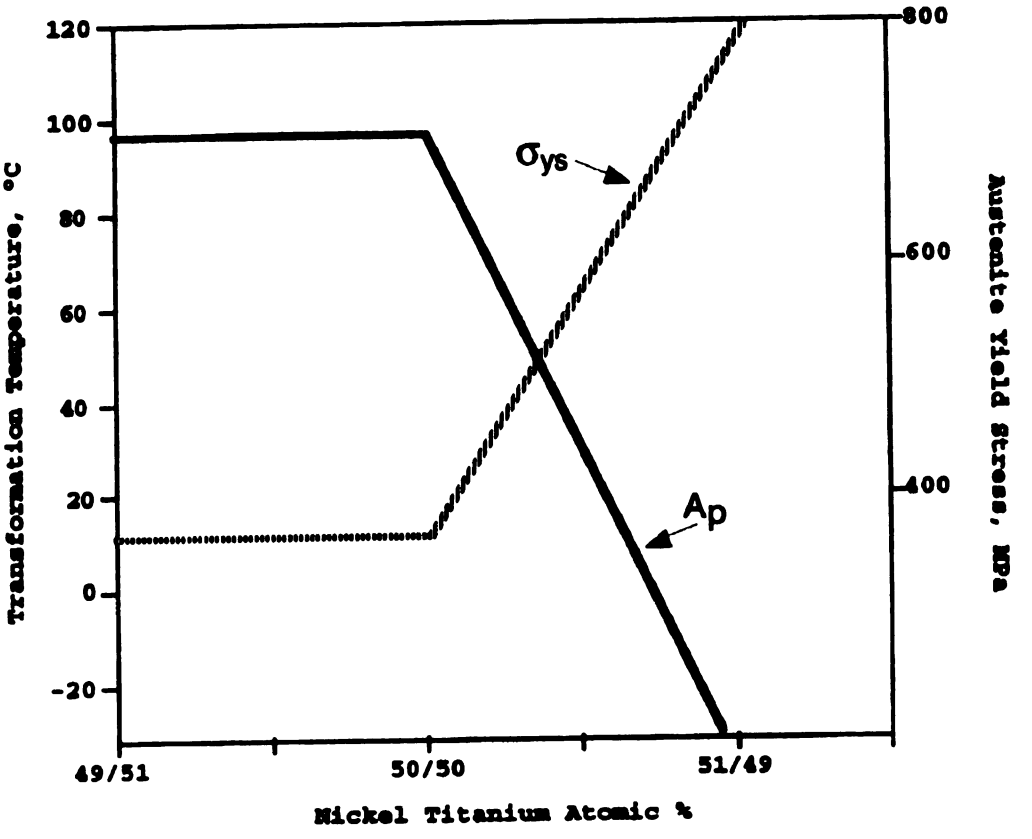

Figure 2-12 The Effect of Composition on Austenitic Strength [Hodgson, 2000].

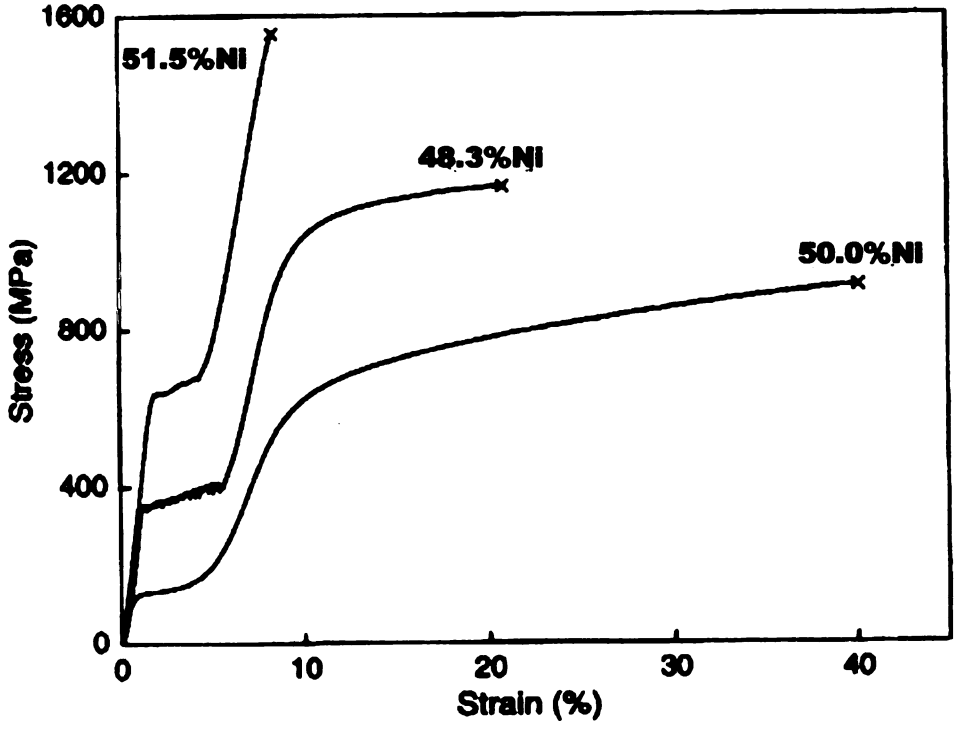

Figure 2-13 Stress-Strain Curves for Various TiNi Thin Films Compositions [Ishida, 1999].

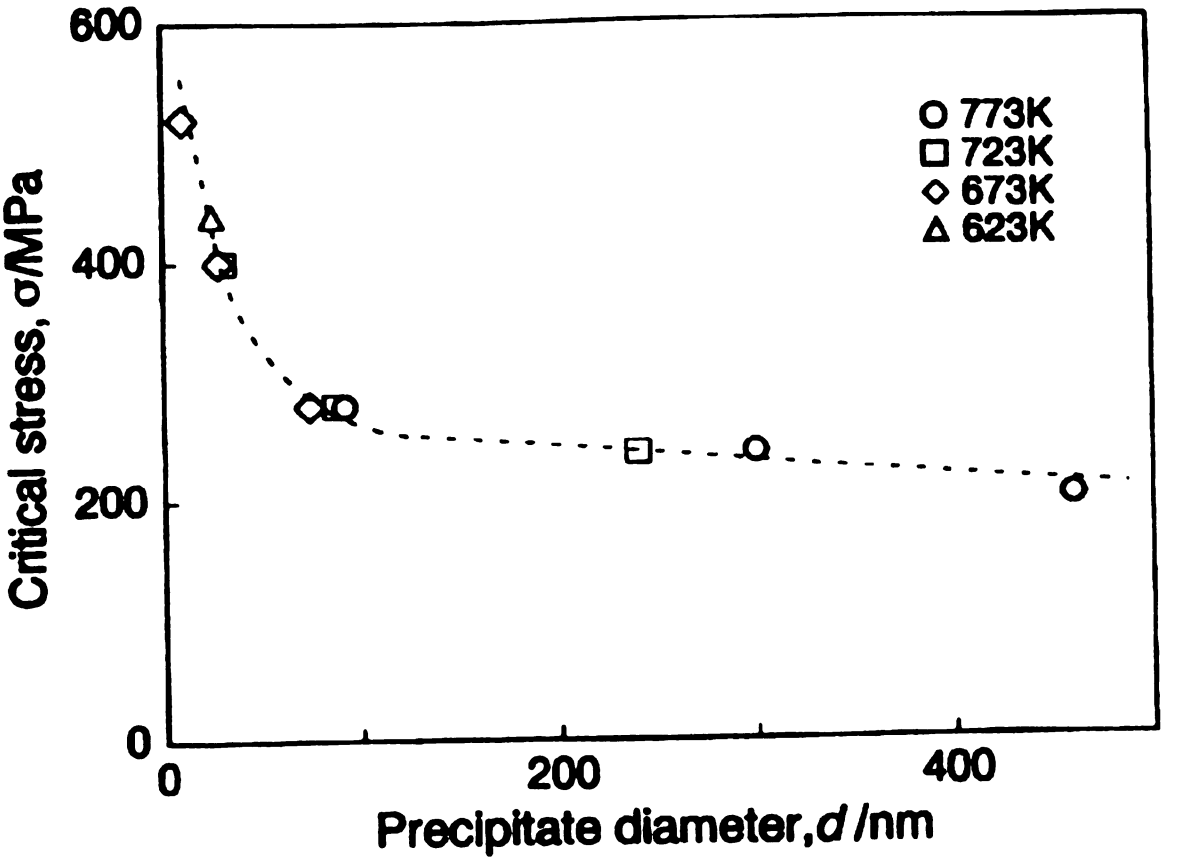

Figure 2-14 The Effect of Precipitate Diameter on the Critical Stress for Slip in Austenite [Ishida, Microstructure 1999].

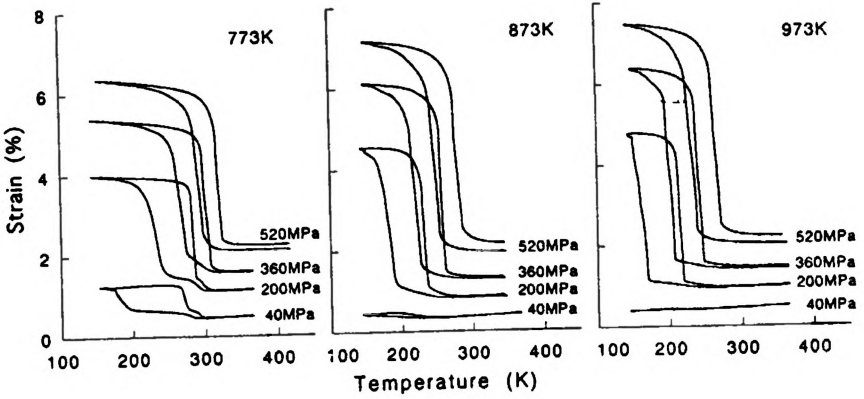

Figure 2-15 Strain-Temperature Curves at Constant Stress of Nickel-Rich TiNi Thin Films Annealed at Various Temperatures for 3.6 ks [Ishida,1995].

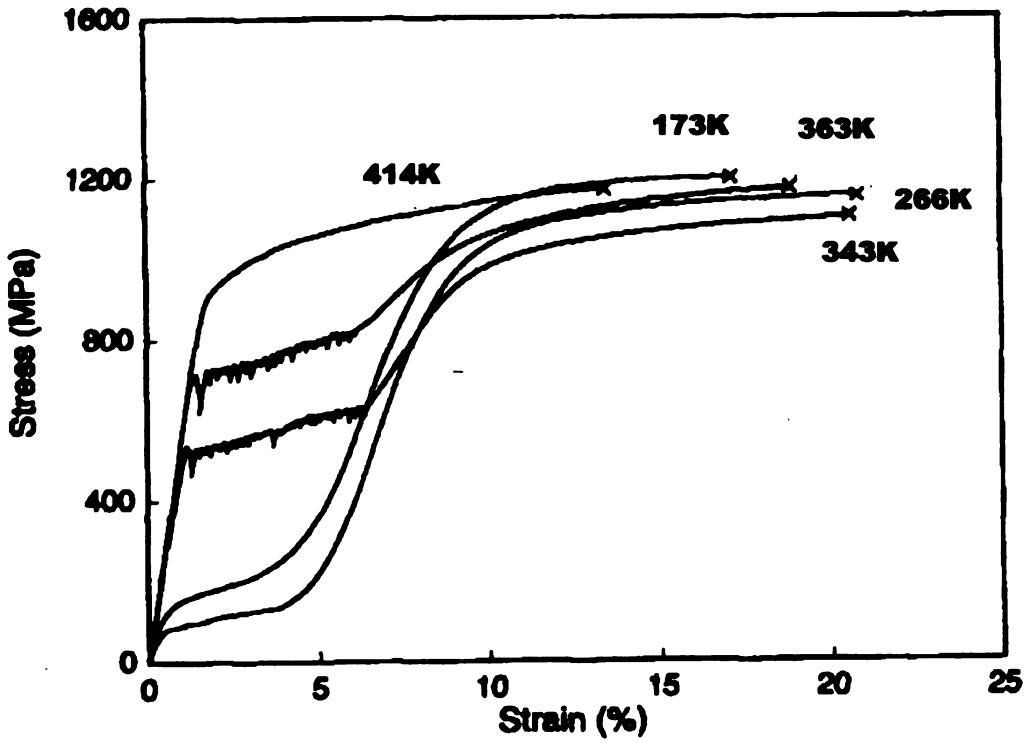

Figure 2-16 (a) Stress-Strain Curve of Ti-48.2 at.% Ni Thin Films Annealed at 773 K for 300s [Ishisda, 1999].

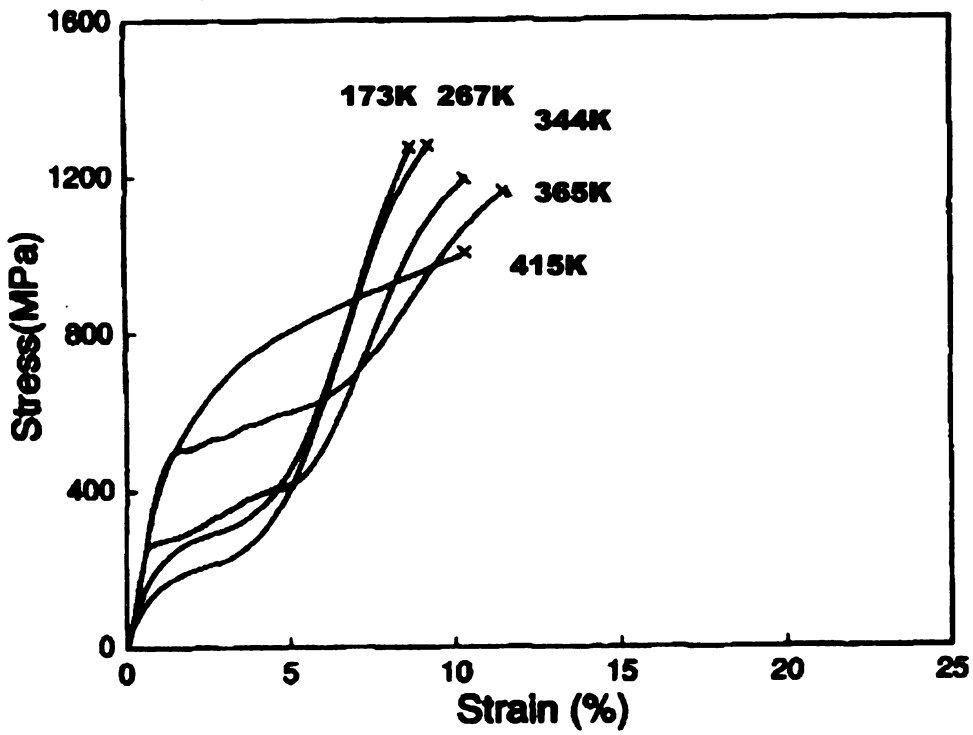

Figure 2-16 (b) Stress-Strain Curve of Ti- 48.2 at.% Ni Thin Films Annealed at 873 K for 3.6 ks [Ishisda, 1999].

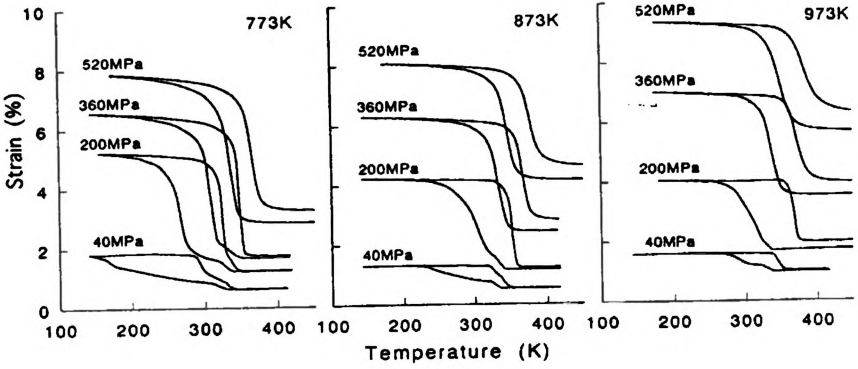

Figure 2-17 Strain-Temperature Curves at Constant Stress of Titanium-Rich TiNi Thin Films Annealed at Various Temperatures for 3.6 ks [Ishida,1995].

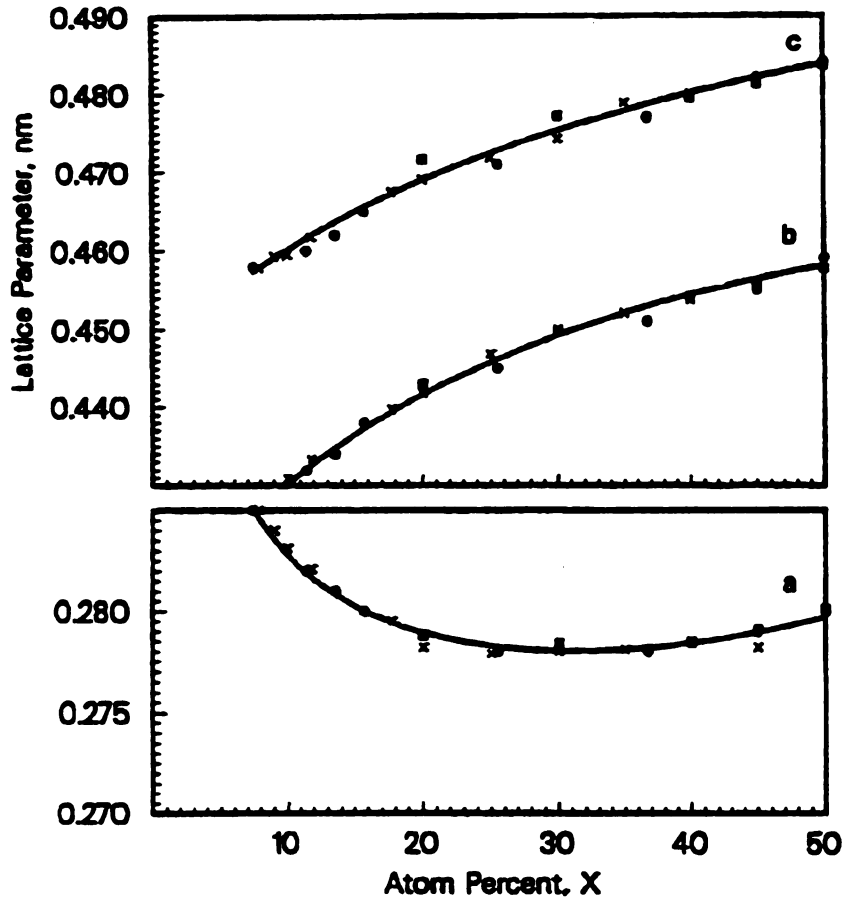

Figure 2-18 Lattice Parameter Data for B19 Martensite as a Function of Pd at. % Reported by Lindquist (■), Sivokha *et al.* (●), and Shugo *et al.* (X).

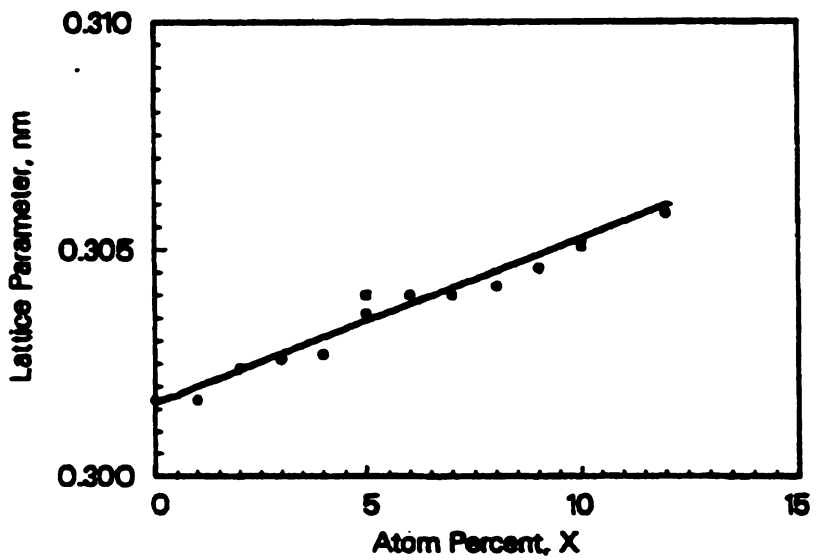

Figure 2-19 Lattice Parameter Data for B2 Austenite as a Function of Pd at. % Reported by Lindquist (■) and Shugo *et al.* (●).

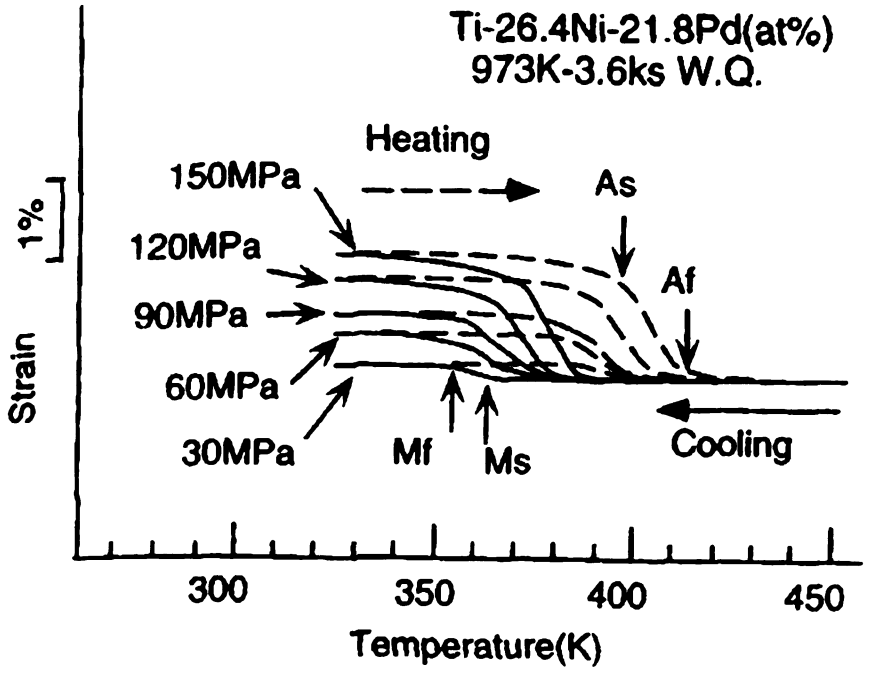

Figure 2-20 Strain-Temperature Curves for Ti-(Ni+Pd) Alloy [Miyazaki, 1999].

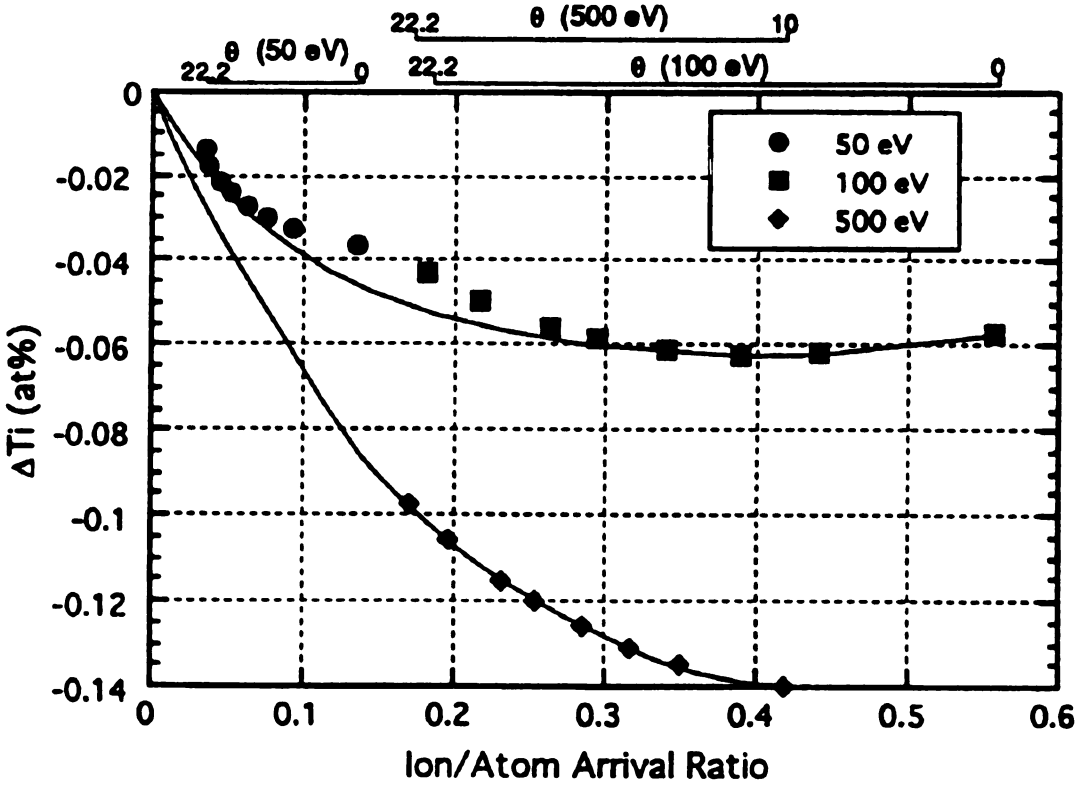

Figure 2-21 Comparison of the Ti Content of IBAD TiNi Films with the Expected Film Composition as Function of I/A Ratio in the Absence of an Assisted Beam [Chang, 1992].

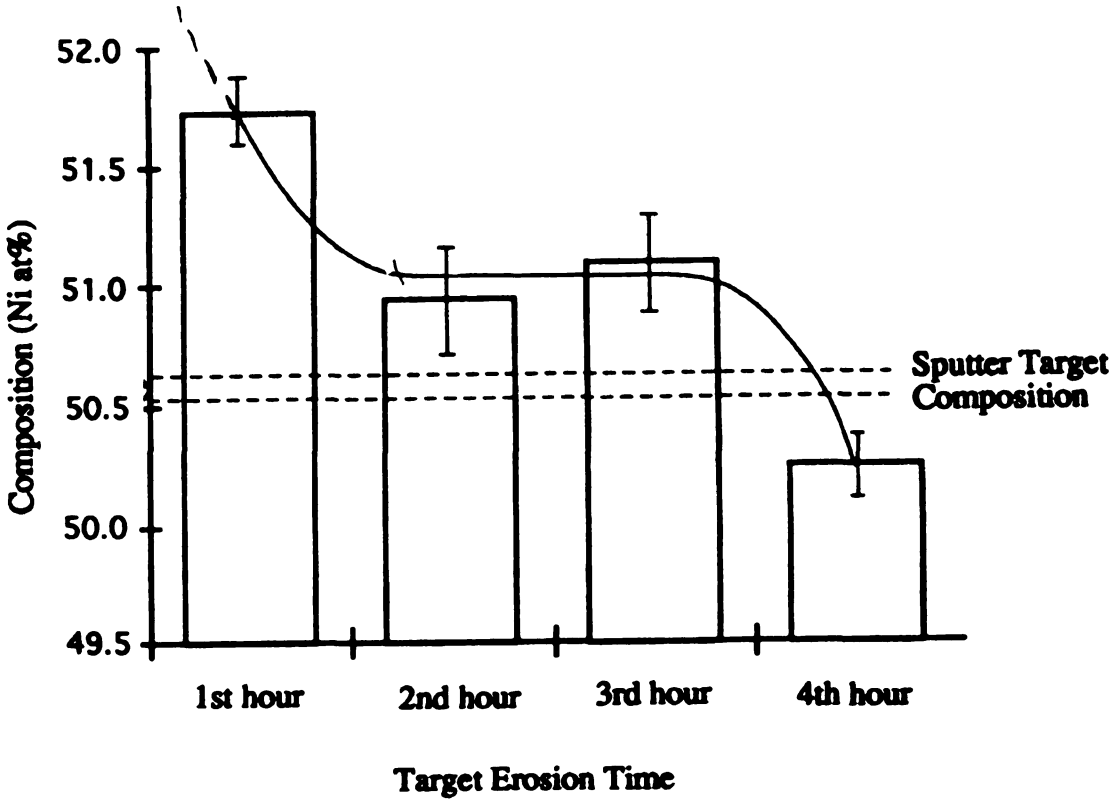

Figure 2-22 The Effect of Target Erosion on Composition [Lee, 1994].

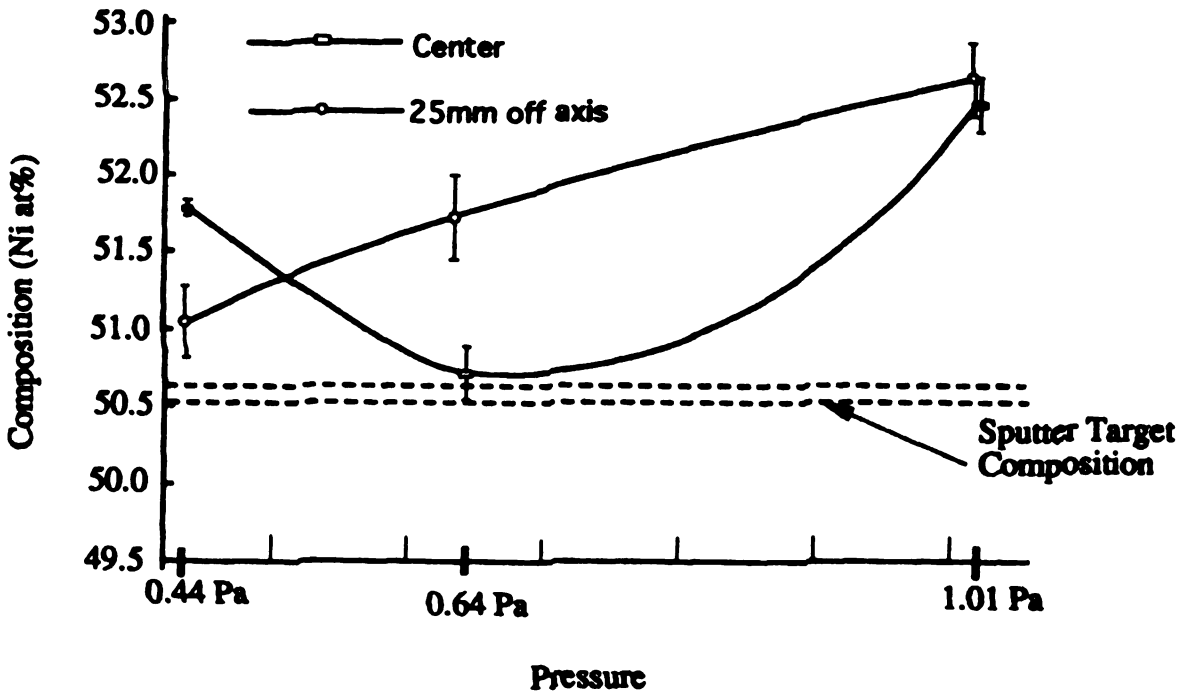

Figure 2-23 The Effect of Pressure on the Composition [Lee,1994].

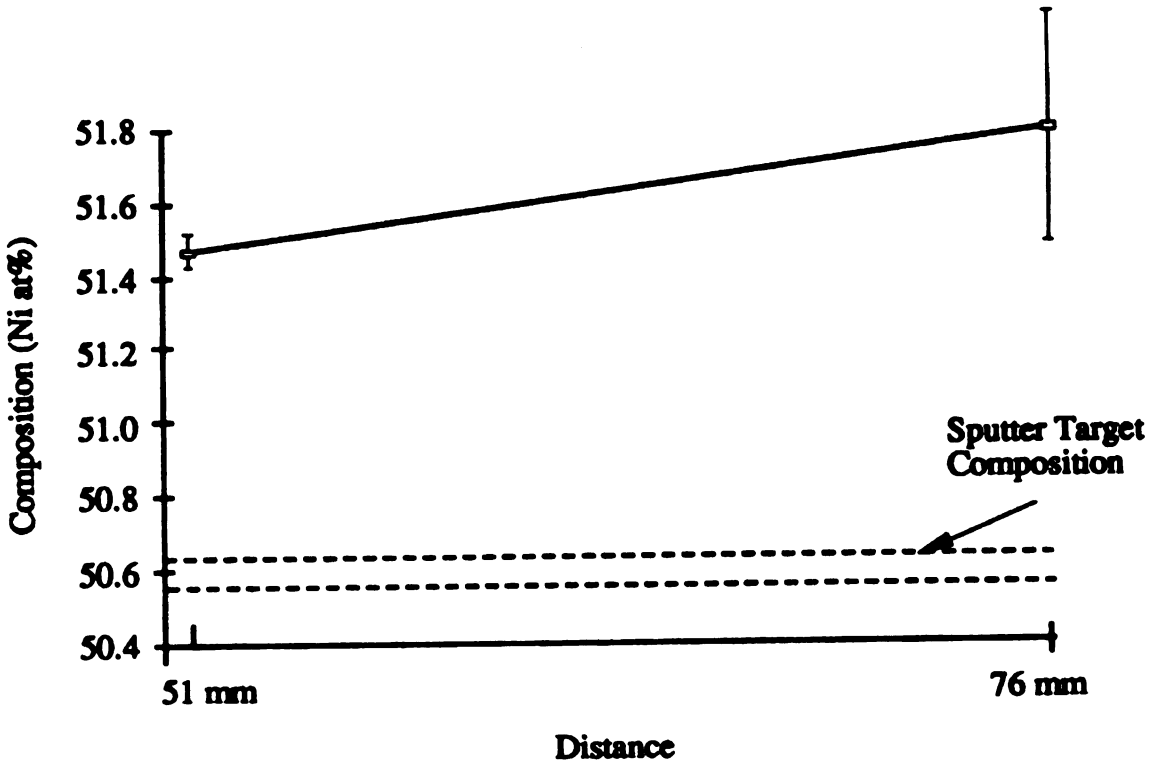

Figure 2-24 The Effect of Target-Substrate Distance on Composition [Lee, 1994].

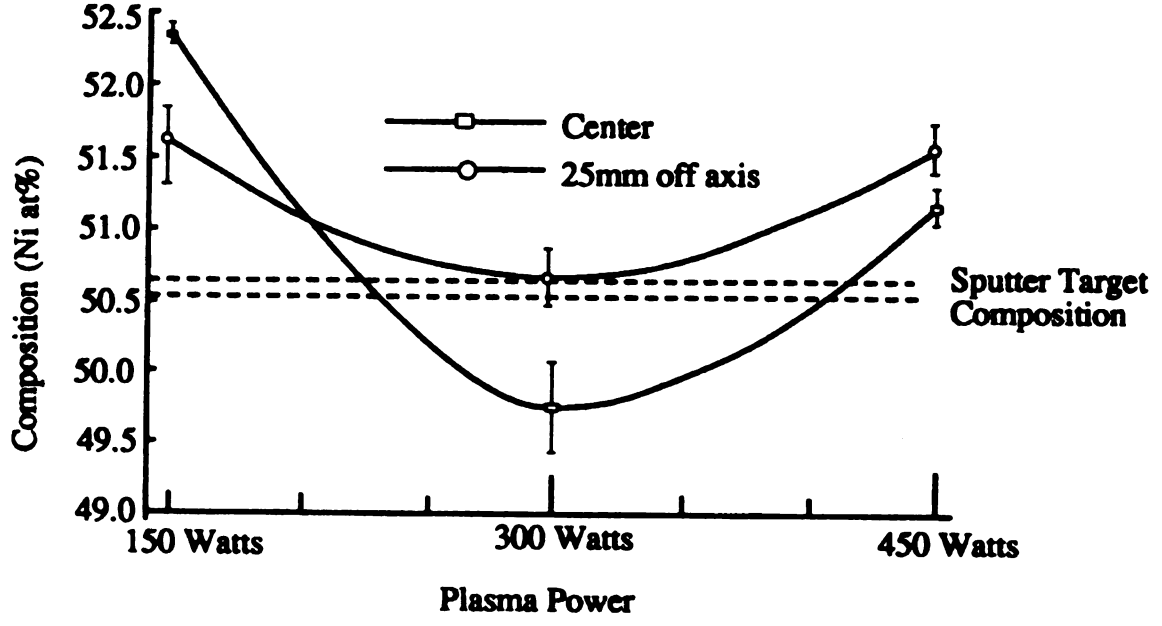

Figure 2-25 The Effect of Power on Composition [Lee, 1994].

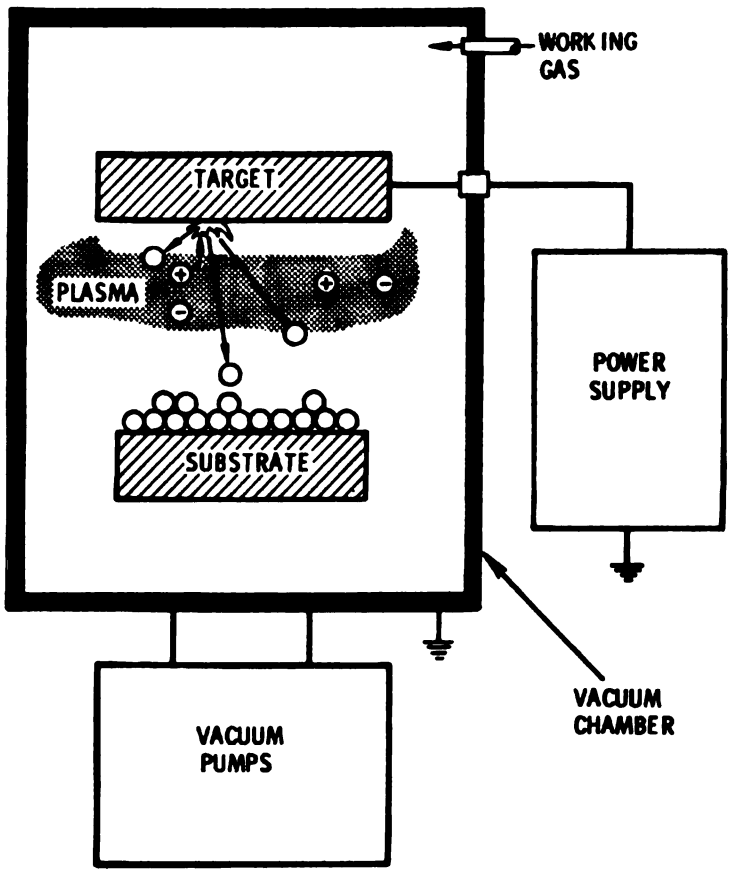

Figure 2-26 Schematic of Sputtering Apparatus [Bunshah, 1994].

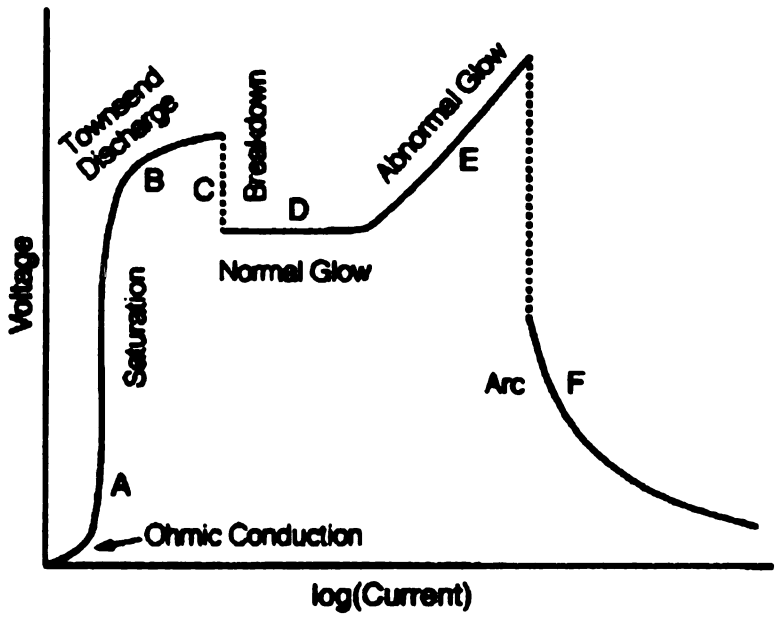

Figure 2-27 The Voltage-Current Relationship in a DC Discharge [Mahan, 1999].

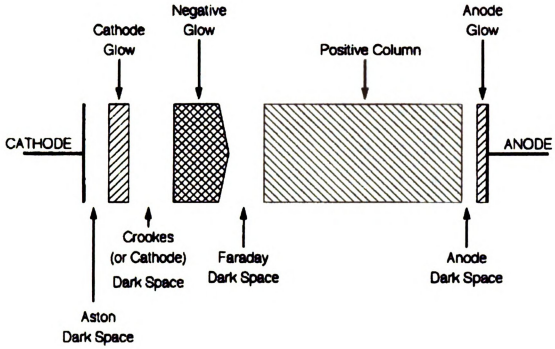

Figure 2-28 The Luminous and Dark Regions of DC Glow Discharge [Mahan, 1999].

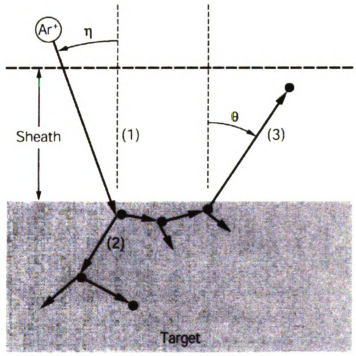

Figure 2-29 A Collision Cascade Resulting in a Sputter Atom or Recoil [Mahan, 1999].

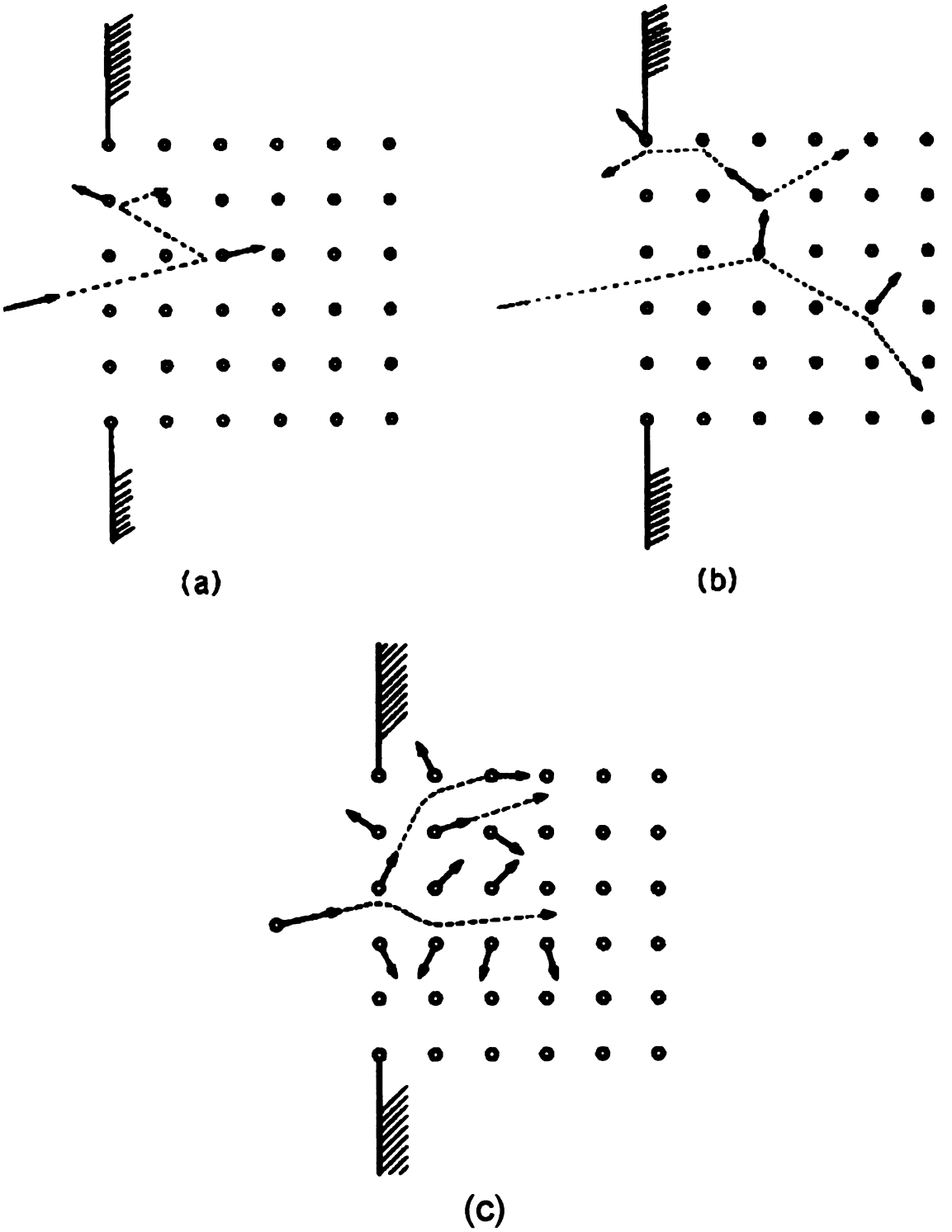

Figure 2-30 The Three Energy Regimes of Collision Cascade (a) Single Knock-on Regime, (b) Linear Cascade (c) Spike Regime [Sigmund ,1981].

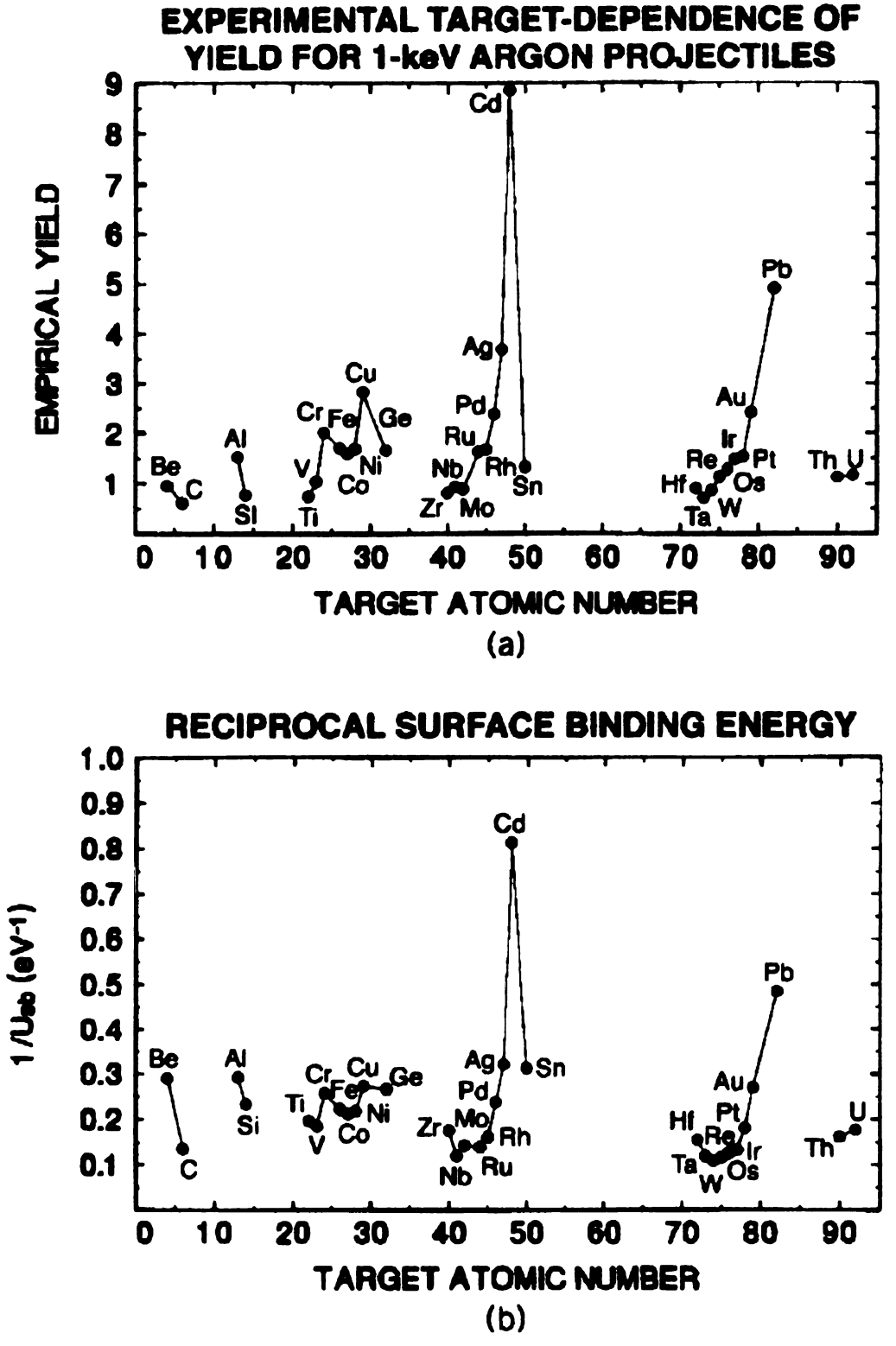

Figure 2-31 The Effect of Surface Binding Energy on Yield [Mahan and Vantomme, 1999].

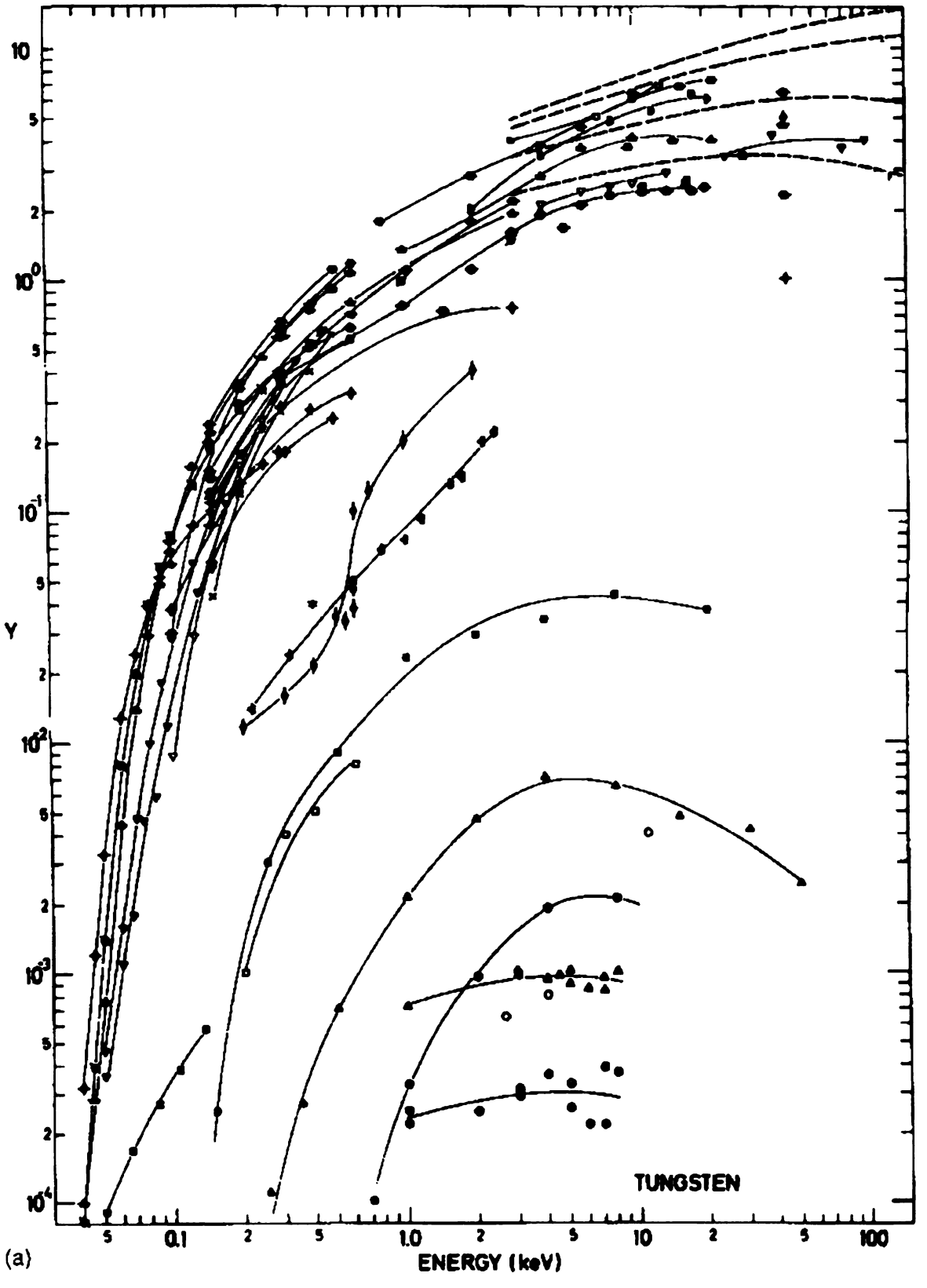

Figure 2-32 The Projectile Energy Dependence on Yield for Tungsten Target Struck by Various Projectiles [Anderson, 1981].

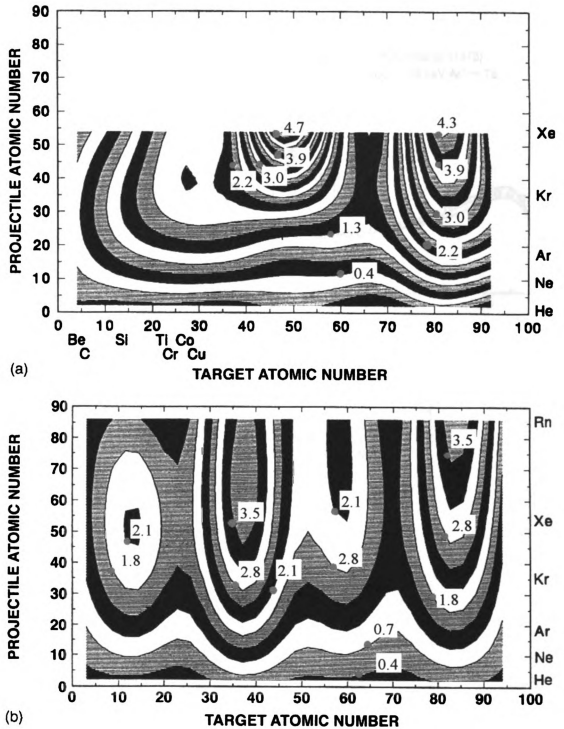

Figure 2-33 A Contour Plot Showing the Effect of Projectile Mass on Sputter Yield with Target Atomic Number (a) Yield Data from Empirical Formula Developed by Matsunami et al. [1984] (b) Yield data from a Simplified Collision Model [Mahan and Vantomme, 1999].

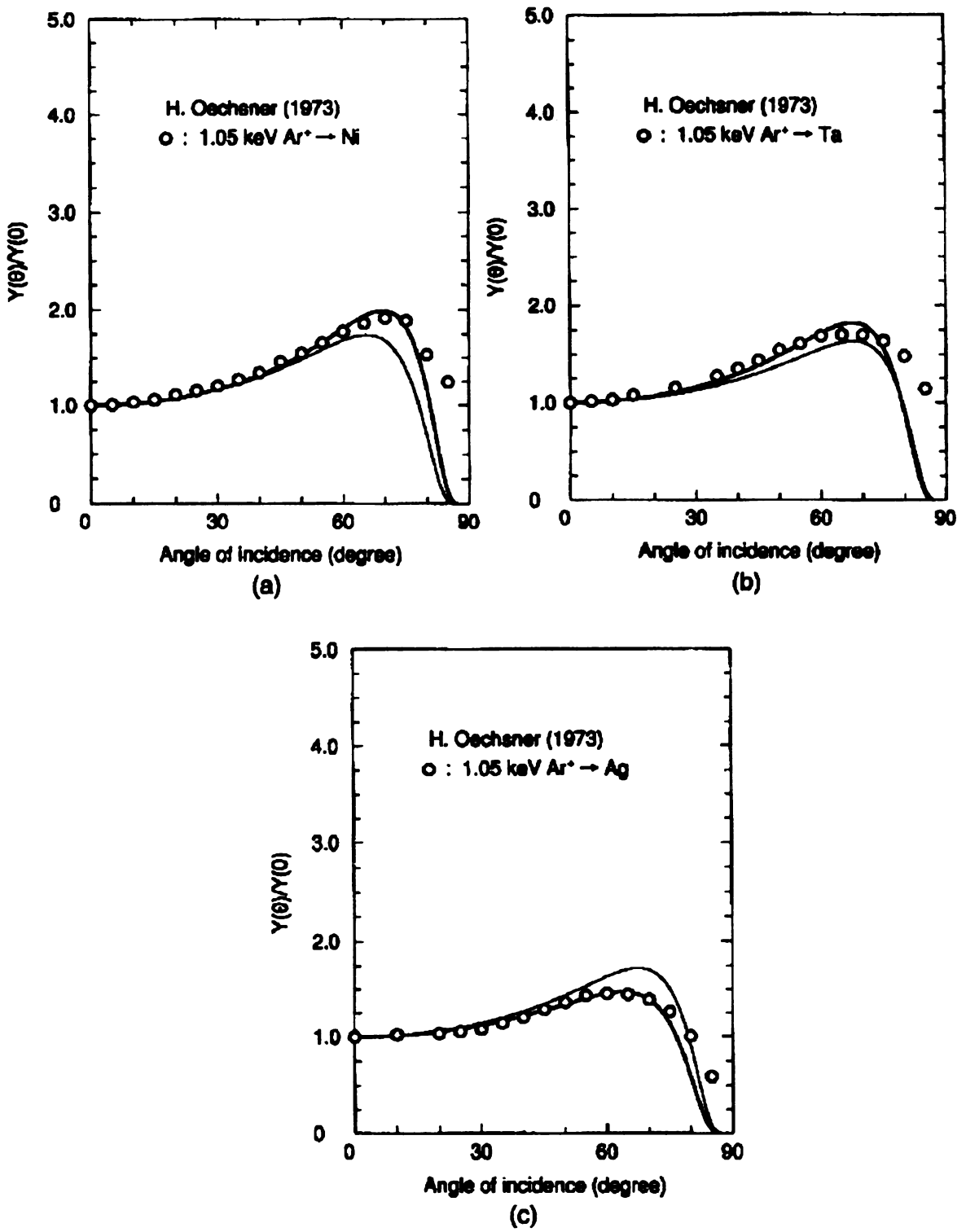

Figure 2-34 The Effect of Ion Incidence Angle on Sputter Yield (solid lines are Theoretical calculation by Yamamura et al. [1983] and circles are experimental data from Oechsner [1973]).

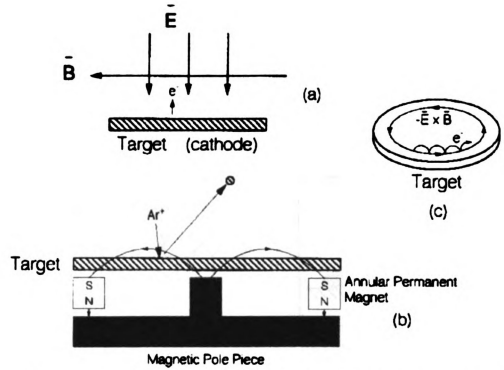

Figure 2-35 The Electron Trapping Effect of Applied Magnetic and Electrical Field [Mahan, 1999].

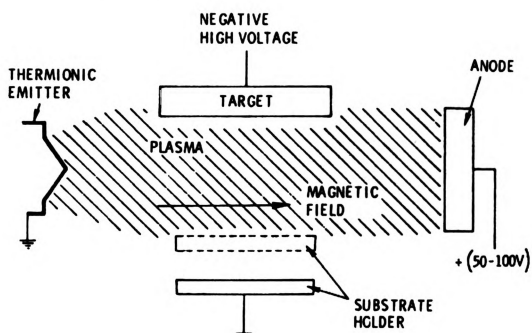

Figure 2-36 Schematic of a Triode Sputtering Source and Configuration [Bunshah, 1994].

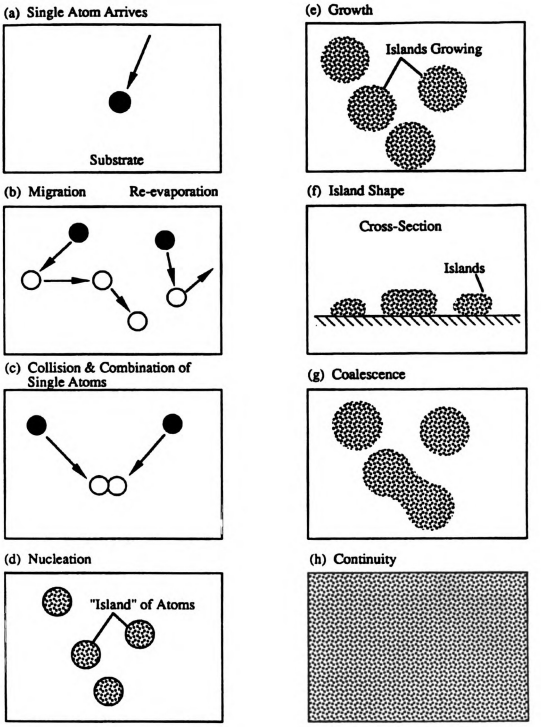

Figure 2-37 Schematic of Film Formation and Growth [Leawer, 1981].

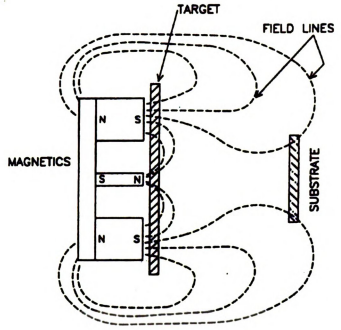

Figure 2-38 Schematic of an Unbalanced Magnetron [Rossnagel, 1982].

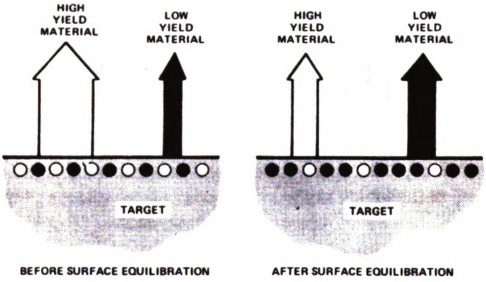

Figure 2-39 Schematic Diagram of Sputtering Yields from Initial and Altered Layer Target Surface Compositions [Bunshah, 1994].

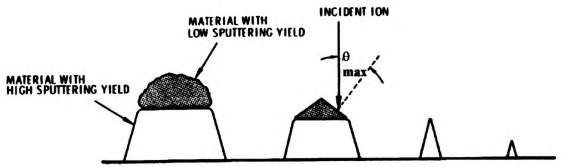

Figure 2-40 Schematic Drawing of the Formation of Cones [Bunshah, 1994].

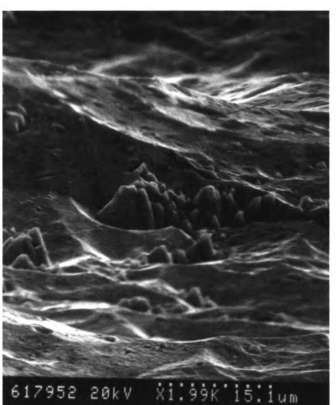

Figure 2-41 SEM Photomicrograph of Cone Structure on the Surface of a Sputtered Ni-Rich TiNi Target [Lee, 1994].

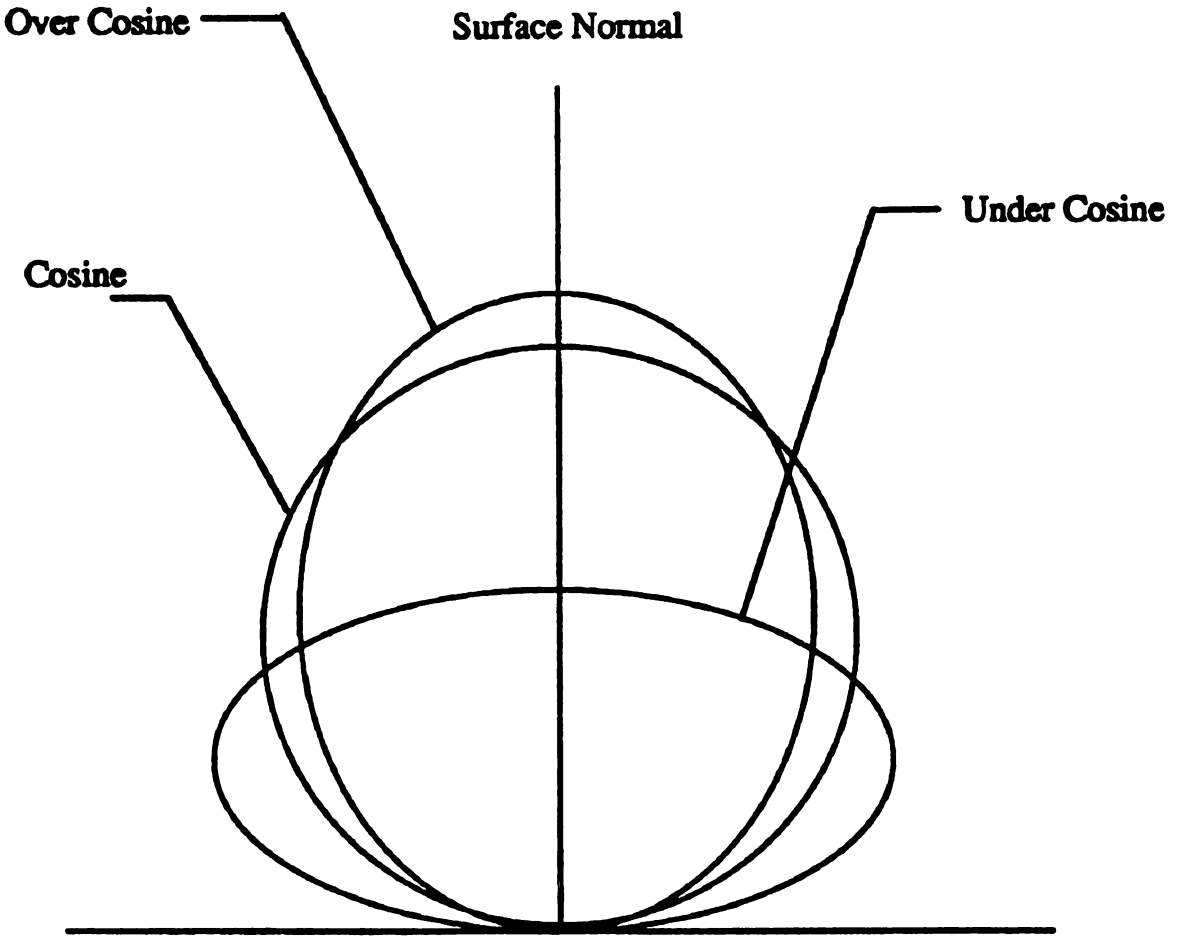

Figure 2-42 Angular Distribution of Sputter Atoms [Kay, 1962].

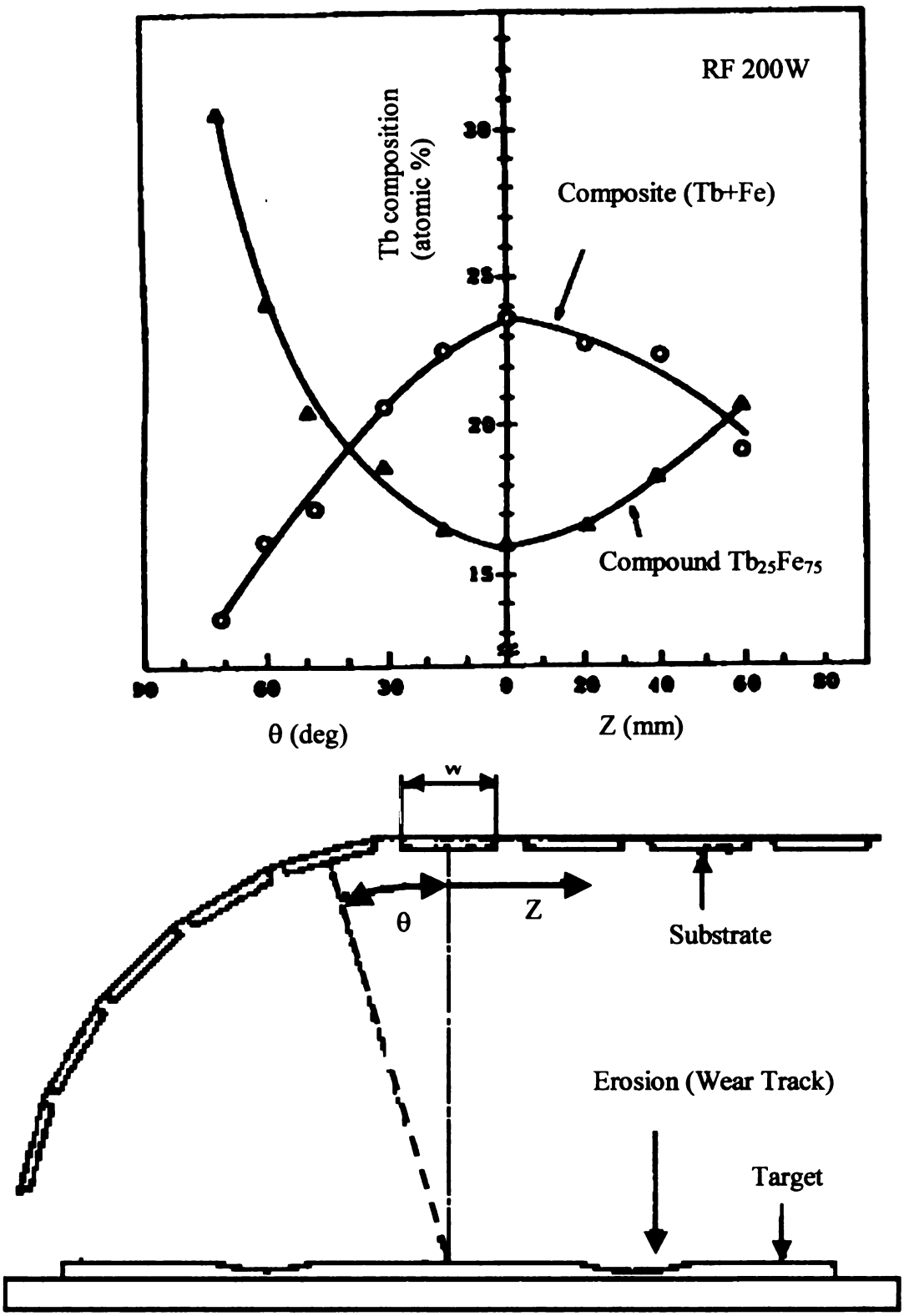

Figure 2-43 Lateral Composition Shifts Studies in TbFe alloy Sputtered Thin Films [Murakami, 1990].

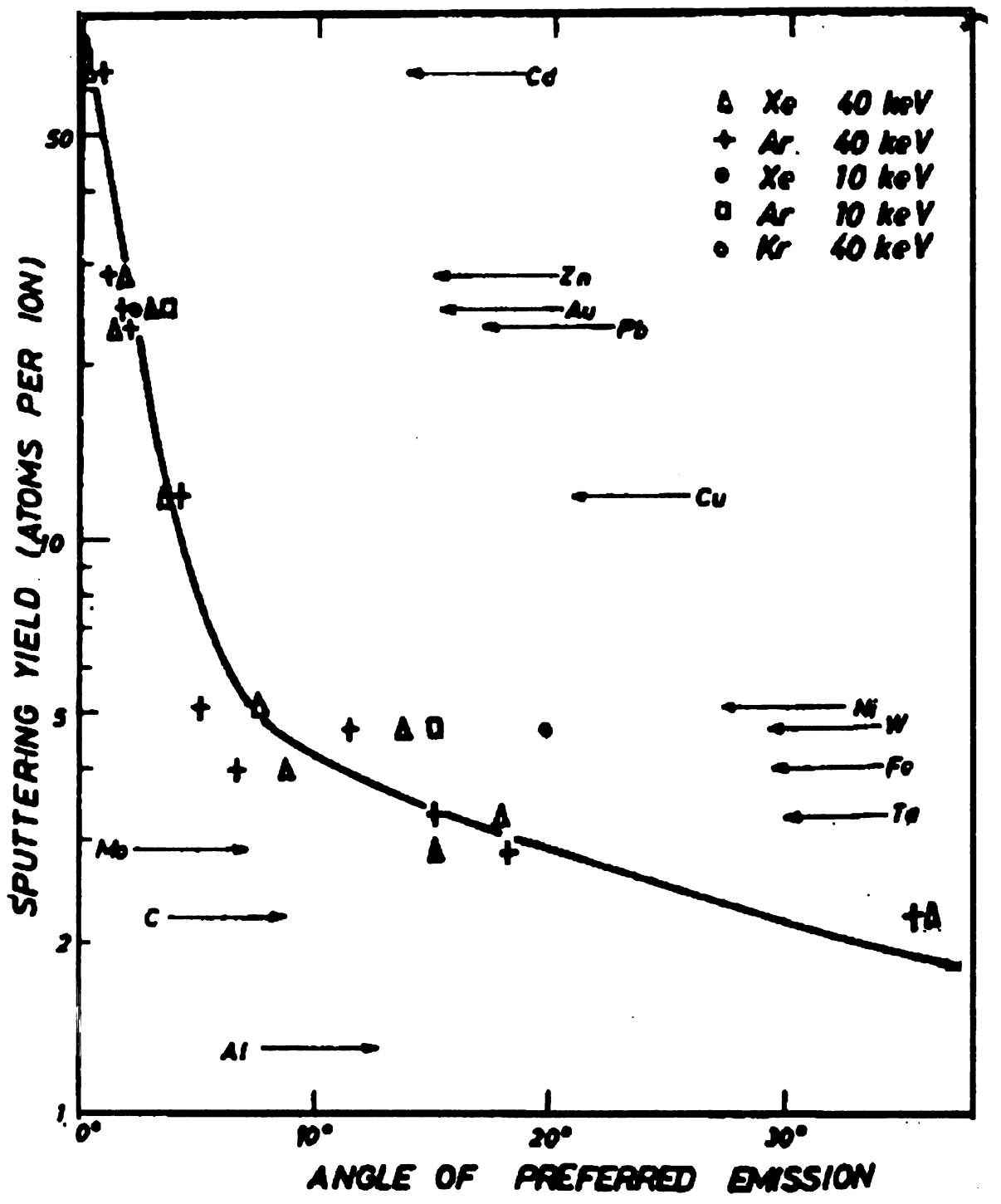

Figure 2-44 The Correlation of Emission Angle with Sputtering Yield [Betz, 1970].

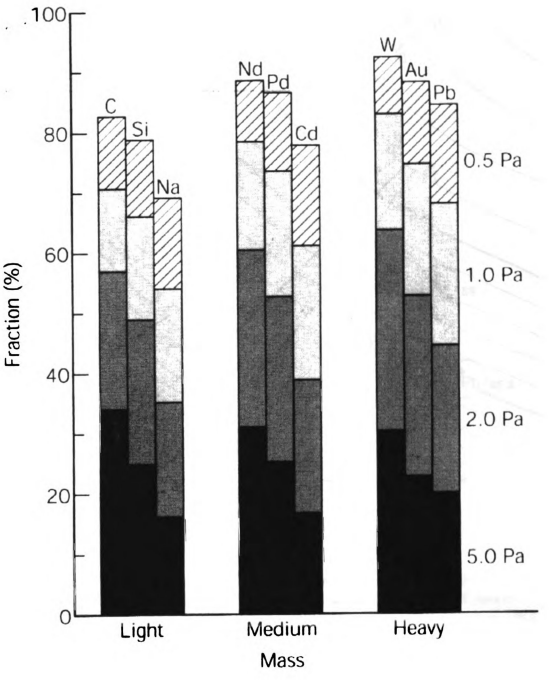

Figure 2-45 The Fraction of Sputter Particles That Reach the Substrate [Turner, 1992].

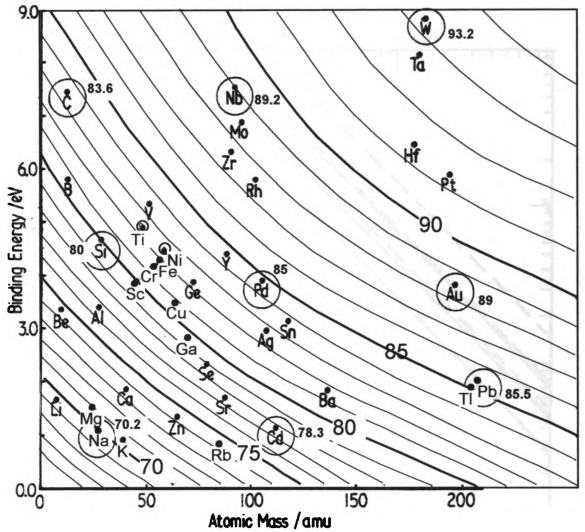

Figure 2-46 A Plot Showing the Binding Energy and Mass of Range of Elements Overlayed with Contour Lines that Indicate the Percentage of Atoms Reaching the Substrate, which was Interpolated from Turner et al. Data on Incident Flux Reduction at 3.5 mTorr. [Turner, 1992].

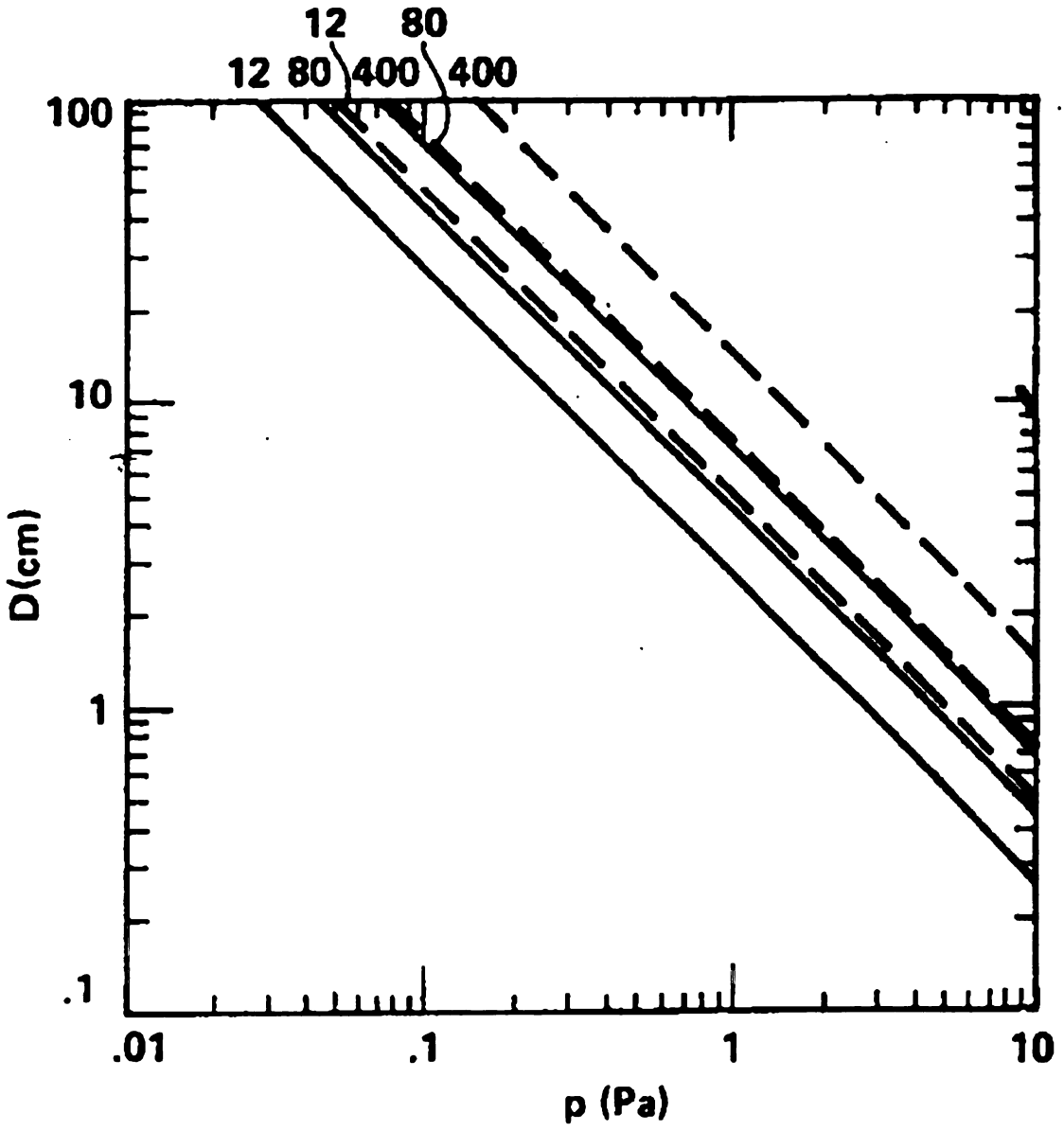

Figure 2-47 Thermalization Distance as Function of Pressure for Various Atomic Masses and Initial Energies [Westwood, 1978] (—— , 5 eV) (·····, 1000 eV).

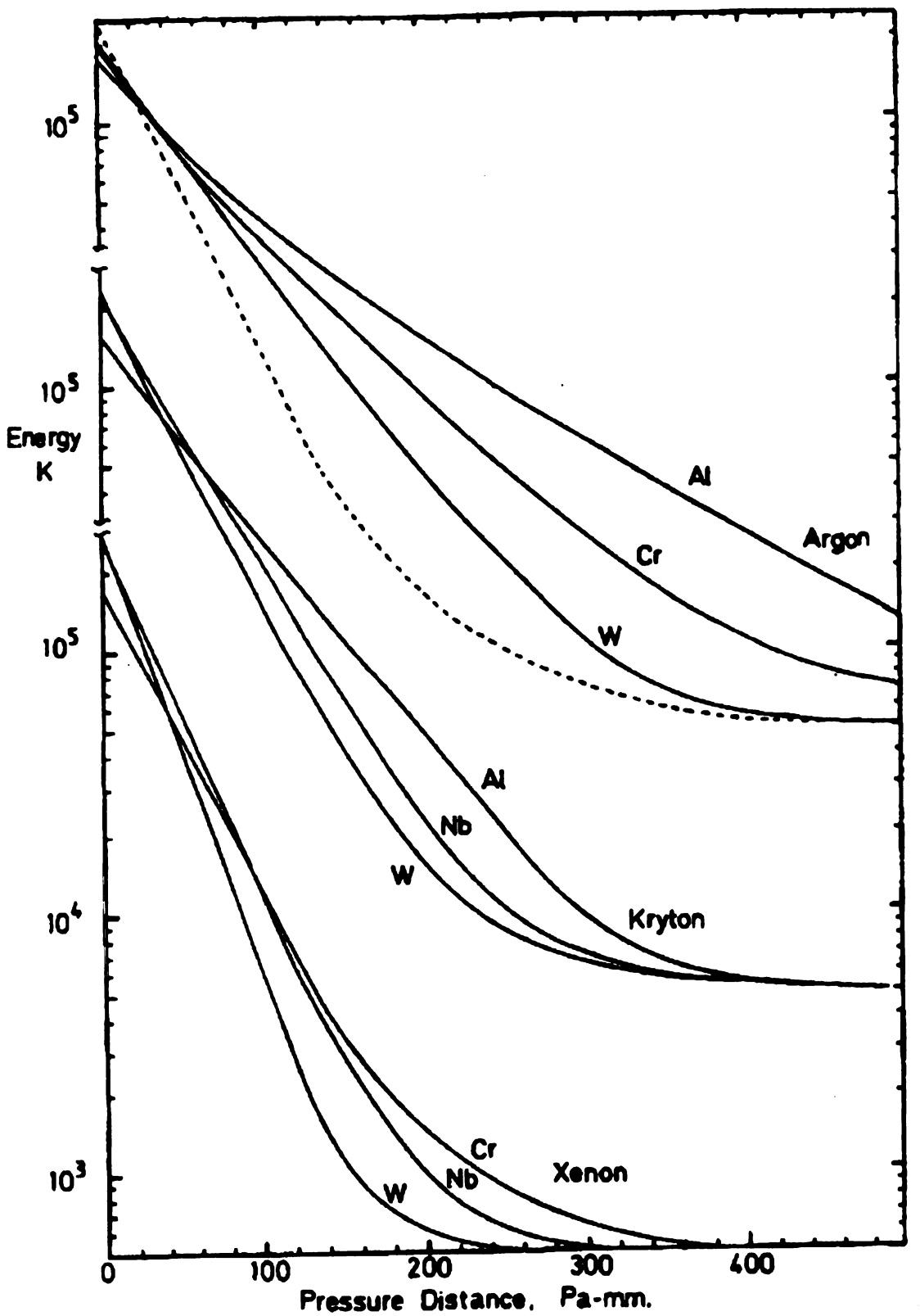

Figure 2-48 The Average Energies as Function of Working Gas-Distance Product [Somekh, 1984].

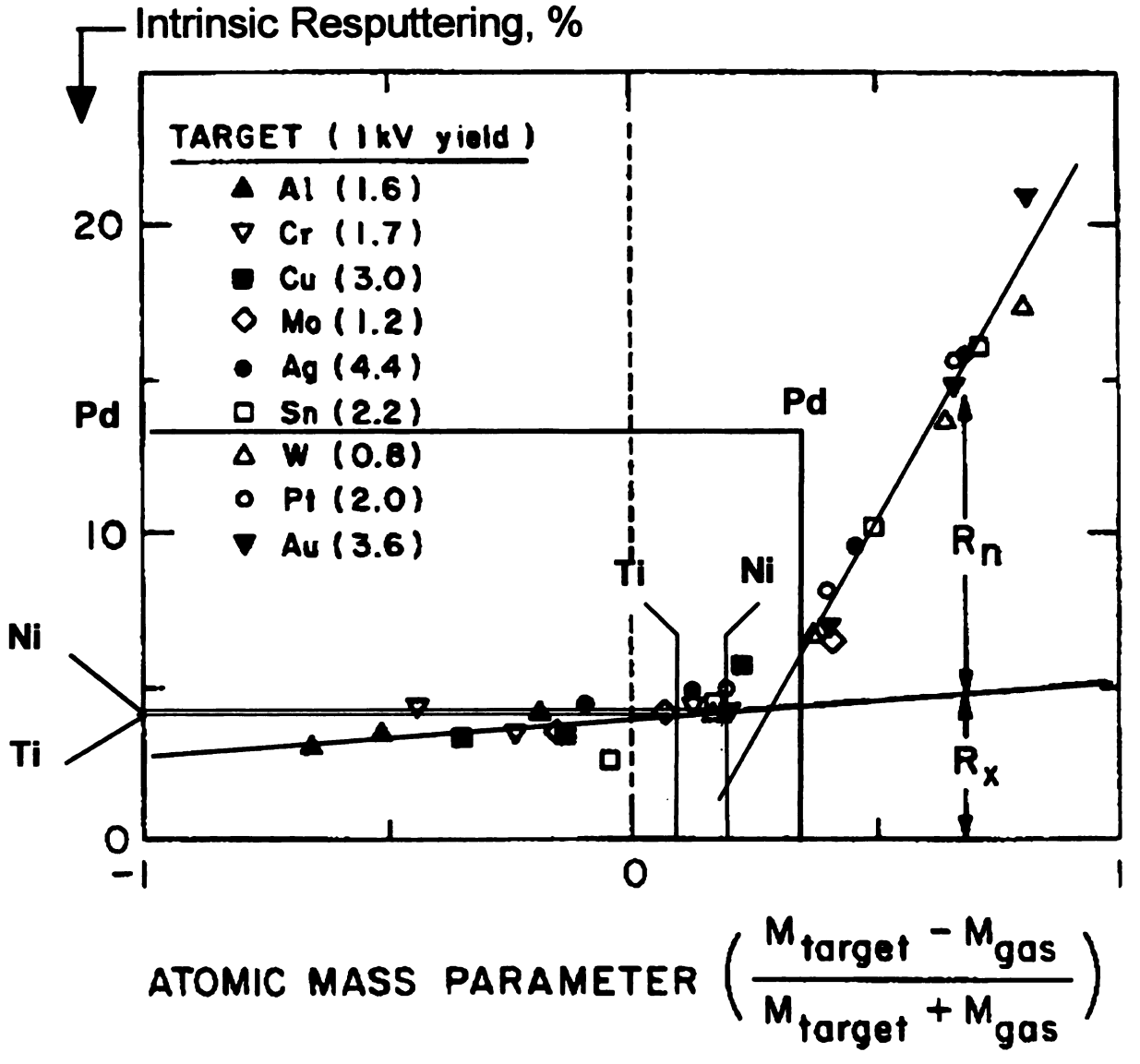

Figure 2-49 The Experiment Data of Intrinsic Resputtering as Function Atomic Mass Parameter and the Resputtering Fractions Calculated for Ti, Ni, and Pd [Hoffman, 1990].

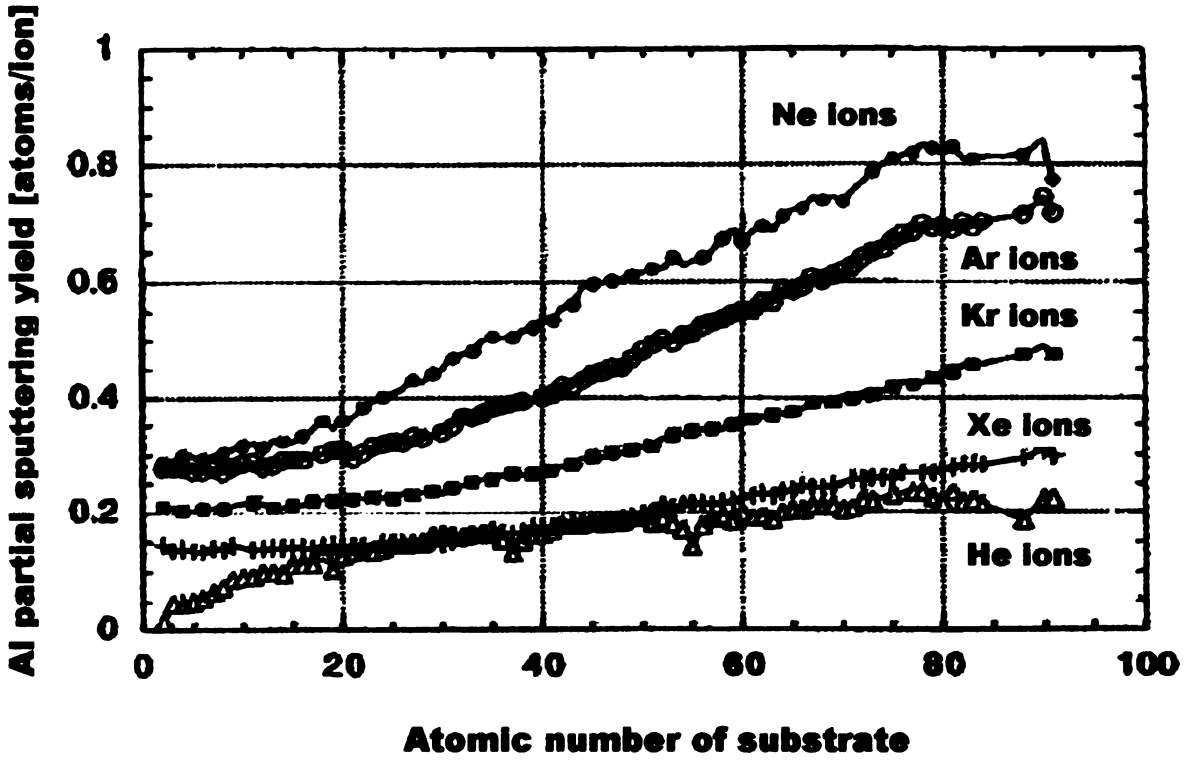

Figure 2-50 Static TRIM Simulations of Partial Sputtering Yield of a 1-nm Thick Al Layer as Function of Substrate Atomic Number for Various Incident Ion Types [Berg, 1999].

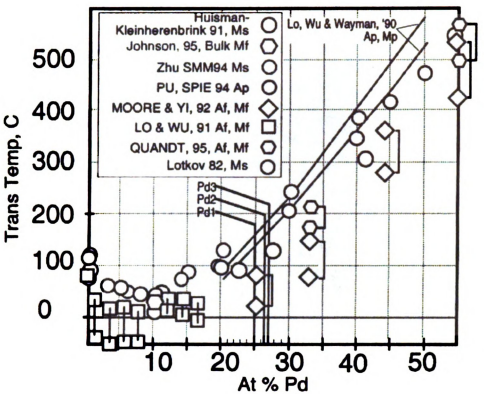

Figure 3-1 Literature Values for Transformation Temperatures of TiNiPd Alloys

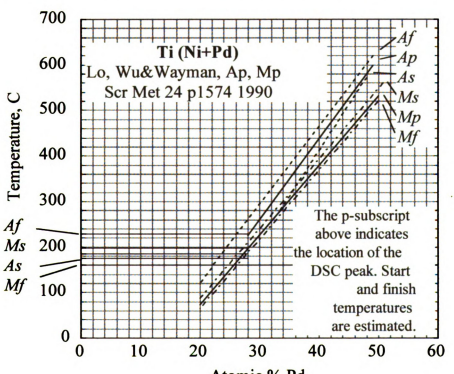

Figure 3-2 Lo-Wu-Wayman's 1990 TiNiPd Transformation Temperature Data

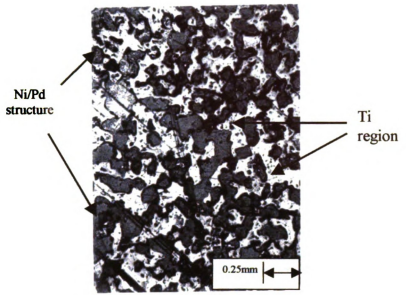

Figure 3-3 Optical photomicrograph of Ti 53.5/Pd 25/Ni 21.5 at. % Target taken at 50X

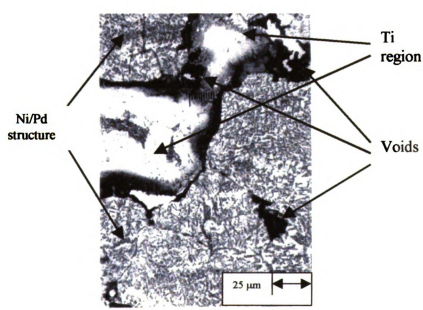

Figure 3-4 Optical photomicrograph of Ti 53.5/Pd 25/Ni 21.5 at. % Target taken at 500X

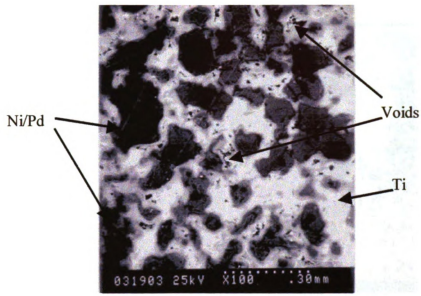

Figure 3-5 SEM photomicrograph at 100 X of the Ti 53.5/Pd 25/Ni 21.5 at. % Target

Figure 3-6 SEM photomicrograph at 1200 X of the Ti 53.5/Pd 25/Ni 21.5 at. % Target

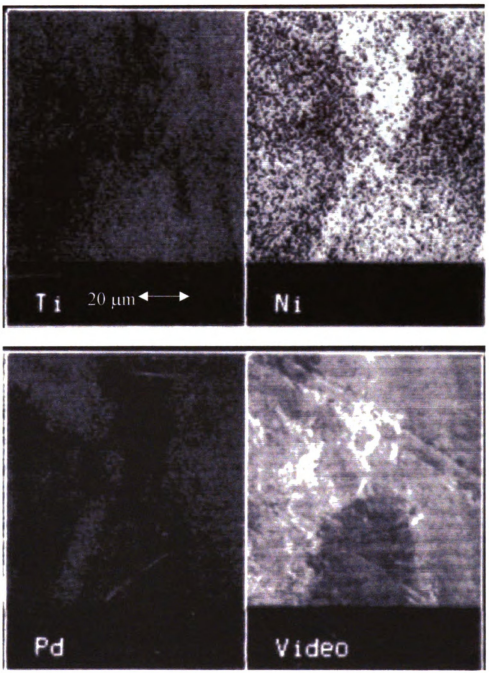

Figure 3-7 X-ray Map for Ti, Ni, and Pd of Target Pd1 at 1000X

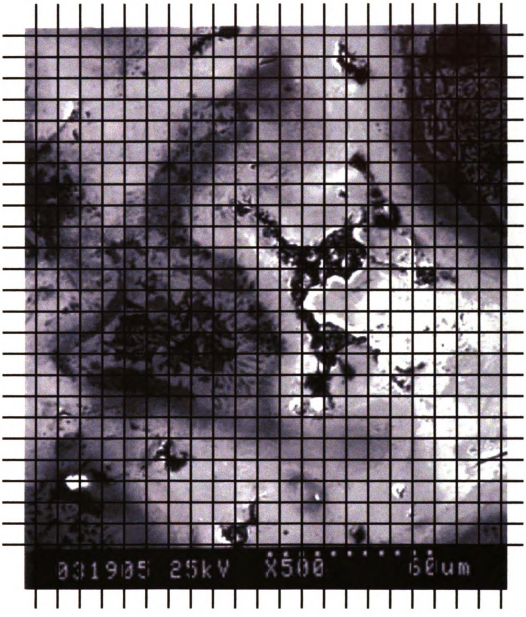

Figure 3-8 SEM Photomicrograph taken at 500X Overlayed with 550 Point Grid used for Void Volume Fraction Calculation.

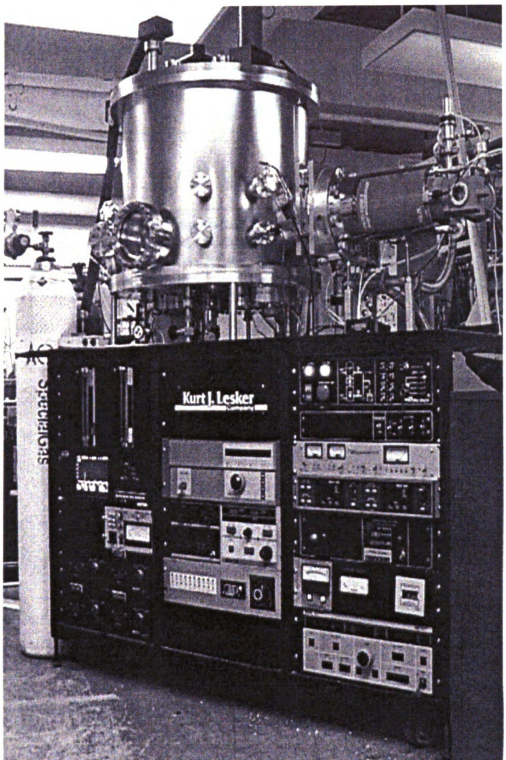

Figure 3-9 Kurt J. Lesker Sputter Deposition System

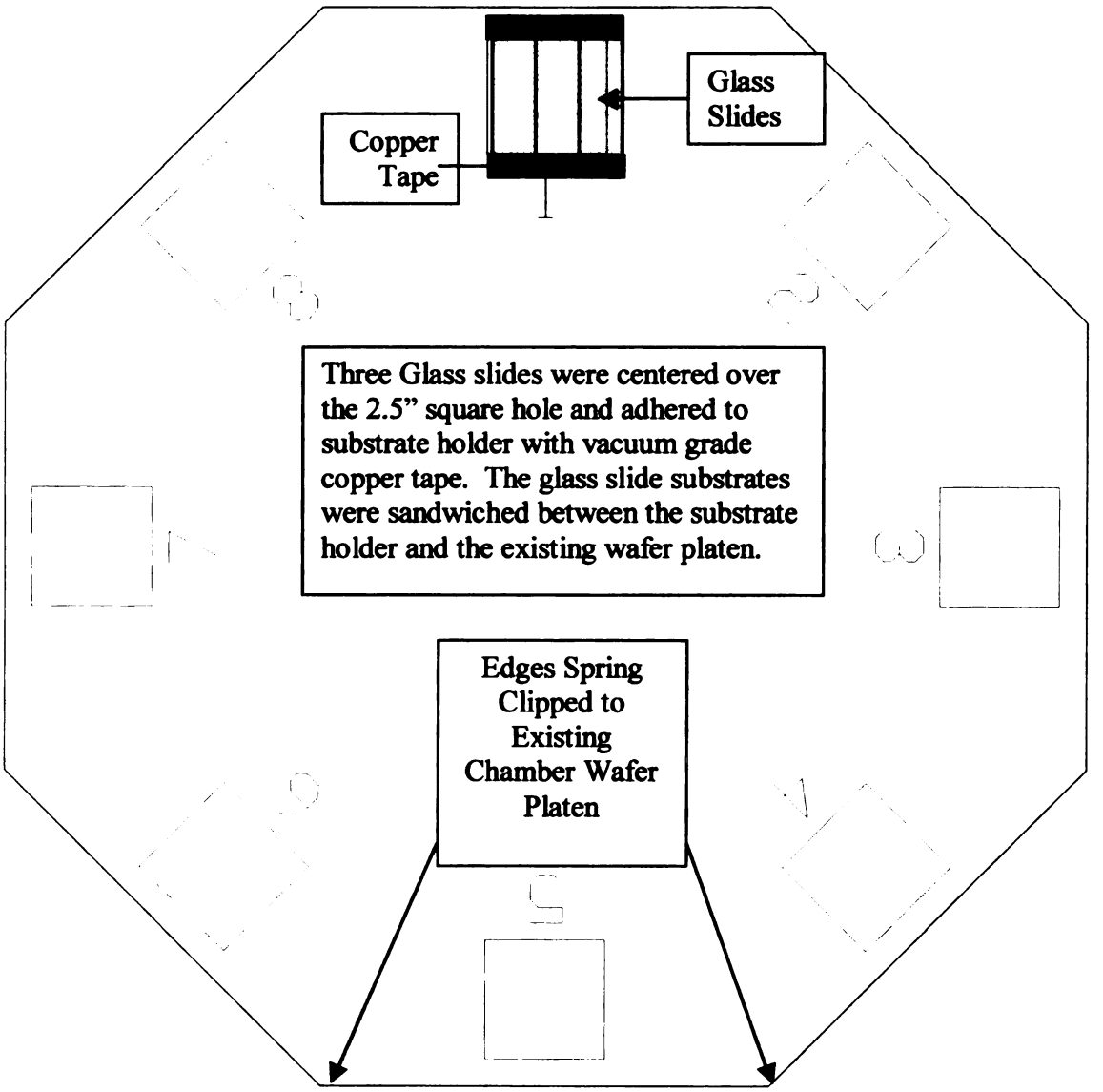

Figure 3-10 Aluminum Substrate Holder

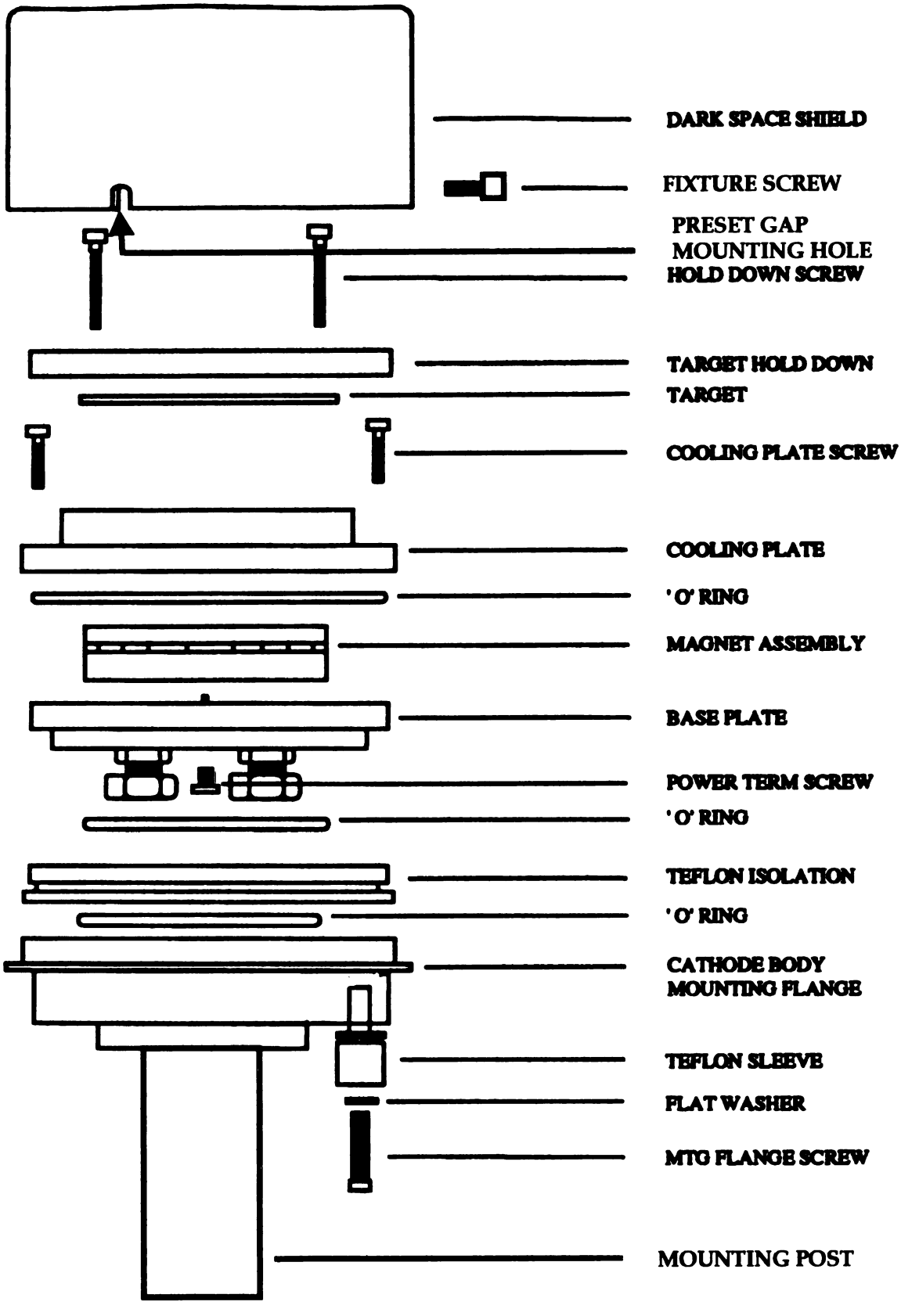

Figure 3-11 Torus 3M Magnetron Sputtering Gun Assembly

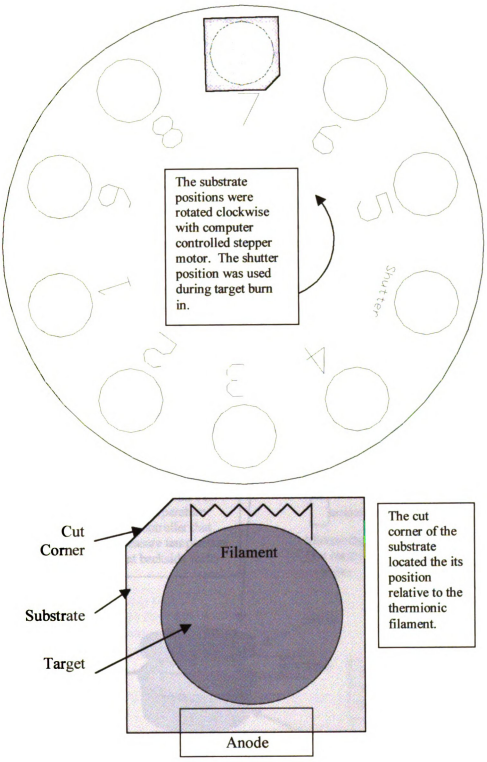

Figure 3-12 Triode Substrate and Gun Position Setup.

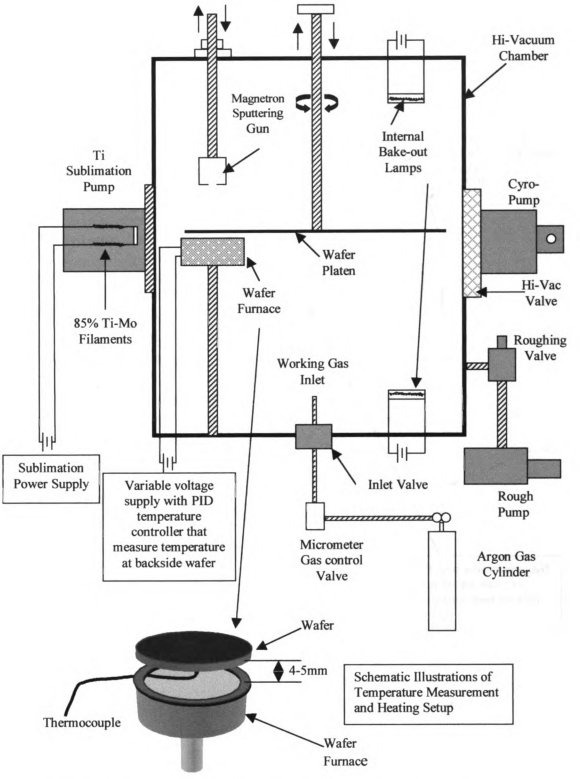

Figure 3-13 Basic Schematic of the Thin Film Deposition Unit Used in Magnetron Sputtered TiNi and TiNiPd Thin Film Composition Experiments

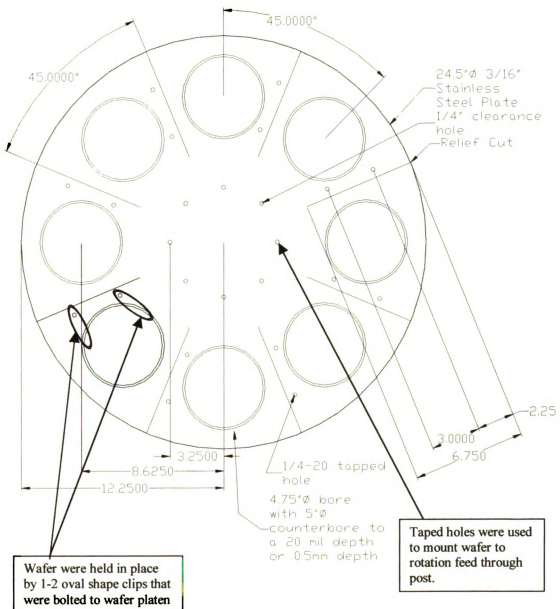

Figure 3-14 5-inch Wafer Platen Used for Depositing TiNiPd Thin Films

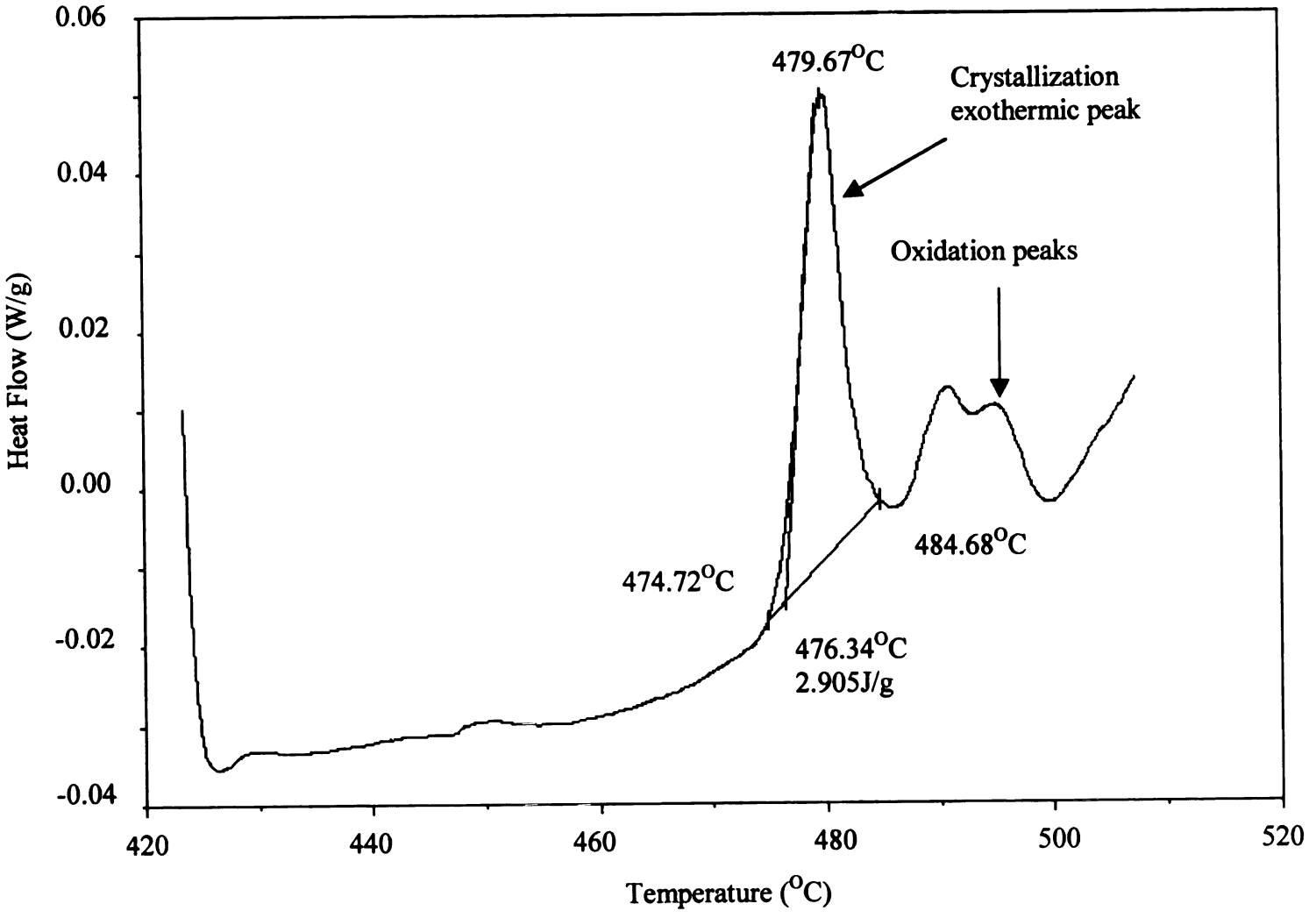

Figure 3-15 DSC Curve Used to Calculate the Crystallization Temperature for Specimen # 02240001 (weight was 5.5 mg and scanned at 5°C/min)

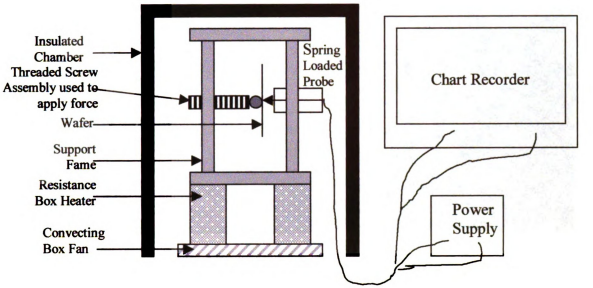

Figure 3-16 Resistivity Device Schematic

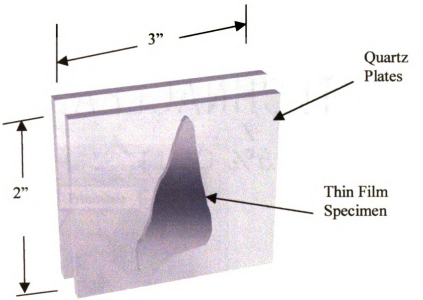

Figure 3-17 Schematic of Annealing Sample Setup

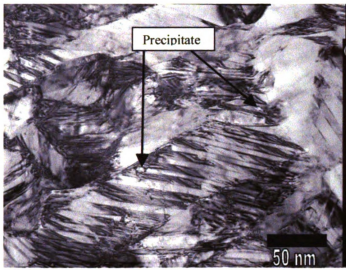

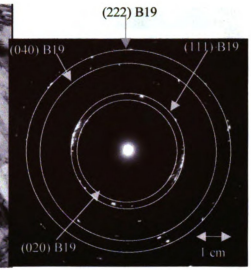

Figure 3-18 (a)TEM Microphotograph of Specimen #03020001-AN0518-500 (100 kX) (b)TEM Diffraction Pattern of B19 Martensite (Camera Length 1.2m)

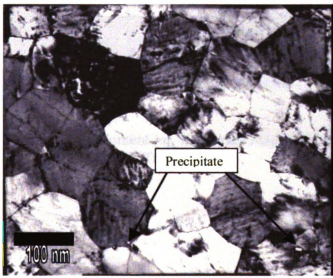

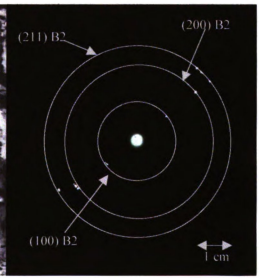

Figure 3-19 (a)TEM Microphotograph of Specimen #03020001-AN0518-500 at 300°C(50 kX) (b)TEM Diffraction Pattern of B2 Austenite (Camera Length 1.2m)

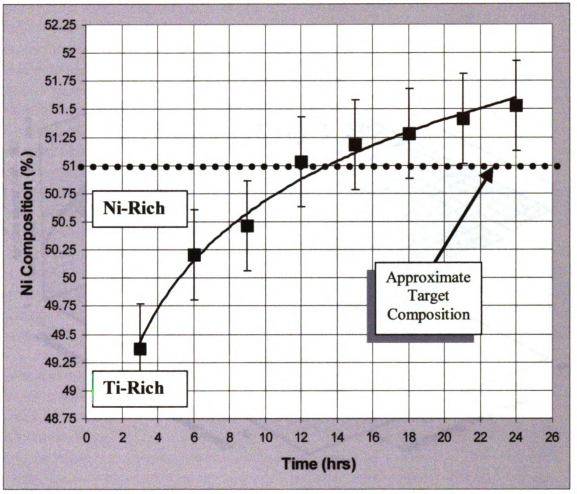

Figure 4-1 Ni Content (at. %) Verses Magnetron Diode Sputtering Time from 51 at% Ni/ 48 at% Ti Target.

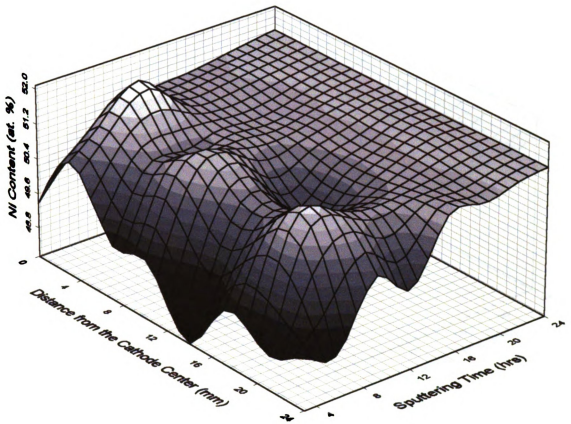

Figure 4-2 Surface Plot of Ni Composition as Function Sputtering Time and Distance from Center of Diode Cathode from 51 at% Ni/ 48 at% Ti Target.

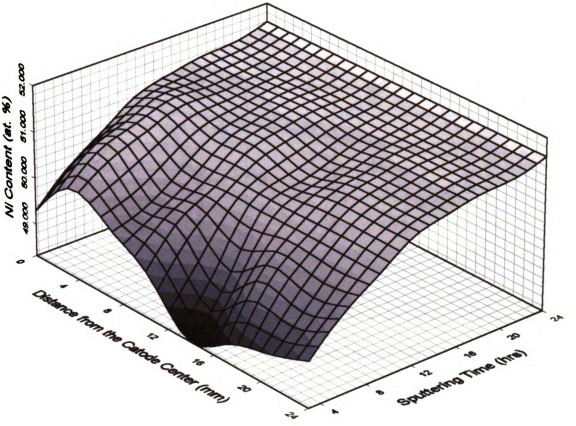

Figure 4-3 Rough Schematic of Smoothed surface plot of Ni Composition as Function Sputtering Time and Distance from Center of Diode Cathode from 51 at% Ni/48 at% Ti Target.

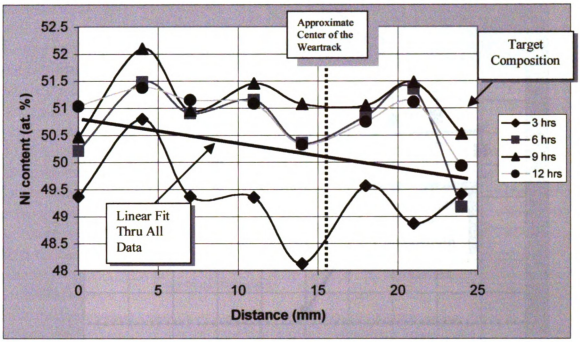

Figure 4-4 Ni Content Verses Radial Distance from Diode Cathode Center for first 12 Hours of Sputtering.

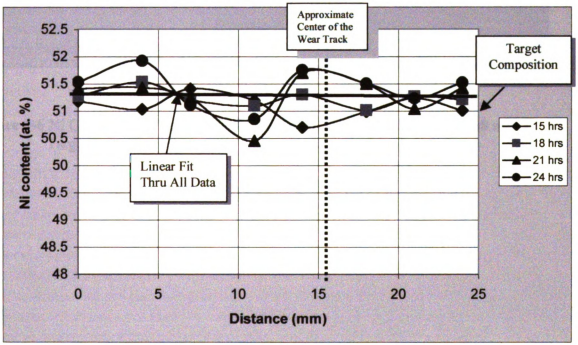

Figure 4-5 Ni Content Verses Radial Distance from Diode Cathode Center for 15 to 24 Hours of Sputtering.

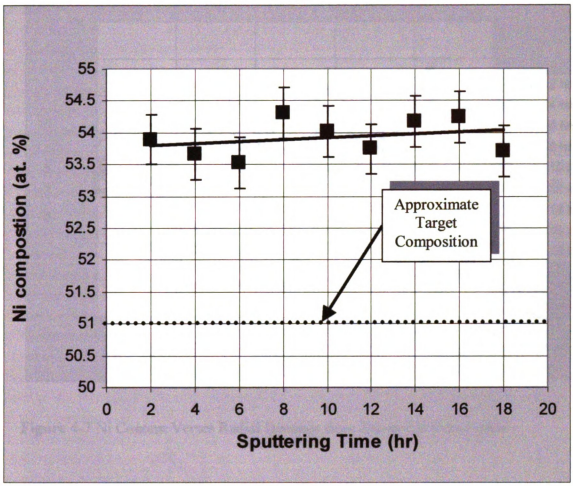

Figure 4-6 Ni Composition Verses Triode Sputtering Time from 51 at.% Ni/ 48 at% Ti Target.

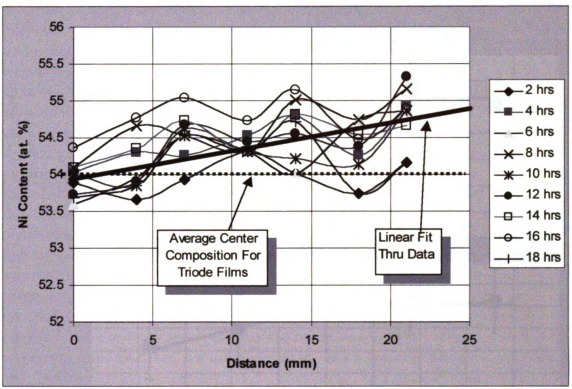

Figure 4-7 Ni Content Verses Radial Distance from Triode Cathode Center.

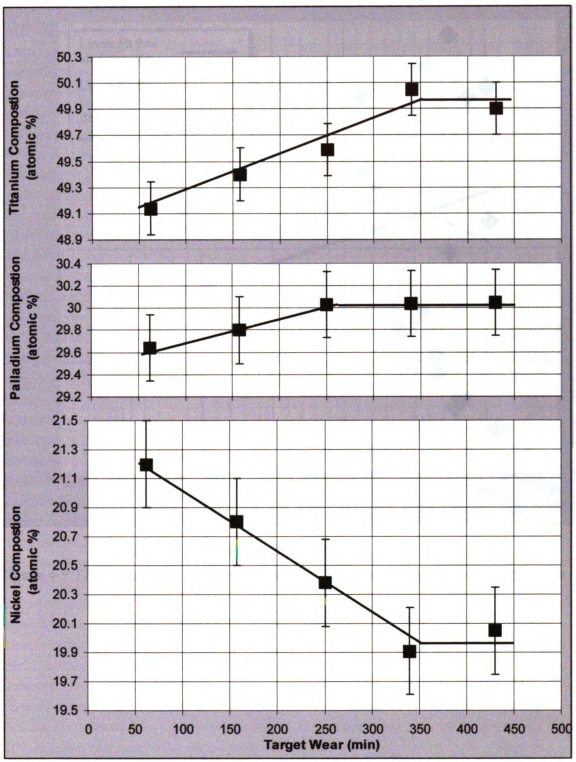

Figure 4-8 Composition Verse Elapsed Target Wear Time of Ti 53.5%/ Ni 21.5 %/ Pd 25% Target.

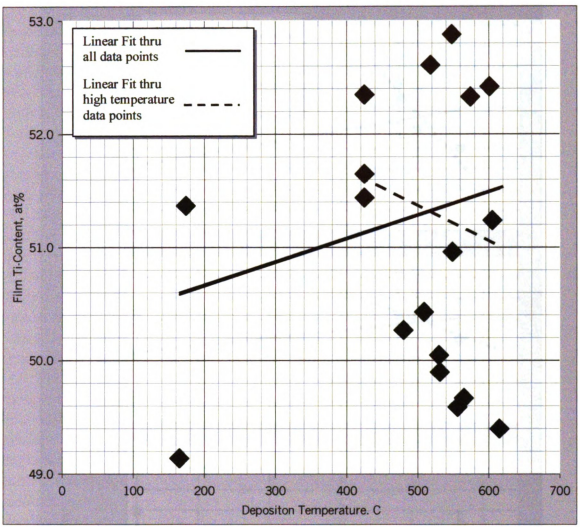

Figure 4-9 Ti Content of the Ti(Ni+Pd) Films as a Function of Deposition Temperature.

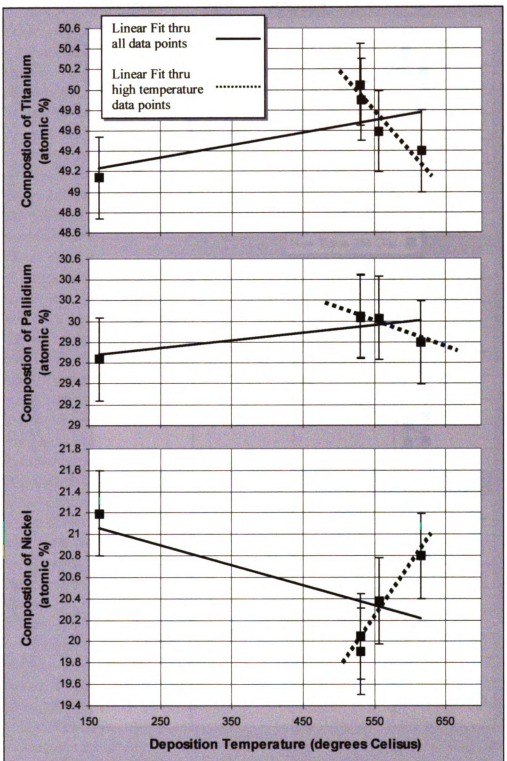

Figure 4-10 Film Composition vs.Deposition Temperature for the Ti 53.5%/ Ni 21.5 %/ Pd 25% Target.

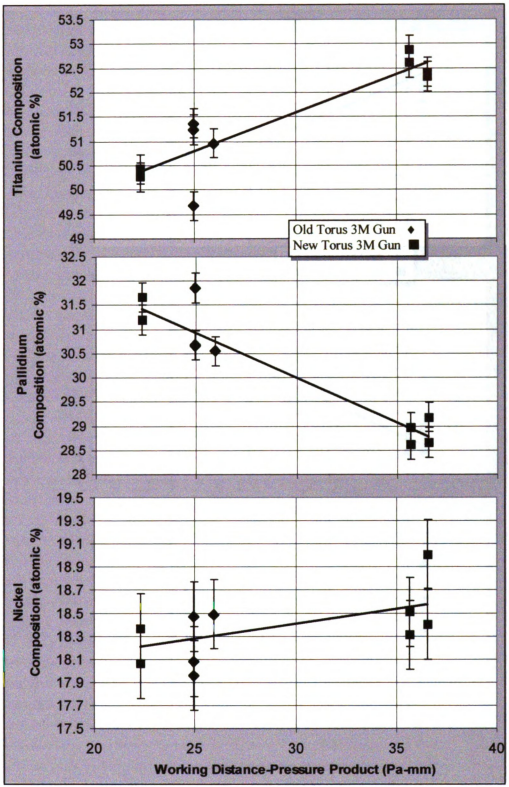

Figure 4-11 Film Composition vs. Pressure-Distance Product for Thin Films Sputtered from the Ti 53.5%/ Ni 19.5%/ Pd 27% Target.

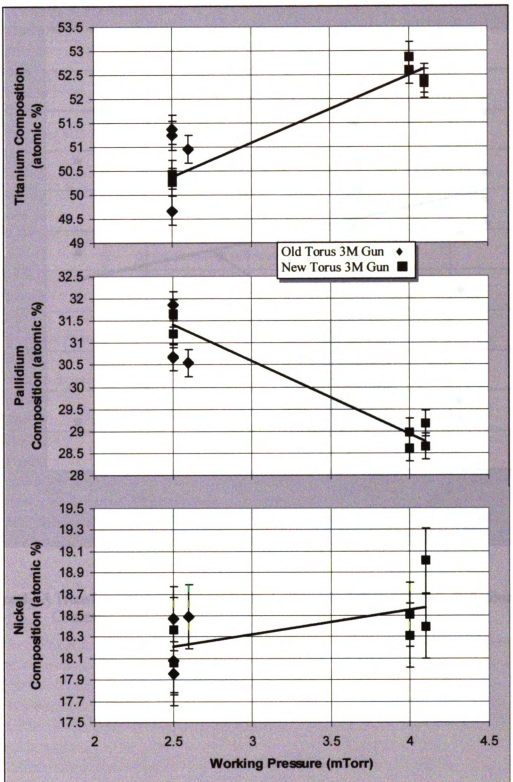

Figure 4-12 Composition vs. Working Gas Pressure for Thin Films Sputtered from the Ti 53.5%/ Ni 19.5%/ Pd 27% Target.

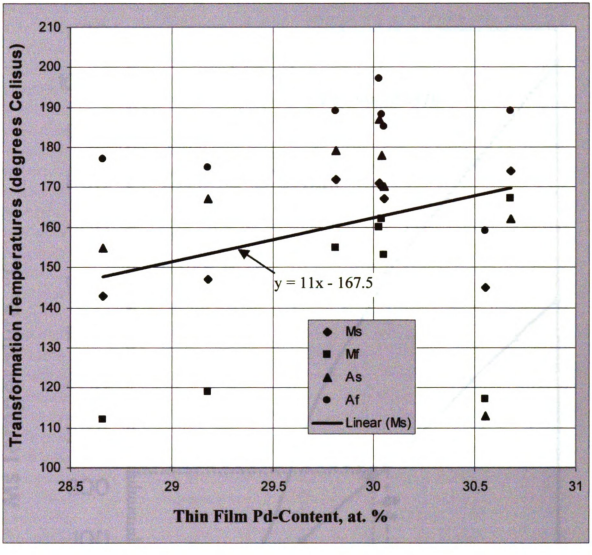

Figure 4-13 Transformation Temperatures in As-deposited Thin Films vs. Palladium Content.

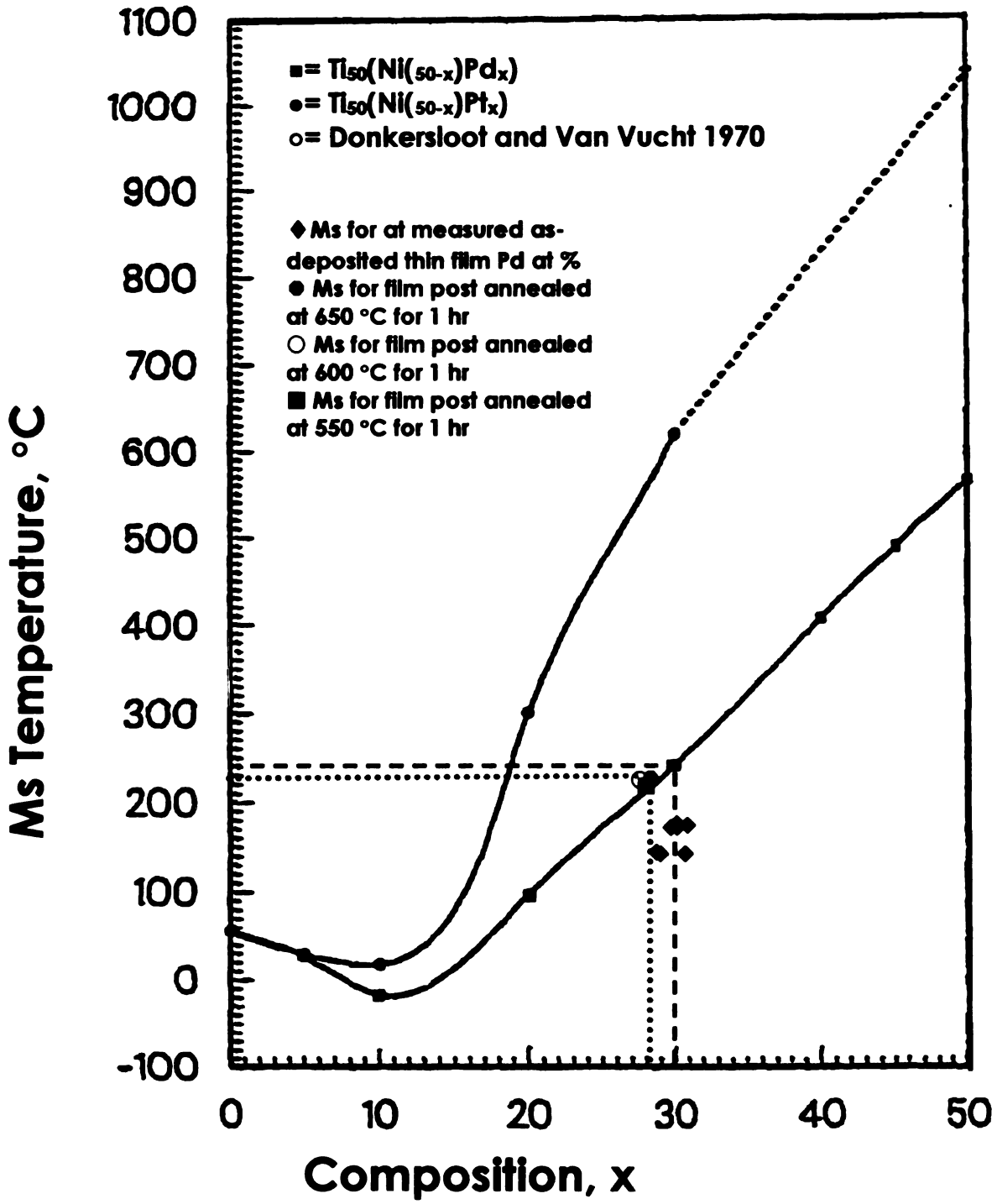

Figure 4-14 M_s Temperature as Function of Palladium Contents: Published Values Compared to As-deposited and Annealed Thin Films[Lindquist, 1988].

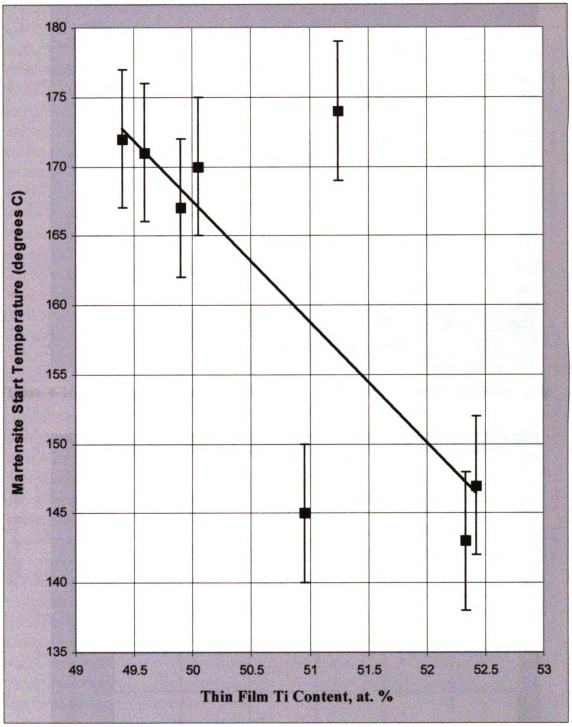

Figure 4-15 M_s Temperature as a Function of Titanium Content for As-Deposited Thin Films.

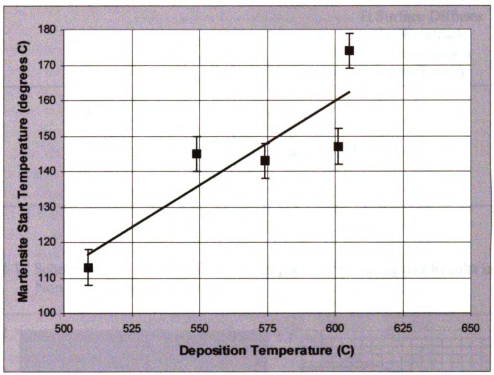

Figure 4-16(a) M_s Temperature Verse Deposition Temperature for As-deposited Thin Films from 53.5% Ti/ 19.5% Ni/ 27% Pd Target.

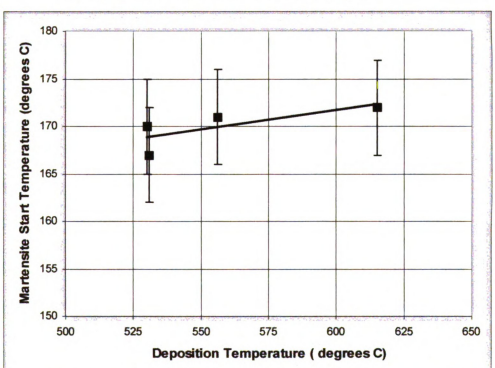

Figure 4-16(b M_s Temperature Verse Deposition Temperature for As-deposited Thin Films from 53.5% Ti/ 21.5% Ni/ 25% Pd Target.

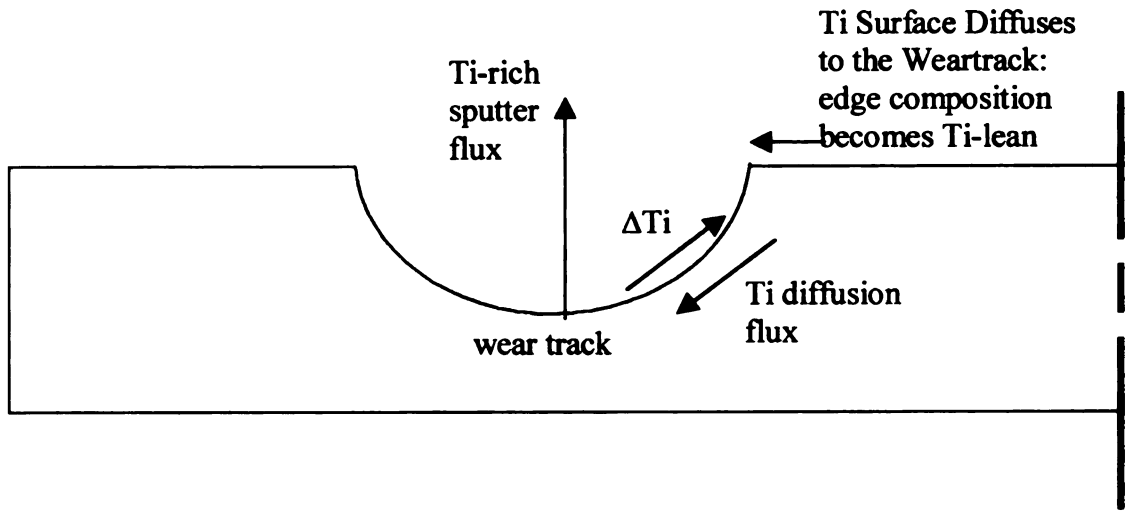

Figure 4-17 Schematic of Surface Diffusion in Magnetron Sputtering that Results in a Non-Steady State Sputter Flux.

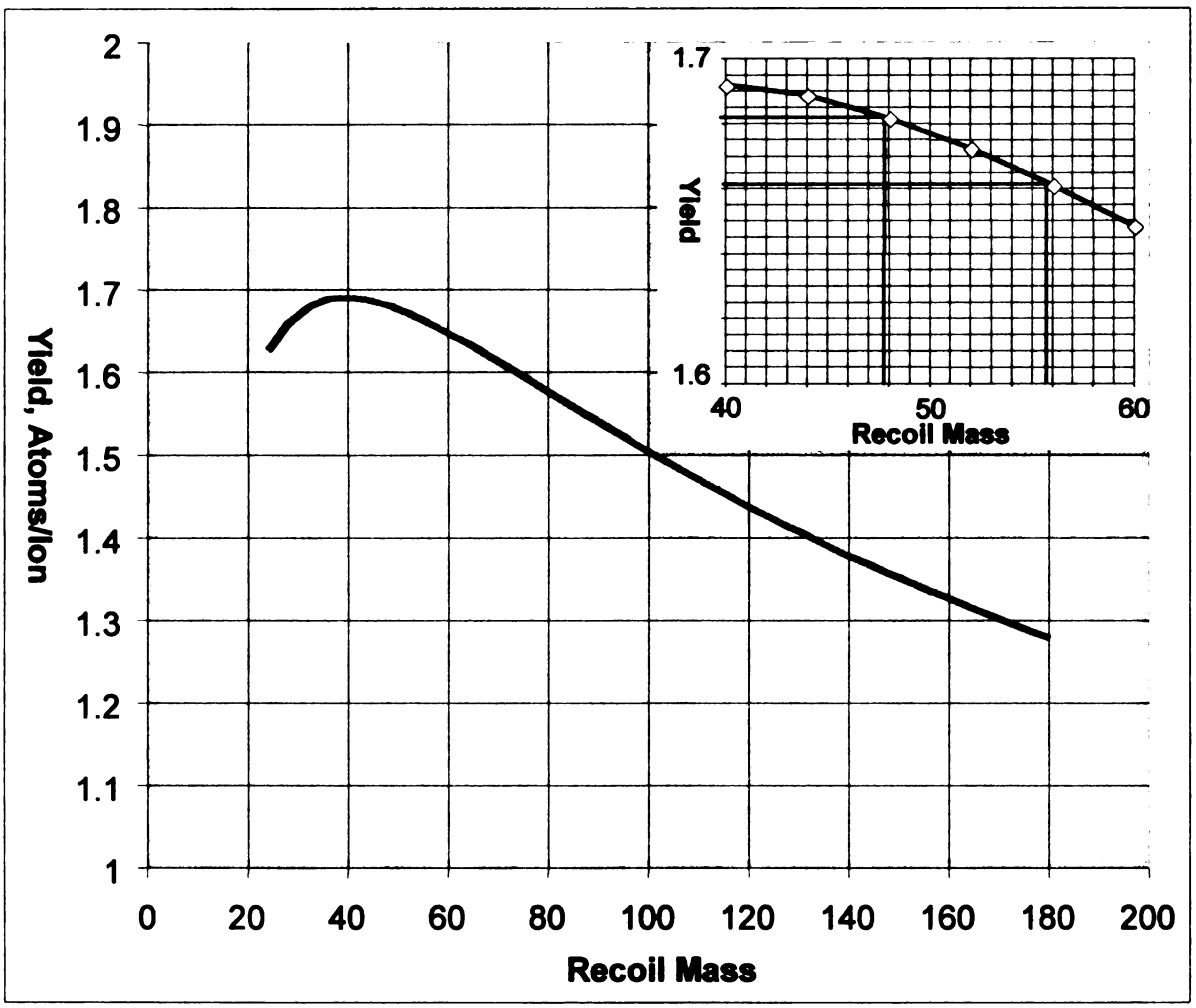

Figure 4-18 The Effects of Recoil Mass on Preferential Sputtering of Alloy Calculated from Matsunami *et al.* Sputter Yield Formula using Argon Projectiles.

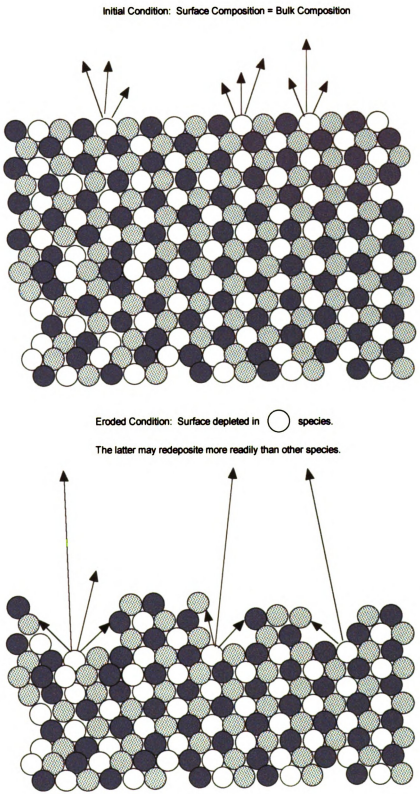

Figure 4-19 Schematic of the Possible Surface Topography Developed in P/M Targets at Steady State.